Structure and Dynamics Away from Equilibrium: Scaling results from a few condensed matter systems

A Thesis

Submitted for the Degree of

DOCTOR OF PHILOSOPHY

in the Faculty of Science

by

Nalina Vadakkayil

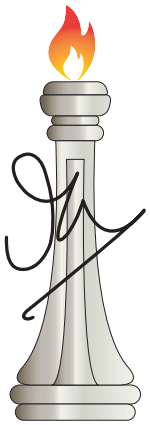

JNCASR

THEORETICAL SCIENCES UNIT
JAWAHARLAL NEHRU CENTRE FOR ADVANCED SCIENTIFIC RESEARCH
(A Deemed University)
Bangalore – 560 064

December 2021

To my parents and teachers

DECLARATION

I hereby declare that the matter embodied in the thesis entitled "**Structure and Dynamics Away from Equilibrium: Scaling results from a few condensed matter systems**" is the result of investigations carried out by me at the Theoretical Sciences Unit, Jawaharlal Nehru Centre for Advanced Scientific Research, Bangalore, India under the supervision of **Prof. Subir K. Das**, and that it has not been submitted elsewhere for the award of any degree or diploma.

In keeping with the general practice in reporting scientific observations, due acknowledgment has been made whenever the work described is based on the findings of other investigators.

Nalina

Nalina Vadakkayil

CERTIFICATE

I hereby certify that the matter embodied in this thesis entitled "**Structure and Dynamics Away from Equilibrium: Scaling results from a few condensed matter systems**" has been carried out by **Nalina Vadakkayil** at the Theoretical Sciences Unit, Jawaharlal Nehru Centre for Advanced Scientific Research, Bangalore, India under my supervision and that it has not been submitted elsewhere for the award of any degree or diploma.

Subir Kumar Das

Prof. Subir K. Das
(Research Supervisor)

Acknowledgements

First and foremost, I would like to extend my sincere gratitude to my Ph.D. supervisor Prof. Subir K. Das for allowing me to be a part of his research group, soft matter and statistical mechanics (SMSM), in the theoretical sciences unit (TSU), JNCASR. He introduced me to various interesting problems, and I enjoyed working on each of those. I am highly thankful to him for his constant help, guidance, encouragement, and patience. His insightful feedback and suggestions always helped me to move forward.

I would like to express my gratitude to all the course instructors, Prof. N.S. Vidhyadhiraja, Prof. Subir K. Das, Prof. Meheboob Alam, Prof. Swapan K. Pati, Prof. Shobhana Narasimhan, Dr. Meher K. Prakash, Prof. Rajesh Ganapathy, Prof. Srikanth Sastry, and Prof. Kavita Jain for the wonderful courses they offered.

I thank all the TSU faculty members for being the source of inspiration.

I would also like to acknowledge the Graduate Student Advisory Committee (GSAC) members, Prof. Rajesh Ganapathy and Dr. Meher K. Prakash for their timely evaluations of the progress of the thesis.

My sincere thanks to my seniors from SMSM, Dr. Jiarul Midya, Dr. Saikat Chakraborty, and Dr. Subhajit Paul. The discussions with them were always like learning sessions for me. I am also thankful to all other past and short-term members of the group: Dr. Sunita, Dr. Sanat K. Singha, Arya, and Mousumi for the cheerful times that we had. Special thanks to all the current members of the group, Koyel, Arabinda, Soumik, Sohini, Tanay, Purnendu, and Anjaney for all the discussions and help that they rendered.

I would like to thank Dr. Sutapa Roy, with whom I have been collaborating on one of the projects, for all the valuable discussions.

I acknowledge JNCASR for financial support.

I would also like to thank the PARAM Yukti facility under the National Supercomputing Mission (NSM) at JNCASR for providing the computational facilities for carrying out some of the works.

I am grateful to all the staff members from Library, CompLab, Academic section, Administration, Accounts, Dhanvantari, Hostel office, Housekeeping department, Mess, and Dining hall for their kind services.

Special thanks to all my friends outside the lab, Sharona, Neha, Sukanya, Archana, Nabadyutidi, and Sayanidi for always being helpful.

Thanks to the music group at JNCASR led by Dr. Nirmala Balwali for the memorable sessions.

I would also like to acknowledge my teachers Prof. Dwaraka Rani Rao, Dr. Deepa Seetharaman, Prof. C. Raghu, and Dr. Promod Dominic for their encouragement during my college days.

I owe my deepest gratitude to my parents for the freedom that they gave me to pursue what interested me the most. Thanks to my sister, Nayana, for always being supportive.

Synopsis

This thesis contains reports from the studies of certain nonequilibrium properties of some systems undergoing different kinds of phase transitions, viz., para-to-ferromagnetic transition and vapor-solid transition. It also contains a scaling picture of disease spread, in line with that in the literature of phase transitions.

In **chapter 1** an introduction to phase transitions and discussions of related scaling properties are provided. All the techniques that are used for the undertaken studies in different chapters are also discussed in detail in this chapter, alongside introductions to the considered models.

In **chapter 2** we study ordering dynamics during the evolution of a ferromagnetic system, when quenched to zero temperature ($T_f = 0$), in space dimensions $d = 2$ and 3, from high temperature disordered phase. We perform this study via Monte Carlo simulations of the Glauber Ising model, using two different algorithms, viz., Metropolis and Glauber. We show that the structures formed during the evolution in $d = 3$ are different from a well-known theoretical expectation that describes results obtained following quenches to temperatures reasonably close to the critical value. We also extract the power-law exponent for domain growth. Unlike for the higher temperature quenches, it is shown that the theoretical value of the growth exponent agrees with the simulation results only in the long time limit. Furthermore, we present results for the aging phenomena at $T_f = 0$. We have used the two-time autocorrelation function, $C_{\rm ag}(t, t_w)$, for probing this phenomena. This quantity decays in a power-law fashion. We have used a recently devised finite-size scaling technique to estimate λ, the corresponding exponent. Interestingly, the obtained value of λ violates a well-known bound. This we understand via the analysis of structure.

Chapter 3 deals with the investigation of the temperature dependence of aging exponent (λ) for quenches below the roughening transition temperature (T_R), in $d = 3$, starting from random initial configurations, i.e., from starting temperatures $T_s = \infty$. The model is same as the one considered in **chapter 2**. Here we show that the anomalies associated with the structure, growth and aging are not unique to the case of zero temperature quench in $d = 3$. These are present over a range of low temperature. Starting from $T_f = 0$, the unexpected or anomalous features in all the nonequilibrium properties disappear when T_f approaches T_R. We show that below T_R, the deviations of λ from the theoretical value have close connection with the departures of structures from

the corresponding theoretical expectation. This points to a strong structure-dynamics connection in phase transition dynamics.

In **chapter 4** we study the effects of long range correlations in the initial configurations on the dynamics of the ordering ferromagnets in $d = 2$ and 3. We quench the Ising systems from the critical temperatures, T_c, where the equilibrium correlation length, ξ, diverges. We probe the aging, following quenches of these configurations to a T_f, via the autocorrelation function, $C_{\rm ag}(t, t_w)$. Our study shows that the decay of $C_{\rm ag}(t, t_w)$ is slower here, providing significantly smaller values of λ than the case of quenches from random initial configurations. Different values of the exponent lead to the division of universality into different classes based on the presence or absence of long range spatial correlations in the system. Through appropriate structural analysis, we show that the obtained values of λ agree with the well-known Yeung-Rao-Desai bound.

In **chapter 5** we carry out a more general study on the dependence of the coarsening dynamics on initial correlations by quenching the Ising systems from different initial temperatures, T_s, lying above T_c. It is observed that for higher values of T_s equilibration happens faster, following quenches to a fixed ferromagnetic state point. This observation has close connection with a counter-intuitive effect, referred to as the Mpemba effect (ME). By definition, ME is related to faster freezing of a hotter body of water than a colder one. Recently there are efforts to generalize it. So far, it is believed that glass-like complex energy landscape is essential for the observation of ME. Our study shows that the effect is rather universal. Note that our model Hamiltonian does not contain any glassy ingredient.

In **chapter 6** we undertake the study of the kinetics of vapor-solid phase separation in a single component Lennard-Jones system via Molecular Dynamics simulations. We present results on the dynamics of cluster growth in the system. The overall density and temperatures of the systems are set to very low values. Such choices give rise to fractality in the disconnected clusters, of which the nonequilibrium morphologies consist. Growth in such systems occurs due to collision mechanisms of various types, viz., diffusive coalescence and ballistic aggregation. We quantity the dimensionality for the above mentioned fractal structure and growth law with the variation of temperature. These results we discuss in the background of appropriate theoretical pictures.

Chapter 7 contains a study on disease spread. The context is COVID-19, a novel coronavirus disease. We analyze the infection data from different geographical regions with the help of a scaling method and comment on universality, like in phase transitions. Even though there are differences in the population density, economic background, cli-

mate, preventive measures, etc., many countries are found to exhibit a unique pattern of spread.

Finally, the **last chapter** summarizes all the works.

Publications

1. "Finite-size scaling study of aging during coarsening in non-conserved Ising model: The case of zero temperature quench", Nalina Vadakkayil, Saikat Chakraborty, and Subir K. Das, The Journal of Chemical Physics **150**, 054702 (2019).

2. "Initial correlation dependence of aging in phase separating solid binary mixtures and ordering ferromagnets", Subir K. Das, Koyel Das, Nalina Vadakkayil, Saikat Chakraborty, and Subhajit Paul, Journal of Physics: Condensed Matter **32**, 184005 (2020).

3. "Aging exponents for nonequilibrium dynamics following quenches from critical points", Koyel Das, Nalina Vadakkayil, and Subir K. Das, Physical Review E **101**, 062112 (2020).

4. "Should a hotter paramagnet transform quicker to a ferromagnet? Monte Carlo simulation results for Ising model", Nalina Vadakkayil and Subir K. Das, Physical Chemistry Chemical Physics **23**, 11186 (2021).

5. "Influence of Roughening Transition on Magnetic Ordering", Nalina Vadakkayil, Sanat K. Singha, and Subir K. Das, arXiv: 2106.16232 (2021).

6. "Dynamics of Cluster Growth during Phase Transitions in a Three-dimensional Single Component Lennard-Jones System", Nalina Vadakkayil, Sutapa Roy, and Subir K. Das, Manuscript under preparation.

7. "Study of Disease Spread via a Scaling Approach", Nalina Vadakkayil and Subir K. Das, Manuscript under preparation.

Materials in Chapters 2 and 5 have been reproduced from publication numbers 1 and 4, respectively, whereas materials in Chapter 4 have been reproduced from publication numbers 2 and 3. The copies of the documents related to permission are attached at the end of the thesis.

Table of contents

List of figures

List of tables

Chapter 1

Introduction

1.1 Phase Transition

Phase transition is commonly observed in nature during which a phase of matter changes to another with the variation in various thermodynamic parameters like pressure (P), temperature (T), density (ρ), etc. [1–5]. In more than one phases, out of the three, viz., vapor, liquid, and solid, we encounter water in everyday life. Another commonly discussed example is the transition between para and ferro phases in magnetic materials [1–5]. This thesis, in large, deals with the latter type of phase transition.

Phase transitions are classified in different ways [6]. A well-accepted classification is due to Ehernfest [6]. This is based on the discontinuity in the order of derivative in the relevant free energy. A modern classification uses the terminologies first-order and continuous phase transitions, which was put forward by Fisher [7]. The discontinuity in the first derivative marks a first-order phase transition. For a second-order or continuous transition, the first derivative is continuous, and the second-order derivative can either be divergent or discontinuous at the transition point [2, 6, 7]. This point is referred to as the critical point [7].

When an external magnetic field (H) is absent, the critical point, marking a second-order phase transition, for a para-to-ferromagnetic transition is the Curie temperature [1–5]. At this point, during the phase change, the magnetization (m) changes continuously. The phase diagram for such a transition is depicted in the $H-T$ plane in Fig. 1.1. The critical temperature, T_c, is marked in the figure. Above T_c, one has the paramagnetic phase. There, for $H = 0$, the spins in the system are randomly oriented, providing $m = 0$. When the temperature is decreased below T_c, the system changes to the ordered phase, with $m \neq 0$, referred to as the ferromagnetic phase. Such a quantity, which varies during

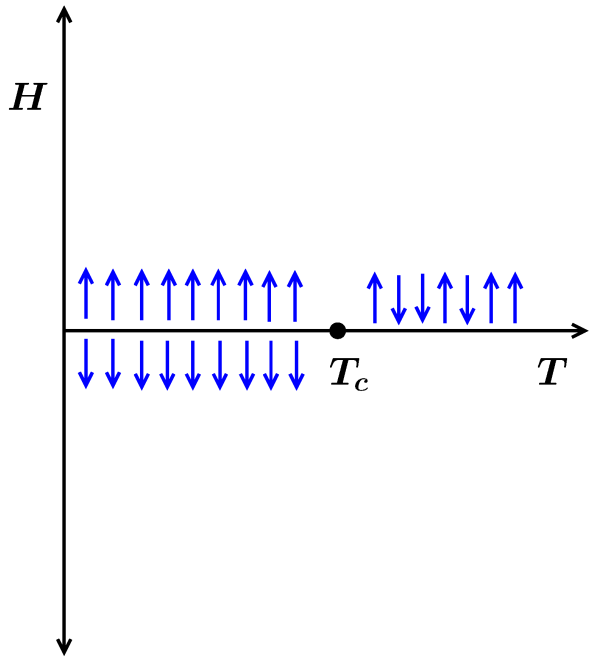

Figure 1.1: The phase diagram of a magnetic material, showing para-to-ferromagnetic transition, is schematically shown in the $H - T$ plane. The critical point is marked as T_c.

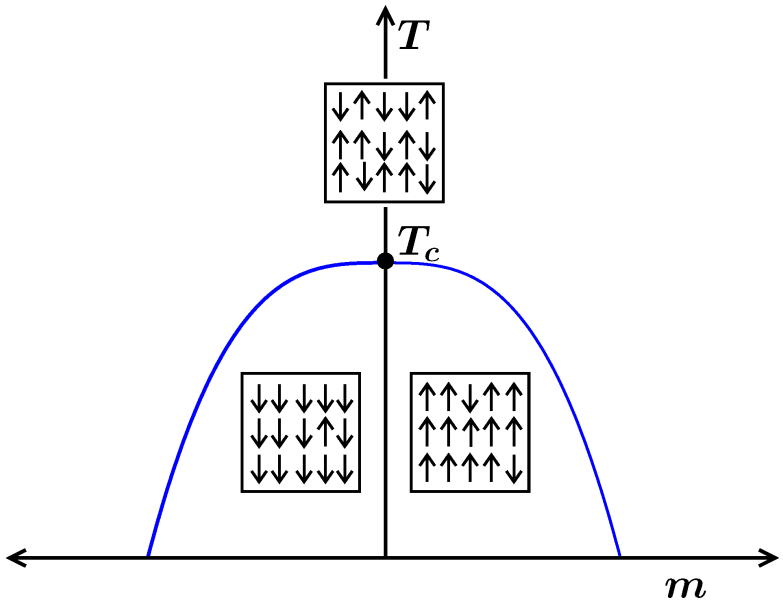

Figure 1.2: A schematic phase diagram of a magnetic material showing para-to-ferromagnetic transition in the $T - m$ plane, for $H = 0$. Above T_c, the system is in the paramagnetic phase, and m has a value zero. Below T_c, m has a non-zero value, and the system is in the ferromagnetic phase. There it lives in a state with majority of the spins aligned either up or down. These are depicted in the figure.

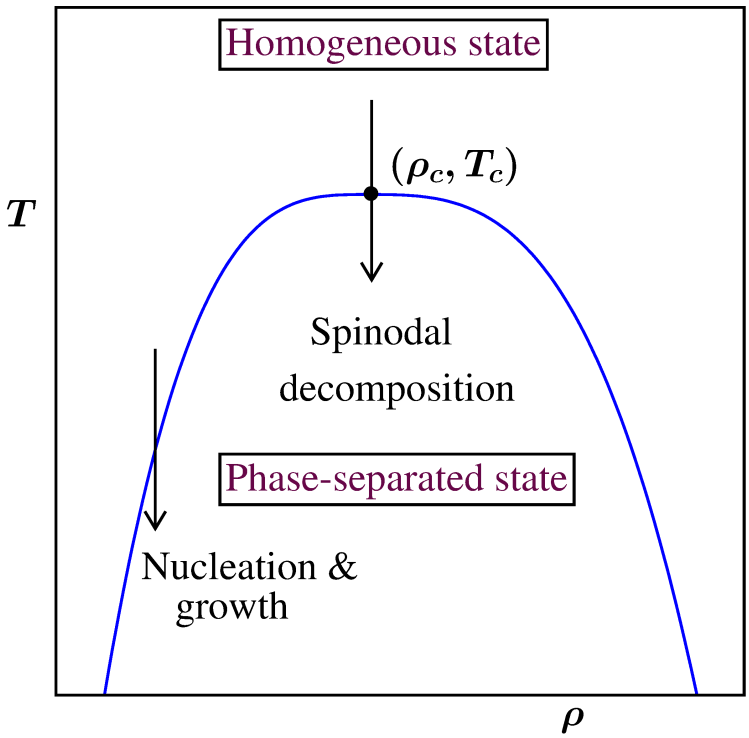

Figure 1.3: Schematic of a vapor-liquid phase transition in $T - \rho$ plane. The critical point is marked as (ρ_c, T_c). Above T_c, the system is found in a homogeneous phase. Depending on the region of quench, in the interior of the coexistence curve, it moves to a phase-separated state via different coarsening mechanisms.

a phase change, from zero to non-zero values, is referred to as the 'order parameter' [1–5]. The phase diagram for the magnetic system under discussion, for $H = 0$, in $T - m$ plane, is shown in Fig. 1.2. To represent the order parameter we will use a general symbol ψ in the following text.

In the case of vapor-liquid transition, the order parameter can well be defined as [1–5] $\psi = \rho_\ell - \rho_v$, where ρ_ℓ is the density in the liquid phase and ρ_v is that in the vapor phase. A phase diagram for vapor-liquid transition, in $T - \rho$ plane, is drawn in Fig. 1.3. The critical point is marked as (ρ_c, T_c), where ρ_c is the critical density. Above T_c, the system is in a "uniform" density state and below that one has a phase-separated state. The line which separates the two states is the coexistence curve [1–5]. Upon quenching of a homogeneous configuration inside this curve, the system moves to the coexisting equilibrium state. The word "quenching" here has the meaning of sudden change of temperature from an initial value to a final value. The evolution of the system to new equilibrium state occurs via formation and growth of regions that are rich or poor in particles of one or the other type. The evolution or coarsening mechanism [1, 5, 8]

may depend on the region of quench. A quench with, or close to, the critical density leads to the formation of interconnected domains. The corresponding growth process is referred to as the spinodal decomposition [9, 10]. For significantly off-critical quench, the coarsening progresses via nucleation and growth of disconnected clusters [10–12]. In the above phase diagram, our region of interest in the thesis will be a low density and low temperature region, below the triple point [2–4], where the disconnected solid cluster formation occurs in the vapor background [13].

Apart from these, phase transitions or analogous phenomena are common in systems of granular matter [14, 15], active matter [16, 17], etc. In each of these cases, interesting pattern of particle-rich and particle-poor clusters form. The same scenario is true in the case of disease spread in a population [18, 19] that drew significant attention recently. Here the infected individuals can form clusters. The phenomena associated with the disease spread are studied by using different mathematical models [18–20]. In one of the chapters in this thesis, we undertake a study on spread of COVID-19, that is caused by a novel coronavirus, using a recently proposed scaling method [20].

1.2 Coarsening Dynamics

As stated above, during the evolution or relaxation of a system to a new equilibrium state point inside the coexistence curve, domain formation occurs. These domains grow or 'coarsen' via the reduction of interface areas [1, 8]. The average size of domains at a time t, which will be denoted by $\ell(t)$, can, in general, be described as a power-law [1, 8] in time:

$$\ell(t) \sim t^{\alpha}. \tag{1.1}$$

The exponent α, in the above quoted power-law, depends on the type of dynamics, the number of components of the order parameter, the dimension of the system, etc. [1]. Based on the relation of the total value of the order parameter with time, the dynamics can be broadly classified into two categories, viz., the nonconserved and the conserved order-parameter dynamics. We discuss the typical growth mechanisms in systems belonging to each of these categories in the following subsections.

1.2.1 Growth in systems with nonconserved dynamics

In systems with the nonconserved order-parameter (NCOP) dynamics, the total value of the order parameter can change during a phase transition [1]. This class of systems

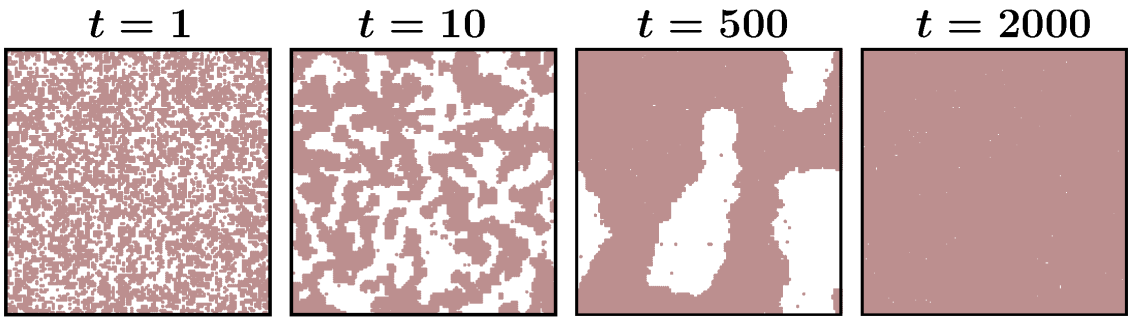

Figure 1.4: The evolution snapshots, from different times (t), of a system exhibiting nonconserved order-parameter dynamics. The quenching is done from a disordered state to a temperature below T_c ($= 0.6T_c$). The colored regions represent the locations of the up-spins. The results are obtained from the Monte Carlo simulations of 2D Ising ferromagnet using the Glauber spin-flip method for a system of size 128×128.

belongs to Model A. This is according to the classification procedure of Hohenberg and Halperin [21]. A well-known example from this class is a magnetic material that undergoes para-to-ferromagnetic transition. As already mentioned, the order parameter here is the magnetization, m. These systems can be studied via the kinetic Ising model [1, 5]. The Hamiltonian of the latter is written as

$$H = -J \sum_{\langle ij \rangle} S_i S_j; \;\; S_i = \pm 1. \tag{1.2}$$

Here J represents the interaction strength and is positive for ferromagnetic ordering. The angular bracket, $\langle ij \rangle$, implies that the summation is only over the nearest neighbor spins (S_i). The values of S_i, $+1$ and -1, correspond to up and down spins, respectively. Typical evolution morphology for this case is presented in Fig. 1.4, obtained via the Monte Carlo simulation [22, 23] using Glauber spin-flip mechanism [24], for a quench below the critical point, starting from a random initial configuration. The colored regions mark the locations of the up spins. On the other hand, the down spins are located in the unmarked regions.

The coarse-grained counterpart of the above model is the time dependent Ginzburg-Landau (TDGL) equation [1, 5]. The latter is written as

$$\frac{\partial \psi(\vec{r}, t)}{\partial t} = a\psi(\vec{r}, t) - b\psi^3(\vec{r}, t) + c\nabla^2 \psi(\vec{r}, t). \tag{1.3}$$

Here $\psi(\vec{r}, t)$ is a continuous coarse-grained order parameter, that depends upon space and time. This quantity can be obtained by averaging the spin values over spatial

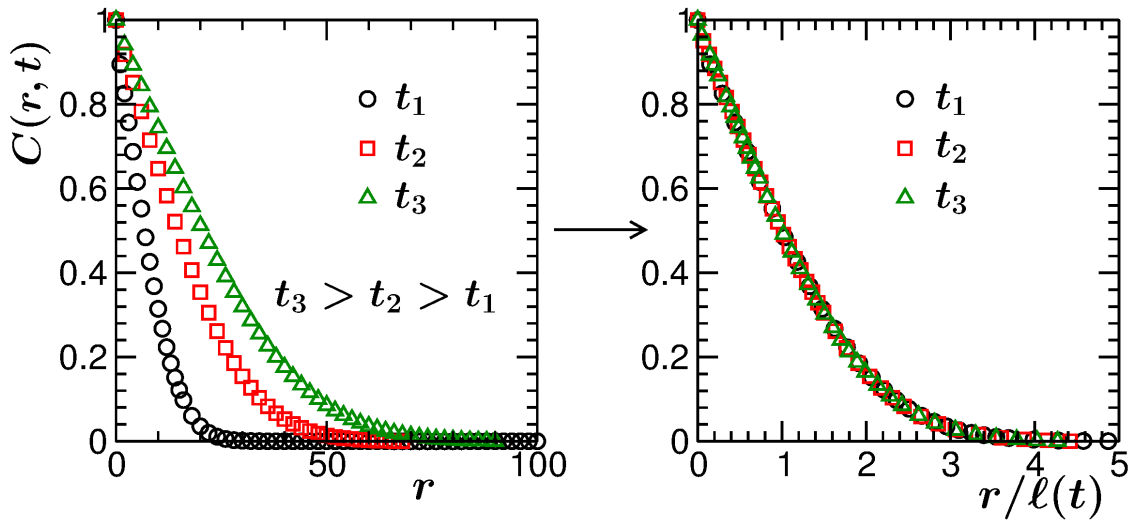

Figure 1.5: The plots of correlation function, $C(r,t)$, for a nonconserved system, are shown in the left panel and corresponding scaling is depicted inside the right frame. Note that $\ell(t)$ represents the domain length at time t.

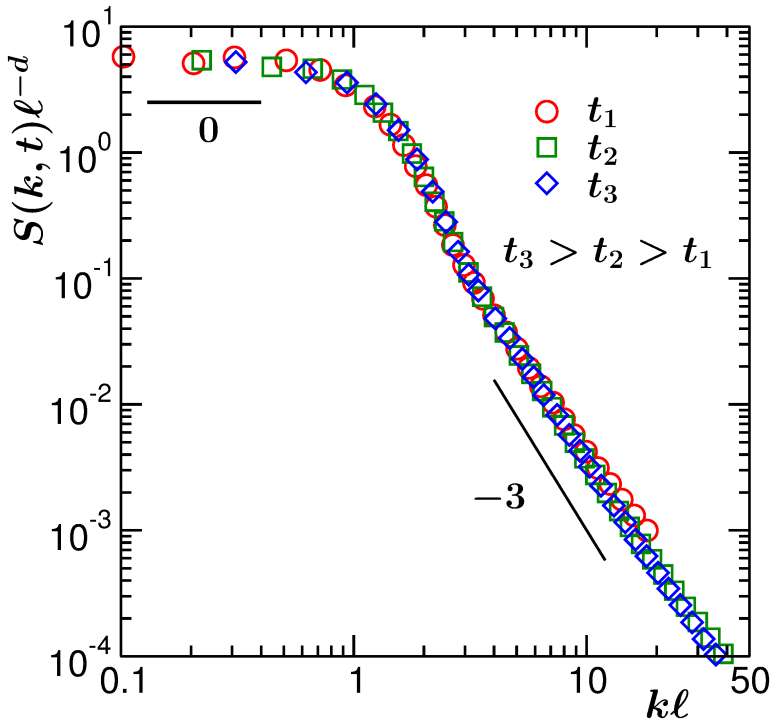

Figure 1.6: Plots of $S(k,t)\ell^{-d}$ as a function of $k\ell$ in a log-log scale, for the NCOP dynamics, for quenches from random initial configurations with zero magnetization to $0.6T_c$. The solid lines are the power-laws with exponents mentioned near them. In the small-k limit, the exponent, β, has the value 0. The exponent corresponding to the Porod law is also mentioned in the figure.

blocks of different sizes. The coefficients a, b and c are temperature dependent positive constants below T_c. By solving the above equation, one can study the pattern formation and coarsening in systems having the NCOP dynamics.

The domain growth in these systems is *curvature-driven* [1]. The velocity, v, of the domain walls is related to the local curvature K as [1, 25]

$$v = -K. \tag{1.4}$$

This is known as the Allen-Cahn equation [1, 25]. In terms of the characteristic length scale, ℓ, Eq. (1.4) can be written as

$$v \sim \frac{d\ell}{dt} \sim \frac{1}{\ell}, \tag{1.5}$$

which gives

$$\ell(t) \sim t^{1/2}. \tag{1.6}$$

This is the well-known Allen-Cahn growth law [25]. The exponent here does not depend on the space dimension, d.

The domain length can be calculated by using the scaling property of various structural quantities, i.e., the two-point equal-time correlation function, $C(r,t)$, defined as [1]

$$C(r,t) = \langle \psi(\vec{r},t)\psi(\vec{0},t)\rangle - \langle \psi(\vec{r},t)\rangle\langle \psi(\vec{0},t)\rangle;\ r = |\vec{r}|. \tag{1.7}$$

During the evolution of a system if the domain morphology at different times are statistically similar, other than a change in length scale, these structures are said to be self-similar. In that case, $C(r,t)$ attains a scaling form [1]

$$C(r,t) \equiv \tilde{C}(r/\ell(t)). \tag{1.8}$$

The scaling of $C(r,t)$, for the nonconserved order-parameter dynamics, is depicted in Fig. 1.5. The data sets are obtained via the Monte Carlo simulations for a ferromagnetic system following a quench from very high temperature to a temperature below T_c in $d = 2$. The left panel shows $C(r,t)$ from different times during the evolution. The data collapse is obtained by scaling the abscissa variable by the characteristic length scales at given times. The length scale here corresponds to the average domain length of the system. This scaling picture is shown in the right frame of Fig. 1.5.

The Fourier transform of $C(r,t)$, which is known as the structure factor, $S(k,t)$, can also be probed for studying the morphology of the system [1]. The scaling form of $S(k,t)$ can be written as [1, 5]

$$S(k,t) \equiv \ell^d \tilde{S}(k\ell). \tag{1.9}$$

$S(k,t)$ in the large k limit shows a power-law behavior, referred to as the Porod law [1], viz., one observes

$$S(k,t) \sim k^{-(d+n)}, \tag{1.10}$$

where n stands for the number of order-parameter components. For a scalar order parameter, which is the only case considered in this thesis, the above relation reduces to $S(k,t) \sim k^{-(d+1)}$.

The small-k behavior of $S(k,t)$ can also be written as a power-law [26] with an exponent β, i.e.,

$$S(k \to 0,t) \sim k^{\beta}. \tag{1.11}$$

The value of β for the considered NCOP dynamics is in general known to be zero [26, 27]. A plot of scaled structure factor for the NCOP dynamics is shown in Fig. 1.6. Again, the data are obtained from the Monte Carlo simulations of the kinetic Ising model, in $d = 2$, for a quench below T_c. The power-laws corresponding to small-k behavior and the Porod law are shown there.

1.2.2 Growth in systems with conserved dynamics

In the conserved order-parameter (COP) dynamics, the system integrated order-parameter remains unchanged during a phase transition [1]. One well-known example is the phase separation in binary alloys which can be studied via the Ising model with the Kawasaki exchange kinetics [28]. This belongs to Model B category [21]. In the Kawasaki dynamics, the neighboring particles exchange positions during the Monte Carlo simulation runs. The snapshots of a system of binary (A+B) mixture, taken during the course of a Monte Carlo simulation run of the stated model, are shown in Fig. 1.7, for a quench to a temperature below T_c. The colored and empty regions are related to the locations of A and B particles, respectively.

At the coarse-grained level, the above phenomenon can be studied via the Cahn-Hilliard equation which can be written as [1, 5]

$$\frac{\partial \psi(\vec{r},t)}{\partial t} = -\nabla^2 \left[a\psi(\vec{r},t) - b\psi^3(\vec{r},t) + c\nabla^2\psi(\vec{r},t) \right], \tag{1.12}$$

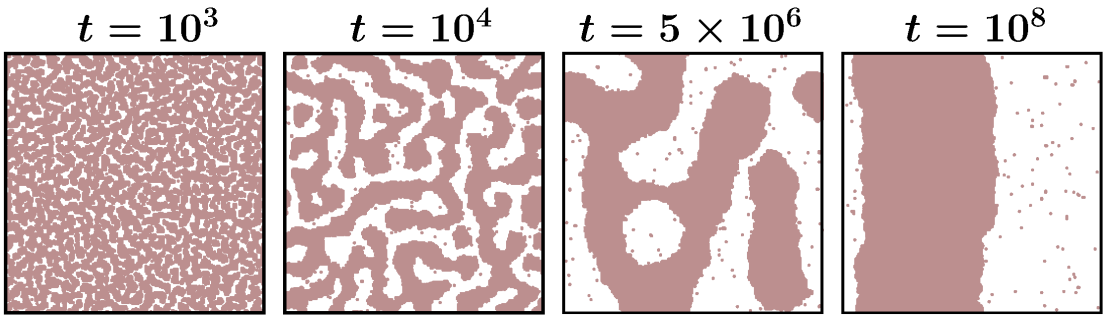

Figure 1.7: The evolution snapshots of a two-dimensional system of binary (A+B) mixture which undergoes phase separation. This system follows the conserved order-parameter dynamics. The results are from the Monte Carlo simulation of the Ising model with Kawasaki dynamics. The colored regions contain the A particles and the empty regions, B particles.

where the parameters a, b, and c are temperature dependent constants, same as in the case of TDGL equation.

The Lifshitz-Slyozov-Wagner (LSW) theory describes the domain growth in these systems [29, 30]. The domains grow via the evaporation of small droplets and condensation of corresponding mass onto the larger droplets. In this particle diffusion process, the interface velocity scales as $|\nabla\mu|$, where μ is the chemical potential. At the interface $\mu \sim \gamma/\ell$, γ being the surface tension. So the interface velocity can be written as

$$\frac{d\ell}{dt} \sim \frac{1}{\ell^2}. \tag{1.13}$$

An integration provides the power-law growth

$$\ell(t) \sim t^{1/3}. \tag{1.14}$$

This is the LSW growth law [29, 30].

In fluids, the growth dynamics is rather complex [9–13]. Because of the influence of hydrodynamics, the late time growth will be faster [9, 12, 31, 32]. This type of systems belong to the class of Model H [21]. The growth in such systems is diffusive in the early time regime, and the power-law exponent obeys the LSW value [29, 30], viz., $\alpha = 1/3$. Beyond a certain time, when ℓ crosses a critical number, hydrodynamics becomes important, and the growth exponent attains a value [9] $\alpha = 1$. This regime is referred to as the viscous hydrodynamic regime. At much later time, inertia dominates and the growth exponent crosses over to a value [12] $\alpha = 2/3$. This is known as the

inertial hydrodynamic regime. This overall picture we summarize as follows [1]:

$$\ell(t) \sim \begin{cases} t^{1/3}, & \text{diffusive regime,} \\ t, & \text{viscous hydrodynamic regime,} \\ t^{2/3}, & \text{inertial hydrodynamic regime.} \end{cases} \tag{1.15}$$

This picture applies to interconnected domain morphology. For much off-critical quenches, for which disconnected cluster morphologies emerge, manifestation of hydrodynamics occurs in a different way. This we will discuss later.

1.2.3 Aging Phenomena

Further information on relaxation of a system during a nonequilibrium process can be obtained via two-time quantities. An example of such a quantity is the autocorrelation function, defined as [5, 27, 33–36]

$$C_{\rm ag}(t, t_w) = \langle \psi_i(t)\psi_i(t_w)\rangle - \langle \psi_i(t)\rangle\langle \psi_i(t_w)\rangle. \tag{1.16}$$

Here t_w is the time at which an observation starts. This is referred to as the waiting time or age of the system. Note that t ($\geqslant t_w$) here is the observation time. For a system at equilibrium, $C_{\rm ag}(t, t_w)$ from different t_w values overlap with each other when plotted versus the translated time, i.e., $t - t_w$. This property is referred to as the *time translation invariance* [5]. For aging in considered nonequilibrium systems, the relaxation of an older system is slower than the younger ones, giving rise to the violation of time translation invariance. Schematic plots depicting this fact are shown in Fig. 1.8. It can be seen there that the decay of $C_{\rm ag}(t, t_w)$ slows down with the increase in the t_w values. However, for large t_w values and when $t \gg t_w$, $C_{\rm ag}(t, t_w)$ from different t_w scale with t/t_w or ℓ/ℓ_w as [33, 34]

$$C_{\rm ag}(t, t_w) \sim (\ell/\ell_w)^{-\lambda} \sim (t/t_w)^{-\lambda\alpha}, \tag{1.17}$$

where ℓ and ℓ_w represent the domain lengths at t and t_w, respectively. The exponent λ is the aging exponent.

The values of λ, for the systems with NCOP dynamics, typically follow the bounds predicted by Fisher and Huse (FH) [34]:

$$\frac{d}{2} \leqslant \lambda \leqslant d. \tag{1.18}$$

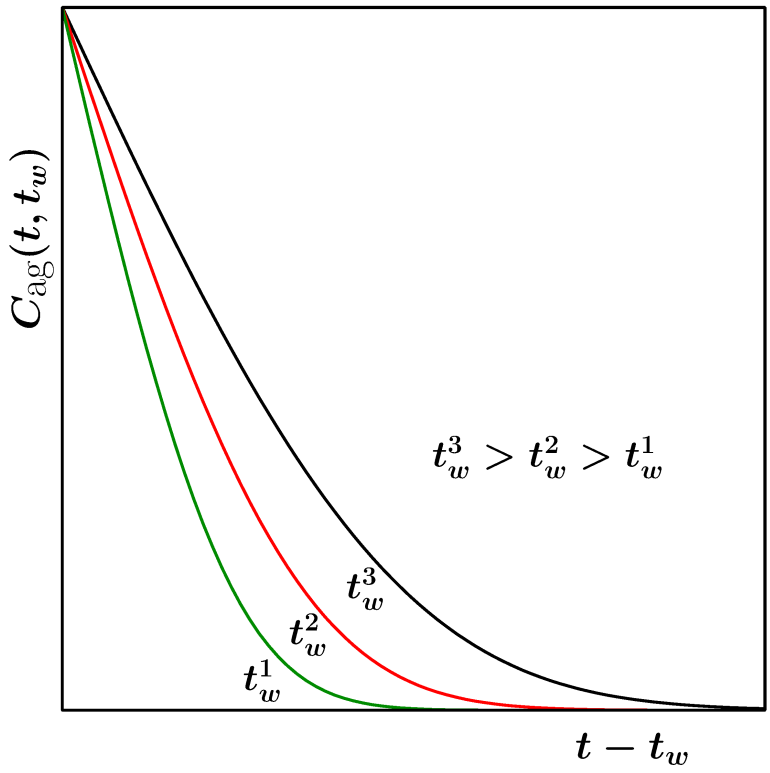

Figure 1.8: Schematic plots of $C_{\rm ag}(t, t_w)$, versus $t - t_w$, for different t_w values. For larger t_w values relaxation is slower than the ones with the smaller t_w values. This violates the time translation invariance.

Later, a more general lower bound was introduced by Yeung, Rao and Desai (YRD) in the context of COP dynamics [27], that reads

$$\lambda \geqslant \frac{d+\beta}{2}. \tag{1.19}$$

In the case of typical NCOP dynamics, the value of β is 0, as shown in Fig. 1.6. So, in this case both FH and YRD lower bounds turn out to be the same. But for the COP dynamics the value of β can differ significantly from the above mentioned value [26, 27]. In this case β is 2 in $d = 1$, and $\beta = 4$ in $d = 2$ and 3, for typical Ising-like systems. Detailed discussions about the values of β in different situations during NCOP dynamics can be found in later chapters.

Another important nonequilibrium aspect of phase transition is persistence of order-parameter. A probability, $P(t)$, referred to as the persistence probability, in this context is defined as the fraction of unperturbed particles or spins till time t [37, 38]. This

quantity also exhibits interesting power-law behavior:

$$P(t) \sim t^{-\theta}, \tag{1.20}$$

where θ is referred to as the persistence exponent. In the literature there have been much interest in the estimation of this exponent [37–40].

In most studies of kinetics of phase transition the focus has been on late time behavior. In critical phenomena, understanding of the corrections to the critical exponents, when a system is far away from the critical point, has been obtained via advanced methods. Early time behavior in kinetics can contain analogous corrections. These have received only limited attention [41].

1.3 Computational Techniques

Main computational tools that we have used for carrying out various studies are the Monte Carlo [22, 23, 42] and Molecular Dynamics [42, 43] simulation techniques. Brief descriptions of these methods are given below.

1.3.1 Monte Carlo Simulation

In the Monte Carlo (MC) method, the sampling of the states is done in a stochastic manner, with the help of the random number generation [22, 23, 42]. Different properties of a system can be calculated by sampling the relevant regions of phase space and taking the averages over many such samples. The accuracy of the MC method lies in the number of such samples.

In this thesis, we have used the MC method to study the para-to-ferromagnetic transition with the help of the nearest neighbor Ising model [1] with Glauber dynamics [24]. Two different algorithms we have used for various studies. These are Metropolis [44] and Glauber algorithms [24]. These algorithms differ from each other by the definition of the transition probability [22]. Using the transition probabilities, in MC methods, the state of a system at a given time can be obtained from that at the previous time step. The process is *Markovian*, i.e., the system's current state doesn't depend on its history [22, 23]. In these processes the *detailed balance condition* implies that the system is in equilibrium. This condition is expressed as [22, 23]

$$P_n \pi_{n\to m} = P_m \pi_{m\to n}. \tag{1.21}$$

Here, P_n is the probability of the system to be at the n^{th} state and $\pi_{n\to m}$ is the transition probability of the system for going from the state n to m [22, 23]. The transition probability may be separated into two parts [22, 23]:

$$\pi_{n\to m} = g_{n\to m} \times W_{n\to m}, \tag{1.22}$$

where $g_{n\to m}$ is the probability of the generation of a state m given that the present state is n, and $W_{n\to m}$ is the probability with which the state m gets accepted from a state n. The latter is called the acceptance probability. We can consider g to be symmetric and rewrite the expression for detailed balance condition as [22, 23]

$$P_n W_{n\to m} = P_m W_{m\to n}. \tag{1.23}$$

The probability, P_n, for a system, with the partition function Z, having energy E_n at the n^{th} state, can be written as [22, 23]

$$P_n = \frac{\exp(-E_n/k_B T)}{Z}, \tag{1.24}$$

where k_B is the Boltzmann constant. Here the ratio of the probabilities of the system being at two states n and m will depend on the energy difference between them, i.e., $\exp(-\Delta E/k_B T)$. By satisfying the detailed balance condition, the acceptance probability for the Metropolis algorithm is given by [44]

$$W(n \to m) = \min(1, \exp(-\Delta E/k_B T)). \tag{1.25}$$

The acceptance probability for the Glauber algorithm is given by [24]

$$W(n \to m) = 1 + S_i \tanh(E_i/k_B T), \tag{1.26}$$

where E_i is the energy of the spin at the i^{th} site in a state n.
The steps followed for the implementation of the MC method in the Glauber Ising model are given below [22, 23]:

1. Generate an initial spin configuration.

2. Choose a site randomly and flip the spin at that site. This is a trial move. Calculate the energy before and after this trial move.

3. Generate a random number, say, r, lying between 0 and 1. If $r \leq$ acceptance probability, accept the move in step (2). If not, flip the spin back to the previous state.

4. Repeat steps (2) and (3) for L^d times, where L is the length and d is the dimensionality of the system. The L^d trial moves make one Monte Carlo step (MCS), a typical unit of time.

Wolff Algorithm

Near the critical point, the systems encounter severe slowing down [21]. In this region of the phase diagram, relaxation becomes very slow due to the diverging correlation length, ξ ($\sim |T - T_c|^{-\nu}$). The corresponding time scale, τ, diverges as [3, 45]

$$\tau \sim \xi^z, \tag{1.27}$$

where z is a dynamic critical exponent. In computers, one works with finite systems, and so, the correlation length is bounded by the linear dimension of the system, say, L. Thus, at the critical point one writes Eq. (1.27) as [45]

$$\tau \sim L^z. \tag{1.28}$$

For the Glauber Ising model the value of z is $\simeq 2.18$ in [46, 47] $d = 2$ and $\simeq 2.03$ in [46] $d = 3$. It is evident that as the linear dimension of the system increases, the system relaxes slower and slower. To avoid this, one can use cluster algorithms instead [48], if dynamics is not of concern. In this thesis, we used the Wolff cluster algorithm [49] for obtaining equilibrium configurations near the critical point. The algorithm is described below [49]:

1. Pick a site i randomly from the lattice.

2. Identify the nearest neighbors with a similar spin value and form the bonds between them with a probability $1-\exp(-2\beta J)$. All the spins connected with bonds belong to a single cluster.

3. Repeat step (2) for each connected spin and add it to the cluster until all such spins are placed inside it.

4. Flip the whole cluster. This is one Wolff step.

An important feature of the Wolff algorithm is that this is a rejection-free method. Due to this, the relaxation time decreases, making the simulation more efficient near T_c.

1.3.2 Molecular Dynamics Simulation

We use molecular dynamics (MD) simulations for studying kinetics of phase transition in a system described by the Lennard-Jones (LJ) potential of the form [42, 43]

$$U(r) = 4\varepsilon \left[\left(\frac{\sigma}{r}\right)^{12} - \left(\frac{\sigma}{r}\right)^{6} \right]. \tag{1.29}$$

Here ε is the interaction strength, σ is the diameter of the particles, and r is the inter-particle distance. In our simulations we have used a truncated, shifted and force corrected LJ potential [50]:

$$\tilde{U}(r) = U(r) - U(r_c) - (r - r_c) \left(\frac{dU}{dr}\right)_{r=r_c}, \tag{1.30}$$

with the cut-off distance, r_c, chosen to be 2.5σ.

MD simulation is typically a deterministic method [42, 43], where the positions and velocities of the particles in a many-body system are determined by solving the Newton's equations of motion. Different algorithms exist to solve these equations. We have used the well-known velocity Verlet algorithm [42, 43]. In this scheme, the position and the velocity of the i^{th} particle are effectively updated via the equations [42, 43]

$$\vec{r}_i(t + \Delta t) = \vec{r}_i(t) + \vec{v}_i(t)\Delta t + \frac{\vec{f}_i(t)}{2m_i}\Delta t^2, \tag{1.31}$$

and

$$\vec{v}_i(t + \Delta t) = \vec{v}_i(t) + \frac{\vec{f}_i(t + \Delta t) + \vec{f}_i(t)}{2m_i}\Delta t. \tag{1.32}$$

In the above equations $\vec{r}_i$, $\vec{v}_i$, m_i, and $\vec{f}_i$ represent the position, velocity, mass and force of or on the i^{th} particle in the system. The force $\vec{f}_i$ can be determined from the gradient of the potential of the i^{th} particle due to the others, i.e., $\vec{f}_i = -\vec{\nabla} U_i$.

Computing the force for each pair of particles in the MD simulations is much time consuming task. To reduce this computational time, we have used the Verlet list and cell list algorithms [42, 43]. For the Verlet list, we tabulate the neighbors within a cut-off radius r_v ($r_v > r_c$) for each particle in the system. This makes the simulation less time-

consuming since the number of pairs to be considered for the force calculation reduces considerably. In the case of cell list, the lattice, say simple cubic, of linear dimension L, is divided into smaller lattices of dimension $\ell_{cell} \times \ell_{cell} \times \ell_{cell}$ such that $L/\ell_{cell} > r_c$. A list can be made for each of the cells, again making the force calculation faster.

The MD simulations are also performed in the canonical ensemble, where the temperature control can be done by using different thermostats. A widely used temperature controller is the Nosé-Hoover thermostat [51, 52], which is considered good for preserving hydrodynamics in the system. We have used the same for our simulations.

Nosé-Hoover Thermostat

This is based on an extended Lagrangian formalism [51, 52], where an additional coordinate (a virtual variable), s, with an effective mass, Q, is introduced in the Lagrangian of an N-body system. The modified equations of motion in this formalism are [51, 52]

$$\dot{\vec{r}_i} = \vec{p}_i/m_i, \tag{1.33}$$

$$\dot{\vec{p}_i} = -\frac{\partial U(\vec{r}^N)}{\partial r_i} - \zeta \vec{p}_i, \tag{1.34}$$

and

$$\dot{\zeta} = \frac{1}{Q}\left(\sum_i \frac{\vec{p}_i^2}{m_i} - 3Nk_BT\right). \tag{1.35}$$

The parameter ζ is a friction coefficient and is defined as $\zeta = \dot{s}/s$. Modified position and velocity update equations within the Verlet algorithm with the Nosé-Hoover formalism can then be written as [51, 52]

$$\vec{r}_i(t+\Delta t) = \vec{r}_i(t) + \vec{v}_i(t)\Delta t + \left[\frac{\vec{f}_i(t)}{m_i} - \zeta(t)\vec{v}_i(t)\right]\frac{\Delta t^2}{2}, \tag{1.36}$$

$$\begin{aligned}\vec{v}_i(t+\Delta t) =& \vec{v}_i(t) + \frac{\Delta t}{2}\left[\frac{\vec{f}_i(t)}{m_i} + \frac{\vec{f}_i(t+\Delta t)}{m_i} - 2\zeta(t)\vec{v}_i(t)\right] \\ &- \frac{\Delta t^2}{2}\left[\frac{\zeta(t)}{2}\left(\frac{\vec{f}_i(t)}{m_i} + \frac{\vec{f}_i(t+\Delta t)}{m_i} - 2\zeta(t)\vec{v}_i(t)\right)\right. \\ &\left. + \vec{v}_i(t)\left(\sum_j \vec{v}_j(t)^2 - 3Nk_BT\right)/Q\right].\end{aligned} \tag{1.37}$$

To carry out "some" of the MD simulations, we have used the Large-scale Atomic/ Molecular Massively Parallel Simulator (LAMMPS) [53, 54] package.

1.4 Finite-size Scaling Analysis

In computer simulations, the finiteness of a system does not allow quantities to grow indefinitely. To overcome such finite-size effects, one can use finite-size scaling (FSS) analysis in the studies of both equilibrium and non-equilibrium properties of a system [55]. Let us consider the equilibrium critical phenomena. The critical singularity of any thermodynamic quantity, X, can be written as [7]

$$X = X_0 \epsilon^{-x}, \tag{1.38}$$

where X_0 is the critical amplitude, ϵ is the reduced temperature $[= (T - T_c)/T_c]$ and x is the critical exponent. E.g., the blowing up of the correlation length, ξ, in terms of ϵ, is written as [7],

$$\xi \sim \epsilon^{-\nu}. \tag{1.39}$$

Combining Eqs. (1.38) and (1.39) one obtains

$$X \sim \xi^{x/\nu}. \tag{1.40}$$

Since we always deal with finite systems in computers, ξ will be limited by the system size at T_c. So, Eq. (1.40) reduces to

$$X \sim L^{x/\nu}. \tag{1.41}$$

One can then introduce a scaling function $Y(y)$ in the above equation [55]:

$$X = Y(y) L^{x/\nu}, \tag{1.42}$$

with y being the scaling variable, which is a dimensionless quantity [say, $= (L/\xi)^{1/\nu}$]. $Y(y)$ can be appropriately derived or constructed such that, in the limit $y \to 0$, $Y(y) \to$ constant, and when $y \to \infty$, $Y(y) \sim y^{-x}$, satisfying the thermodynamic limit singularity when $\xi << L$. By exploring different system sizes and obtaining the best collapse of data for $Y(y)$, one can acquire knowledge about the behavior of a quantity in the large system size limit.

In an analogous manner FSS can be formulated for nonequilibrium growth problems [56]. Note that FSS analysis can also be used for extracting crucial finite-size properties of various systems. One such example is concerning the utility of FSS in the study of disease spread in a population [20]. A brief description of this is given below.

Finite-size scaling in the context of disease spread

For an epidemic, the natural early time pattern of infection is of the exponential form [57]

$$N = N_0 \exp(mt), \tag{1.43}$$

where N is the infected population at time t, and N_0 and m are constants. Suppose N_s is the population that gets infected when the infection spreading pattern deviates from its exponential behavior. This is similar to the appearance of finite-size effects and connected to the limiting number of infections when the spread has stopped. By using this fact and following steps similar to the equilibrium case above, a scaling ansatz can be formulated as [20]

$$\ln n = Y(y) \ln n_s, \tag{1.44}$$

where $n = N/N_0$, $n_s = N_s/N_0$, and $y = \ln n_s/mt$. Here $Y(y) \to$ constant as $y \to 0$, and $Y(y) \sim y^{-1}$ as $y \to \infty$.

1.5 Overview of the Thesis

In this thesis, we study various nonequilibrium properties of a few systems exhibiting different kinds of phase transitions. Even though the Synopsis contains similar information below we repeat the overview of the thesis very briefly.

In chapters 2, 3, 4, and 5, our study is focused on various properties of the ordering Ising ferromagnet. The main objective of chapters 2 and 3 is to identify and understand the anomalous behavior of aging during zero and other low-temperature quenches.

The aging properties in these systems also get influenced by the spatial correlations present in the initial structures. In this regard, in chapter 4, we study aging in the specific cases of quenches from critical temperatures, T_c, and compare the results for quenches from infinite temperature.

In chapter 5, a more systematic study on the dependence of coarsening dynamics on the initial correlation is carried out. This study has connection with a counter-intuitive effect referred to as the Mpemba effect [58, 59]. The latter is related to faster freezing of a

hotter body of water than a colder one [58]. We investigate the presence of similar effect in ferromagnetic ordering. For all the studies mentioned above, we have used Monte Carlo simulations [22]. In each of the cases there was no constraint on the conservation of the order parameter over time.

Chapter 6 contains the study of the kinetics of vapor-solid phase transition, for which the order parameter is a conserved quantity. Here we consider a single component Lennard-Jones system to study the formation and growth of fractal clusters in this system. For this we perform molecular dynamics simulations in hydrodynamic environment.

The last chapter contains results on disease spread in a population. Here we undertake a scaling analysis of COVID-19 data by using a recently developed finite-size scaling method in this context [20]. One of the objectives here is to identify universal features of the spread.

References

[1] A.J. Bray, Adv. Phys. **51**, 481 (2002).

[2] H.E. Stanley, *Introduction to Phase Transitions and Critical Phenomena* (Clarendon Press, Oxford, 1971).

[3] A. Onuki, *Phase Transition Dynamics* (Cambridge University Press, Cambridge, 2002).

[4] N. Goldenfeld, *Lectures on Phase Transitions and the Renormalization Group* (West view press, 1992).

[5] *Kinetics of Phase transition*, edited by S. Puri and V. Wadhawan (CRC Press, Boca Raton, 2009).

[6] G. Jarger, Arch. Hist. Exact Sci. **53**, 5 (1998).

[7] M.E. Fisher, Rep. Prog. Phys. **30**, 615 (1967).

[8] A.J. Bray, Phil. Trans. R. Soc. Lond. A **361**, 781 (2003).

[9] E.D. Siggia, Phys. Rev. A **20**, 595 (1979).

[10] K. Binder, Phys. Rev. B **15**, 4425 (1977).

[11] K. Binder and D. Stauffer, Phys. Rev. Lett. **33**, 1006 (1974).

[12] H. Furukawa, Phys. Rev. A **31**, 1103 (1985).

[13] J. Midya and S.K. Das, Phys. Rev. Lett. **118**, 165701 (2017).

[14] I.S. Aranson and L.S. Tsimring, Rev. Mod. Phys. **78**, 641 (2006).

[15] S. Paul and S.K. Das, Europhys. Lett. **108**, 66001 (2014).

[16] T. Vicsek, A. Czirôk, E. Ben-Jacob, I. Cohen, and O. Schochet, Phys. Rev. Lett. **75**, 1226 (1995).

[17] M.C. Marchetti, J.F. Joanny, S. Ramaswamy, T.B. Liverpool, J. Prost, M. Rao, and A. Simha, Rev. Mod. Phys. **85**, 1143 (2013).

[18] W.O. Kermack and A.G. McKendrick, Proc. R. Soc. A **115**, 700 (1927).

[19] R.M. Anderson, in *Population Dynamics of Infectious Diseases: Theory and Applications*, edited by R.M. Anderson (Chapman and Hall, New York, 1982), pp. 1-37.

[20] S.K. Das, Proc. R. Soc. A **477**, 20200689 (2021).

[21] P.C. Hohenberg and B.I. Halperin, Rev. Mod. Phys. **49**, 435 (1977).

[22] D.P. Landau and K. Binder, *A Guide to Monte Carlo Simulations in Statistical Physics* (Cambridge University Press, Cambridge, 2009).

[23] M.E. Newman and G.T. Barkema, *Monte Carlo Methods in Statistical Physics* (Clarendon Press, Oxford, 1999).

[24] R.J. Glauber, J. Math. Phys. **4**, 294 (1963).

[25] S.M. Allen and J.W. Cahn, Acta Metall. **27**, 1085 (1979).

[26] C. Yeung, Phys. Rev. Lett. **61**, 1135 (1988).

[27] C. Yeung, M. Rao, and R.C. Desai, Phys. Rev. E **53**, 3073 (1996).

[28] K. Kawasaki, in *Phase Transition and Critical Phenomena*, edited by C. Domb and M.S. Green (Academic, New York, 1972), Vol. 2, p. 443.

[29] I.M. Lifshitz and V.V. Sloyozov, J. Phys. Chem. Solids **19**, 35 (1961).

[30] C. Wagner, Z. Elektrochem. **65**, 581 (1961).

[31] S. Ahmad, S.K. Das, and S. Puri, Phys. Rev. E **85**, 031140 (2012).

[32] S.K. Das, S. Roy, and J. Midya, C. R. Phys. **16**, 303 (2015).

[33] F. Liu and G.F. Mazenko, Phys. Rev. B **44**, 9185 (1991).

[34] D.S. Fisher and D.A. Huse, Phys. Rev. B **38**, 373 (1988).

[35] J. Midya, S. Majumder, and S.K. Das, J. Phys.: Condens. Matter **26**, 452202 (2014).

[36] S. Chakraborty and S.K. Das, Europhys. Lett. **119**, 50005 (2017).

[37] S.N. Majumdar, C. Sire, A.J. Bray, and S.J. Cornell, Phys. Rev. Lett. **77**, 2867 (1996).

[38] G. Manoj and P. Ray, Phys. Rev. E **62**, 7755 (2000).

[39] S. Chakraborty and S.K. Das, Eur. Phys. J. B **88**, 160 (2015).

[40] P. Mullick and P. Sen, Phys. Rev. E **93**, 052113 (2016).

[41] S. Majumder and S. K. Das, Phys. Chem. Chem. Phys. **15**, 13209 (2013).

[42] D. Frenkel and B. Smit, *Understanding Molecular Simulations: From Algorithms to Applications* (Academic Press, San Diego, 2002).

[43] M.P. Allen and D.J. Tildesley, *Computer Simulations of Liquids* (Clarendon, Oxford, 1987).

[44] N. Metropolis, A.W. Rosenbluth, M.N. Rosenbluth, A.H. Teller, and E. Teller, J. Chem Phys. **21**, 1087 (1953).

[45] M.E. Fisher, in *Critical Phenomena*, edited by M.S. Green (Academic, London, 1971) p. 1.

[46] P. Grassberger, Physica A **214**, 547 (1995).

[47] M.P. Nightingale and H.W.J. Blőte, Phys. Rev. B **62**, 1089 (2000).

[48] E. Luijten, Lect. Notes Phys. **703**, 13 (2006).

[49] U. Wolff, Phys. Rev. Lett. **62**, 361 (1989).

[50] S. Majumder and S. K. Das, Europhys. Lett. **95**, 46002 (2011).

[51] S. Nosé, J. Chem. Phys. **81**, 511 (1984).

[52] W.G. Hoover, Phys. Rev. A **31**, 1695 (1985).

[53] S. Plimpton, J. Comp. Phys. **117**, 1 (1995).

[54] http://lammps.sandia.gov.

[55] M.E. Fisher and M.N. Barber, Phys. Rev. Lett. **28**, 1516 (1972).

[56] S. Majumder and S.K. Das, Phys. Rev. E **84**, 021110 (2011).

[57] H.W. Hethcote, SIAM Rev. **42**, 599 (2000).

[58] E.B. Mpemba and D.G. Osborne, Physics Education **4**, 172 (1969).

[59] M. Jeng, Am. J. Phys. **74**, 514 (2006).

Chapter 2

Finite-Size Scaling Study of Aging during Coarsening in Nonconserved Ising Model: The case of zero temperature quench

2.1 Introduction

When a homogeneous system is quenched inside the coexistence curve, the system falls out-of-equilibrium. Here we provide a discussion of the related aspects and define the problem following Ref. [1]. During the evolution of this system towards a new equilibrium, various structural quantities exhibit interesting scaling properties [2–14]. In this context, a space-dependent order-parameter can be defined as [2, 3]

$$C(\vec{r}_1, \vec{r}_2; t) = \langle \psi(\vec{r}_1, t)\psi(\vec{r}_2, t)\rangle - \langle \psi(\vec{r}_1, t)\rangle\langle \psi(\vec{r}_2, t)\rangle, \tag{2.1}$$

with ψ being a space- and time-dependent order-parameter field. The quantity in Eq. (2.1) is known as the two-point equal-time correlation function [2, 3]. We will denote this as $C(r, t)$ with r being the scalar distance between $\vec{r}_1$ and $\vec{r}_2$ ($r = |\vec{r}_1 - \vec{r}_2|$). On the other hand, a two-time correlation function, represented by $C_{\rm ag}(t, t_w)$, can be defined with $\vec{r}_1 = \vec{r}_2$ [3]. This quantity is referred to as the two-time autocorrelation function and is written as [3, 4],

$$C_{\rm ag}(t, t_w) = \langle \psi(t, \vec{r}_1)\psi(t_w, \vec{r}_1)\rangle - \langle \psi(t, \vec{r}_1)\rangle\langle \psi(t_w, \vec{r}_1)\rangle. \tag{2.2}$$

Here t_w ($\leq t$) is referred to as the waiting time or the age of the system. It is worth mentioning that $C_{\rm ag}(t, t_w)$ is used for the study of aging in the nonequilibrium systems [3, 4] and may contain information on relaxation related to equilibration inside individual domains as well.

For self-similar structures, $C(r, t)$ typically exhibits the scaling behavior [2, 3, 10]

$$C(r, t) \equiv \tilde{C}(r/\ell(t)), \tag{2.3}$$

where $\ell(t)$ is a characteristic length scale of the system which grows in a power-law manner [2], with exponent α, as

$$\ell \sim t^{\alpha}. \tag{2.4}$$

The Fourier transform of $C(r, t)$ is the structure factor, $S(k, t)$, scaling form of which can be written as,

$$S(k, t) \equiv \ell^d \tilde{S}(k\ell), \tag{2.5}$$

where $\tilde{S}(k\ell)$ is a scaling function independent of time and d is the dimension of the system.

In many of the systems, $C_{\rm ag}(t, t_w)$ is also found to exhibit a scaling form [3–5, 7–9, 12, 15, 16]

$$C_{\rm ag}(t, t_w) \equiv \tilde{C}_{\rm ag}(x);\ x = \frac{\ell}{\ell_w}. \tag{2.6}$$

Here ℓ_w is the average size of the domains in the system at time t_w.

For the nonconserved order-parameter, a quantitative theory for scaling behavior was given by Ohta, Jasnow and Kawasaki [10]. This was based on a Gaussian approximation of the auxiliary field concerning the time dependent Ginzburg-Landau (TDGL) equation. From this model a general expression for the correlation function was obtained as [17]

$$C_{\rm OJK}(r; t, t_w) = \frac{2}{\pi} \sin^{-1} \left(\frac{2\sqrt{t t_w}}{t + t_w} \right)^{d/2} \exp \left[\frac{-r^2}{4D(t + t_w)} \right], \tag{2.7}$$

where D is a diffusion constant. For $t = t_w$, this reduces to

$$C(r, t) = \frac{2}{\pi} \sin^{-1} \left[\exp \left(\frac{-r^2}{8Dt} \right) \right], \tag{2.8}$$

which is known as the Ohta-Jasnow-Kawasaki (OJK) function. For $r = 0$ and $t >> t_w$, from Eq. (2.7), one can obtain

$$C_{\rm ag}(t, t_w) \sim \left(\frac{t}{t_w}\right)^{-d/4}, \tag{2.9}$$

or

$$C_{\rm ag}(t, t_w) \sim \left(\frac{\ell}{\ell_w}\right)^{-\lambda}; \ \lambda = \frac{d}{2}. \tag{2.10}$$

Here we have used the fact that $\alpha = 1/2$, say, for the nonconserved Ising model [2, 3, 18]. Liu and Mazenko (LM) [5], using a similar but more general approach, obtained different dimension dependence for λ. The outcome of the dynamical equation for the correlation function, that LM constructed, matches with the OJK theory in the limit $d \to \infty$. Approximate solutions of the above mentioned equation provide [5] $\lambda \simeq 1.29$ and $\simeq 1.67$ in $d = 2$ and 3, respectively.

Two well-known bounds for the exponent λ are due to Fisher and Huse (FH) [4], and Yeung, Rao and Desai (YRD) [7]. FH bound is applicable in the case of nonconserved order-parameter dynamics. This is written as

$$\frac{d}{2} \leq \lambda \leq d. \tag{2.11}$$

Notice here that the lower bound of Eq. (2.11) coincides with the value quoted in Eq. (2.10), outcome of the OJK theory. A more general lower bound, given by YRD [7], incorporates the structural differences between the conserved and nonconserved dynamics, and is defined as

$$\lambda \geqslant \frac{d + \beta}{2}. \tag{2.12}$$

Here β is the exponent related to the power-law behavior of small wave-number (k) for structure factor [19, 20], i.e.,

$$S(k, t) \sim k^{\beta}. \tag{2.13}$$

For nonconserved Ising dynamics the value of β is zero [19, 20]. This leads to the agreement of YRD bound with the FH lower bound in this case.

For the values of λ, the predictions of both OJK and LM agree with the FH bounds. We mention here that there exists an argument, related to percolation, by FH [4], that suggests $\lambda = d - a$, where a is the inverse of the exponent for the power-law singularity of the percolation correlation length. This, e.g., provides $\lambda = 5/4$ in $d = 2$. However, FH [4] cautioned about using this argument, as well as their upper bound.

The results from Monte Carlo (MC) simulations of the nonconserved Ising model in $d = 2$ seem to be consistent [15, 21] with the OJK function of Eq. (2.8), the growth exponent $\alpha = 1/2$ and the FH bounds for λ. The consistency with theory in the λ value appeared true [15, 21] in $d = 3$ as well, for quenches to certain nonzero temperatures (T_f), that lie above the roughening transition [22], from random initial configurations, corresponding to an initial temperature, $T_s = \infty$. But for $T_f = 0$, the $d = 3$ Ising model provided surprises [21, 23–30]. In this case, simulation reports on the time dependence of ℓ differ from the theoretical expectation [18]. While some works reported $\alpha = 1/3$, a few reported even slower growth. In recent works [27, 30], with the simulation of very large systems, it has been shown that the theoretical prediction of $\alpha = 1/2$ can be obtained only at very late time. Furthermore, studies with smaller systems, for $T_f = 0$, revealed interesting freezing behavior with respect to reaching the expected ground state [28, 29]. Unusual structural aspects were reported for $d = 3$ [28, 29, 31, 32]. The scaling form of correlation function was also shown to be different from the case of higher temperatures [21, 33].

Recently, in Refs. [1, 33] the authors had reported that in space dimension $d = 3$, for quenches to $T_f = 0$, the value of λ is $\simeq 1.1$. This is a significant observation in the sense that, unlike for quenches to high temperature, the exponent is much smaller than the FH lower bound. Thus, we have undertaken the task of substantiating this observation by more authentic studies. This is, thus, clearly an extension of a study initiated in Ref. [1]. In this connection, a natural question is: Is this special feature related to the above mentioned freezing phenomena? If yes, does there exist a scaling limit where $C_{\rm ag}(t, t_w)$ decays to zero? In other words, if one chooses larger and larger system size, will $C_{\rm ag}(t, t_w)$ vanish when ℓ/ℓ_w increases indefinitely? If not, the overall problem cannot be placed in the category of standard ever-growing systems, and scaling concepts of nonequilibrium statistical mechanics will lose meaning. Thus, it is essential to know the nature of freezing. For the validity of our analysis and conclusion, existence of a linear relationship between the frozen length scale and system size is essential. If such a relation appears to be true, other question is what affects the value of λ? Is there any interesting structure-dynamics connection? This question was touched upon in Ref. [33]. But more elaborate study of this we find necessary. For this purpose, similar study in $d = 2$ can provide more insight into this.

Here note that freezing has also been reported [28, 29, 31] in $d = 2$. However, in this dimension the character of the growing pattern, unlike in $d = 3$, remains unchanged with the variation of temperature. It is worth examining then, to understand the role

of structure in aging, whether or not there is a "special" value of λ for $T_f = 0$ in $d = 2$. However, one of the latest results [34] for $T_f = 0$, in this dimension also, differs from recent study [15] at high temperature, despite no structural difference. Thus, we revisit the $d = 2$ case, by performing advanced analysis, with high quality data, to check if there really exists a temperature dependence in λ. As mentioned above, outcome of such a study will provide crucial insight. This work addresses this broad issue of structure-dynamics connection and checks for the validity of the decay of autocorrelation to zero in thermodynamic limit by examining the nature of freezing, via state-of-the-art methods of analysis including a novel finite-size scaling (FSS) technique [15, 16, 35–39], the latter itself containing an important feature that is to be discussed later.

Furthermore, even though all the above mentioned studies of kinetic Ising model use (Glauber) spin-flip [35, 40] as trial move during the MC simulations [35], that does not preserve the global order parameter, these moves were accepted with different probabilities in different studies. For example, in Ref. [33], Metropolis algorithm [35] was used, whereas Refs. [28] and [29] used the Glauber algorithm [35, 40]. Thus, it is also important to establish that the results obtained via different algorithms do agree with each other, particularly when unexpected observations have been reported on various coarsening aspects for $T_f = 0$. Here we state that at $T_f = 0$ the trial moves that bring no change in the energy are customarily accepted with the probabilities $p = 0$, $1/2$ or 1, the latter two correspond, respectively, to the Glauber and Metropolis methods. Such an exercise we feel necessary particularly because of the fact that for $p = 0$ coarsening is not observed. This was reported [28, 29] previously and was also independently verified by us. In addition, to address the controversy on the growth exponent in $d = 3$, we performed simulations with very large systems.

For the decay of $C_{\rm ag}(t, t_w)$, our conclusions are the following. Our results strongly suggest that there exists no temperature dependence in pattern, growth and aging in the case of $d = 2$. On the other hand, for $d = 3$, the value of the aging exponent appears smaller than the FH lower bound. Outcomes from $d = 2$ and 3 suggest that the low value of λ in $d = 3$ is due to the formation of different structure at $T_f = 0$ than high temperatures which nicely comply with the construction of the YRD bound.

On the issue of freezing, the frozen length scale as well as the onset of finite-size effects are system-size dependent with a linear relationship. This fact validates our scaling analysis, implying that the obtained results are meaningful in the thermodynamically large system size limit. Furthermore, for the domain growth, unambiguous confirmation of the $t^{1/2}$ behavior has been provided. Overall coarsening picture obtained by using

Metropolis and Glauber algorithms are found to be consistent with each other, as far as $t \to \infty$ limit is concerned. Nevertheless, we caution the reader on choosing low value of p. For such choices the amplitude of growth can be smaller and transient can be longer. Thus, to observe the expected asymptotic behavior one requires much longer simulation runs.

The rest of the chapter is organized as follows. Section 2.2 contains the discussion on the model and methods, followed by the results in Section 2.3. The conclusions are given in Section 2.4. Appendix contains a discussion on the finite-size scaling method.

2.2 Model and Methods

Nonconserved coarsening dynamics in the nearest neighbor Ising model, for $T_f = 0$, is studied via MC simulations [35] on a square or simple cubic lattice. The Hamiltonian of the model is given by

$$H = -J \sum_{\langle ij \rangle} S_i S_j, \;\; S_i = \pm 1, \;\; J > 0, \tag{2.14}$$

where $\langle ij \rangle$ stands for the nearest neighbors. The values of T_c for this model [35] are $= 2.269185...J/k_B$ and $\simeq 4.51 J/k_B$, in $d = 2$ and 3, respectively, k_B being the Boltzmann constant. As opposed to the $d = 2$ case, in $d = 3$ the value is only approximate.

The simulations are performed by using Glauber spin-flip dynamics [40] where a trial move is equivalent to selecting a spin randomly and changing the sign of it. During this trial move, if the energy change, $\Delta E < 0$, the move is always accepted and if $\Delta E > 0$, the move is rejected. For the case $\Delta E = 0$, different probabilities p (> 0) can be used for accepting the moves [28, 29]. In this work, we have used $p = 0.5$ and 1, that correspond to Glauber [35, 40] and Metropolis [35] acceptance probabilities, respectively. Such L^d trial moves correspond to one MC step (MCS), which is the unit of time in our simulations. Here L is the linear dimension of a system, in units of a, the lattice constant. In all our simulations, we set k_B, J and a to unity.

The average domain length, $\ell(t)$, was obtained from the first moment of the distribution function, $P(\ell_d, t)$, i.e. [21],

$$\ell(t) = \int d\ell_d \ell_d P(\ell_d, t). \tag{2.15}$$

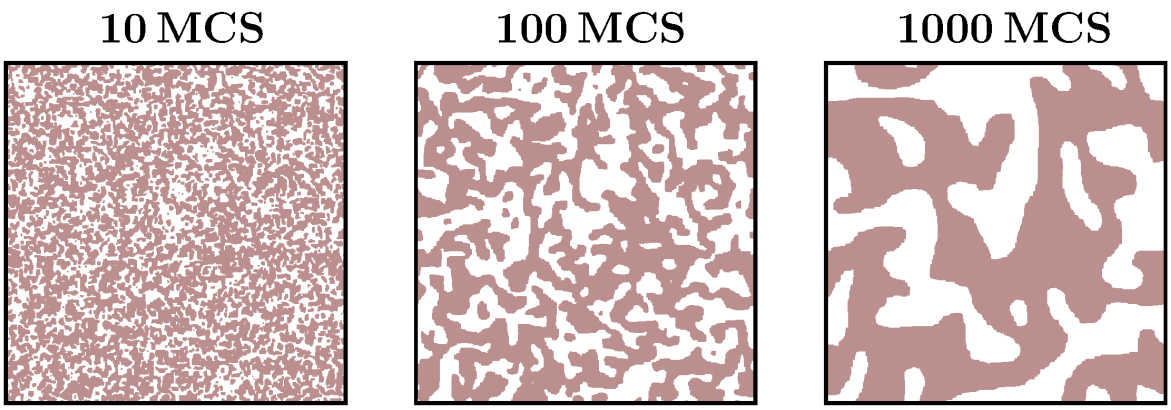

Figure 2.1: Evolution snapshots from the Monte Carlo simulations of the 2D nonconserved Ising model at $T_f = 0$, after quenching from $T_s = \infty$. These pictures correspond to $p = 1/2$. The marked regions represent "up" spins and the locations of the "down" spins are left unmarked. The linear dimension of the system is $L = 512$.

Here ℓ_d is obtained by scanning a system along different Cartesian directions; it is the distance between two successive interfaces. The length scale can be calculated from other methods also [41], e.g., from the decay of $C(r, t)$. Results from various methods should differ only by a proportionality constant.

All our presented results are averaged over multiple independent initial configurations. This number, for growth and aging, falls in the range between five and 60, depending upon the value of L. Other than the finite-size effects and freezing phenomena related analyses, all data for the correlation functions are for $L = 512$, presented after averaging over 100 and 20 independent initial configurations, in $d = 2$ and $d = 3$, respectively. For the freezing phenomena, given that the studied systems are rather small, we have obtained the quantitative results after averaging over several hundred initial configurations.

In the related work of Ref. [1] all results were obtained for $p = 1$. If any resemblance appears in figures with those in Ref. [1], differences are there either in the value of p or in statistics (with new runs) or lengths of simulation runs or in space dimension or in system size. For the sake of completeness and better understanding we have presented an elaborate story.

2.3 Results

We start our discussion by presenting results for the pattern and growth. In Fig. 2.1 we show snapshots taken during the evolution of the nonconserved Ising model at $T_f = 0$.

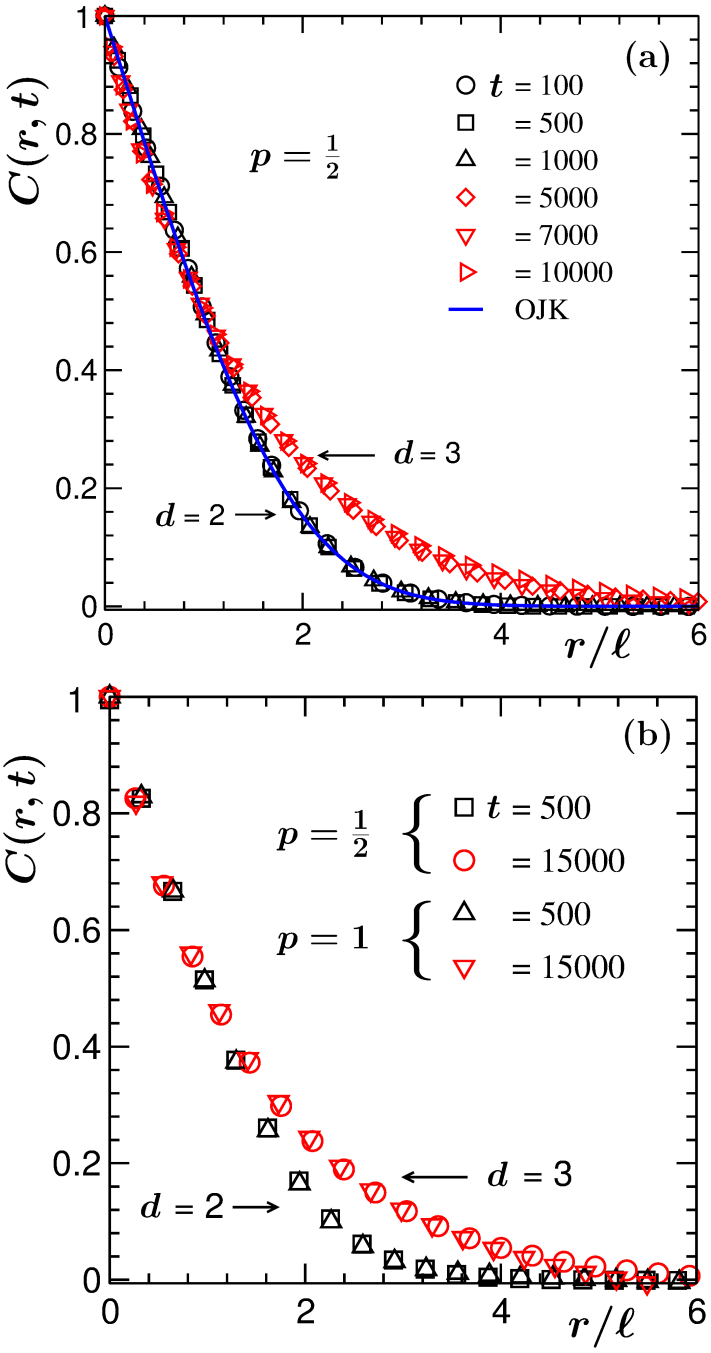

Figure 2.2: (a) Scaling plots of the two-point equal-time correlation function. We have shown $C(r,t)$ as a function of r/ℓ, for both $d = 2$ and 3. In each dimension data from three different times are included. The used values of ℓ in this figure were obtained from $C(\ell,t) = 0.5$. For all the other purposes we have used ℓ obtained from the first moment of the domain size distribution function $P(\ell_d,t)$. The continuous curve there is the Ohta-Jasnow-Kawasaki function. All results are for $p = 1/2$. (b) Same as (a) but here we show comparison between outcomes from $p = 1$ and $1/2$.

These snapshots are from MC simulations in $d = 2$, with $p = 1/2$. Growth in the system is clearly visible. To check for the self-similarity, in Fig. 2.2(a) we show scaling plots of the two-point equal-time correlation function. In this figure, we present data from both $d = 2$ and 3, with $p = 1/2$. Here the data from different times collapse on top of each other implying the self-similar character [2, 3] of the growth. Interestingly, the master curves from $d = 2$ and $d = 3$ do not match with each other [21]. It can also be seen that the $d = 2$ data are in agreement with the OJK function [10, 21]. We note here, $C(r, t)$ at high temperatures, for both the dimensions, agree well with the OJK form [21]. This states the fact that the pattern at $T_f = 0$, in $d = 3$, is special. This is in line with previous reports by other authors [21, 23–30, 33] and will be useful in explaining new observation with respect to aging property. Fig. 2.2(b) contains $C(r, t)$ data from both the dimensions, for $p = 1/2$ as well as for $p = 1$. It appears that the results for $p = 1/2$ nicely overlap with those for $p = 1$ when the distance axis is appropriately scaled by the corresponding average domain sizes. These results confirm that both the algorithms provide similar structure.

In Fig. 2.3(a) we present data for domain growth, viz., we show $\ell(t)$ versus t for $p = 1$, on a log-log scale. Results from both the dimensions are included. The 2D data exhibit a unique power-law behavior, with $\alpha \simeq 1/2$, over an extended period of time. The departure from the above scaling in the long time limit, clearly seen for $L = 512$ (shown with symbols), is due to the finite-size effects. While this behavior in $d = 2$ is same as the results from nonzero temperature, the case of $d = 3$ is very different from our observation for coarsening at T_f higher than the roughening transition [22] (here note that in $d = 2$ there does not exist a nonzero roughening transition). The 3D data in Fig. 2.3(a), after a brief initial period (with higher exponent corresponding to annihilation of local defects), display [8, 21, 23–26] growth with $\alpha \simeq 1/3$ over more than two decades in time. At very late time the data exhibit a crossover [21, 27, 30] to $\alpha \simeq 1/2$. Towards the end of the presented time window, we see signature of finite-size effects for $L = 512$ (see the data set with symbols).

With respect to the appearance of finite-size effects, however, there is similarity between the 2D and 3D cases. See the deviation of data with symbols, corresponding to $L = 512$ for both the dimensions, at $\ell \simeq 205\,(= 0.4L)$, marked by the dashed horizontal line. For larger system size (see the dashed line for $d = 3$ with $L = 750$ and the dashed-dotted line for $d = 2$ with $L = 2048$), of course, the growth with $\alpha = 1/2$ is more prominent due to lesser effects of finite system size over the presented time range. Note that such a clear confirmation of $t^{1/2}$ behavior for extended period of time in

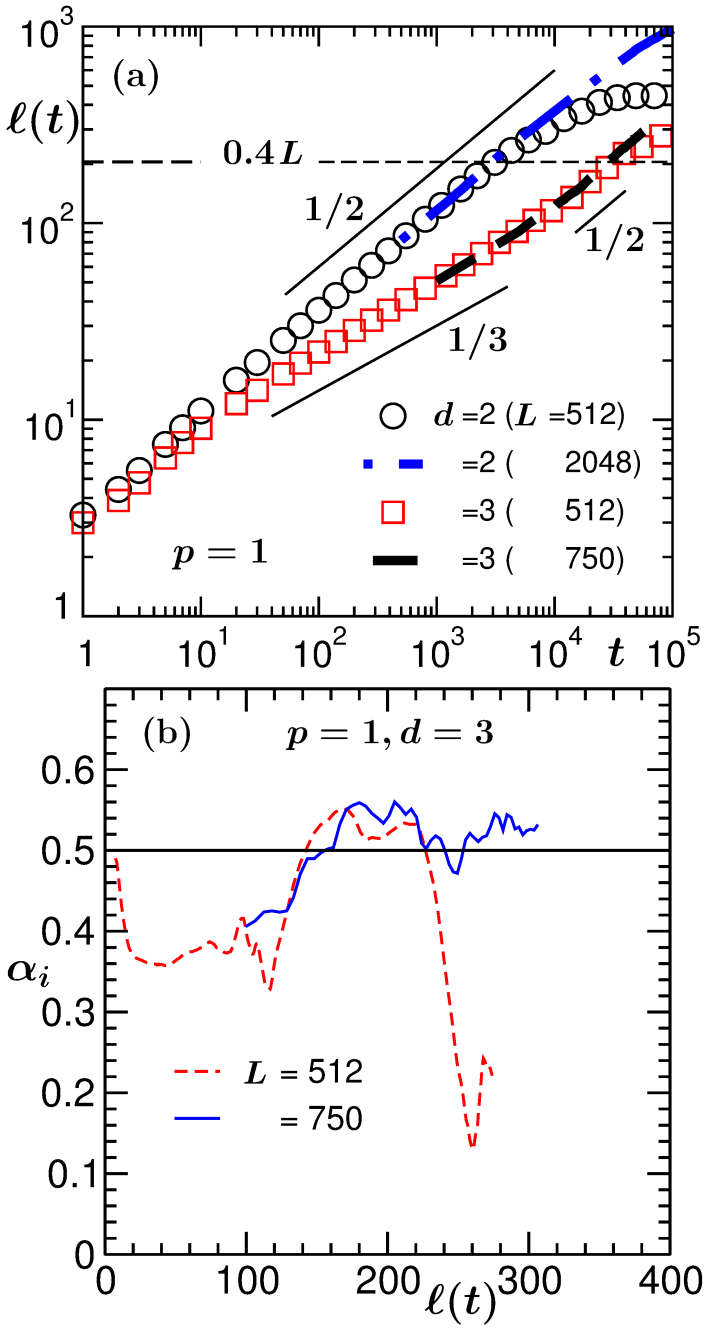

Figure 2.3: (a) Log-log plots of average domain size versus time, for $p = 1$. We have shown data from both the dimensions. The continuous lines represent various power laws, exponents for which are mentioned in the figure. The dashed horizontal line, at $\ell = 0.4L$, marks the appearance of finite-size effects for data sets corresponding to $L = 512$. This figure partially resembles Fig. 5.1 of Ref. [1]. (b) Instantaneous exponent $\alpha_i \left(= \frac{d \ln \ell}{d \ln t}\right)$ is plotted versus ℓ for $d = 3$.

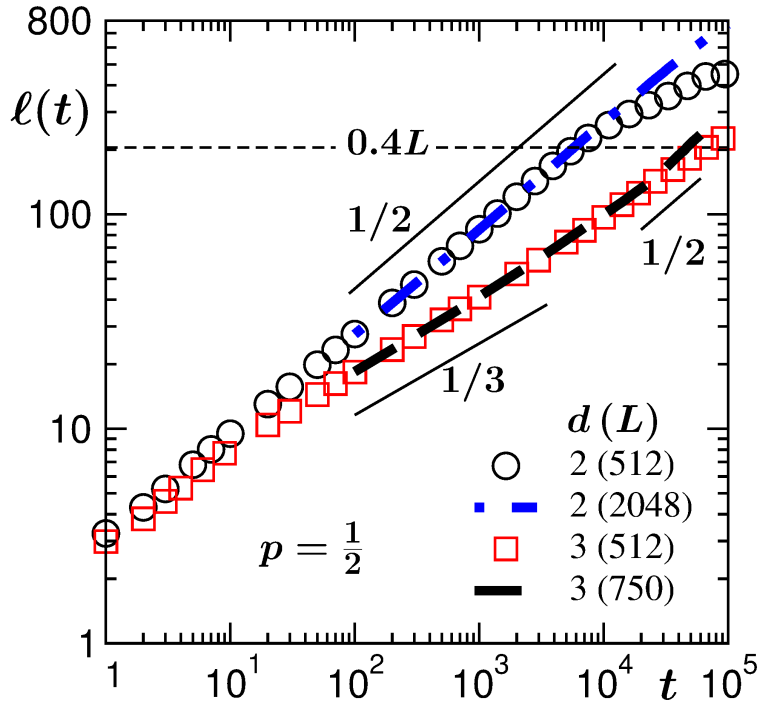

Figure 2.4: Log-log plot of average domain length versus time. We have shown data from $d = 2$ and 3. The continuous lines represent power-laws, exponents being mentioned next to them. The dashed horizontal line marks the appearance of finite-size effects, at $\ell = 0.4L$, for $L = 512$. The presented data are with $p = 1/2$.

$d = 3$ could not have been previously possible because of consideration of much smaller system sizes. This point is further justified by presenting the instantaneous exponent [42] $\alpha_i \left(= \frac{d \ln \ell}{d \ln t}\right)$ as a function of ℓ in Fig. 2.3(b). For $L = 750$, the length scale "range" that follows $t^{1/2}$ behavior is a factor of 2 larger than that for $L = 512$, the size that was previously considered. If the brief "$\alpha_i \simeq 1/2$" period in the $L = 512$ case is argued to be a statistical fluctuation, the stable data set for $L = 750$ certainly removes this confusion that actually is an artefact of finite-size effects in the smaller system size data. Since we are now confident that growth remains unaffected even for quench to very low temperature, in both the dimensions, any temperature related anomaly in the aging property may safely be attributed to the structural aspect. The appearance of finite-size effects at $\ell \simeq 0.4L$ at $T_f = 0$ is very similar to that for non-zero values of T_f. We mention here, in the 3D case the very late time finite-size behavior for $T_f = 0$ is rather complex [28, 29]. The systems almost never reach the ground state (this problem is perhaps less severe in $d = 2$) even at the end of extremely long simulation runs [28, 29, 43, 44]. One may anticipate this fact to be somewhat more severe for $p < 1$.

Fig. 2.4 shows log-log plots of ℓ versus t, for both the dimensions, for the $p = 1/2$ case. Like in the $p = 1$ case, the 2D data appear consistent with the theoretical expectation all the way till the finite-size effects appear [21] at $\ell \simeq 0.4L$. For $L = 512$, see the departure of the data set from that of $L = 2048$. Plot for the $d = 3$ case also exhibits a trend similar to the $p = 1$ case – there exists a consistency of the data set with an exponent $\alpha \simeq 1/3$ for nearly three decades in time, after which a crossover appears. This is very clearly visible in the $L = 750$ case. By examining the $L = 512$ data one may conclude that the finite-size effects appear a little earlier than when ℓ reaches $0.4L$. This could well be due to statistical reasons. Here note that, as already mentioned above, runs for many initial configurations get trapped in metastable states very early, without allowing us to appropriately probe the post-crossover region.

Data presented in Fig. 2.4 [as well as in Fig. 2.3(a)] are averaged by including such runs as well. In Fig. 2.5(a) we show ℓ versus t data for two typical runs, on linear scale, for $L = 512$. It is clear that some runs can encounter freezing around the time (or even before) when a crossover is expected. This necessitates either extremely good statistics or very large system size. In part (b) of this figure, we show the plot for the data set that did not show a signature of freezing, on a log-log scale. Clearly, a $t^{1/2}$ behavior is very prominent towards the end. This overall picture is true for both values of p. We will provide further discussion on freezing phenomena towards the end.

From the growth data for $d = 2$ and 3, obtained by setting p to $1/2$ and 1, we make the following further observations. In both the dimensions growth amplitude is smaller for lower value of p. In fact, if carefully examined, data in Fig. 2.3(a) and Fig. 2.4 suggest that for $d = 3$ the preasymptotic growth occurs with a smaller exponent for lower value of p. On the other hand, the length scale at the onset of $t^{1/2}$ behavior remains unchanged. This implies that, to observe the theoretically expected value of α in the higher dimension one needs to run a large system for a longer period of time, which is a computationally difficult task. Here one may ask, can the overall slower growth for smaller p affect the value of λ? Answer to that question is not obvious to us.

From the demonstration in Fig. 2.5 one may ask: why not analyze the data sets that do not freeze? For large enough systems, simulation of which is a necessity here, it is difficult to choose which systems will finally exhibit freezing and which ones not. Furthermore, as we will discuss in detail later, in connection with studies via smaller systems, practically no system reaches the ground state in $d = 3$. Thus we prefer to work with averaging over all initial realizations and rely on certain scaling rules that will

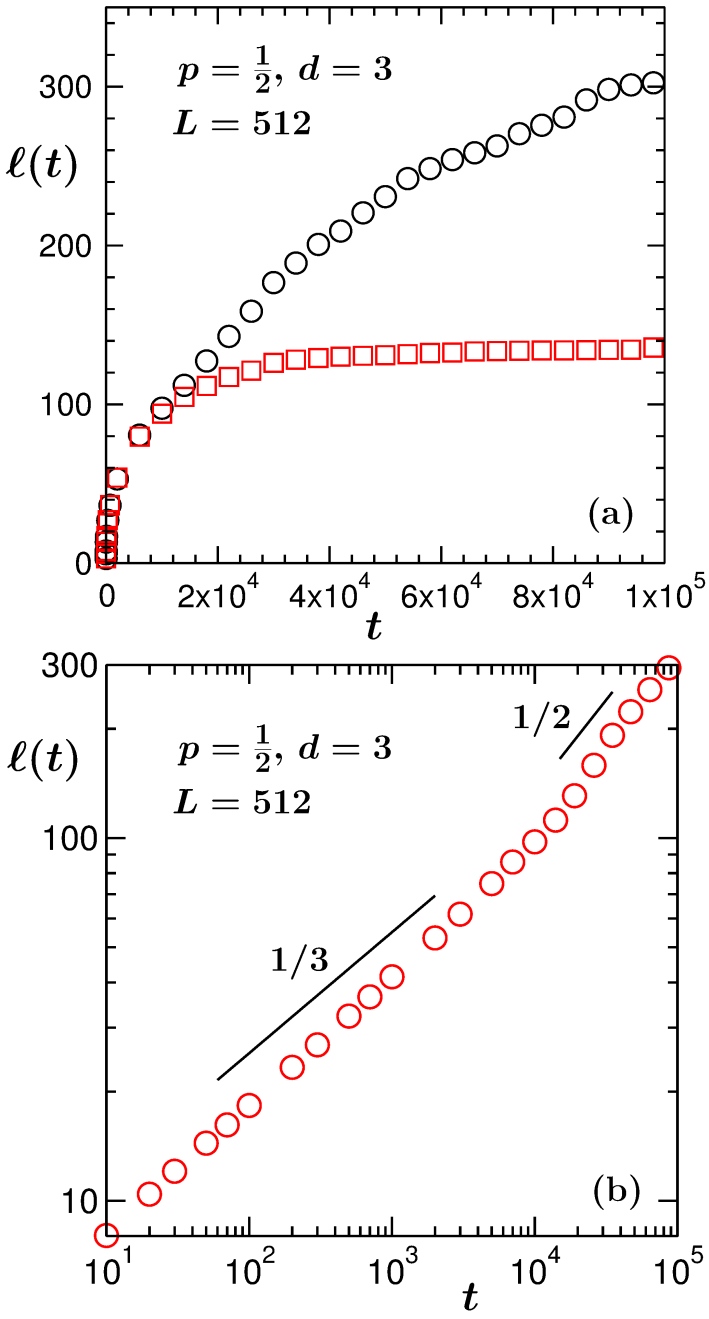

Figure 2.5: (a) Plot of domain length versus time in $d = 3$, for two different initial configurations, from systems with $L = 512$. (b) Log-log plot of average domain size versus time for the data sets that did not undergo freezing. These results are obtained with $p = 1/2$.

be discussed later. Now we move to the aging property of the system. We will present the aging results for $p = 1/2$. For FSS analysis we will include data for $p = 1$ as well.

In Figs. 2.6(a) and (b) we have plotted the autocorrelation function, $C_{\rm ag}(t, t_w)$, versus ℓ/ℓ_w, in $d = 2$ and $d = 3$, respectively. A nice collapse of data from different t_w values are obtained in both the dimensions. For large x values deviations are present in all the data sets, which perhaps are related to finite-size effects [15, 16]. For higher t_w values the deviations occur earlier. Note here that for a higher value of t_w smaller fraction of the system size is available for further growth. For $d = 3$, the presented data did not suffer as much from the finite-size effects. In this dimension running simulations for large systems over very long period, to observe such effects, is computationally very demanding. Note that the appearance of finite-size effects, if deviations from the scaling really imply the fact, in the autocorrelation function, in both the dimensions, again complies with our above quoted limit $\ell \simeq 0.4L$ that we observe for the domain growth. The solid lines in these figures correspond to the power-laws with the exponents given by LM predictions of λ. In the case of $d = 2$, the data are consistent with this, but for $d = 3$, the discrepancy between the data and LM value is clearly visible [see Fig. 2.6(b)]. Furthermore, the scaling functions obtained from the simulation shows continuous bending [15]. This, of course, is possible when there exist corrections to the power-law scaling [15]. In such a situation, calculation of the instantaneous exponent [5, 15, 16, 42, 45] gives useful information. This can be defined as,

$$\lambda_i = -\frac{d \ln C_{\rm ag}}{d \ln x}. \tag{2.16}$$

We plot λ_i versus $1/x$ (recall, $x = \ell/\ell_w$), for the $d = 2$ case, in Fig. 2.7(a), from two different system sizes. The value t_w is fixed here. Data for the smaller value of L deviate from a linear behavior, as x increases, when the value of x is approximately 2. This is due to the finite-size effects and can be confirmed from the continued linear trend for the data set from the larger value of L. Results for different values of t_w, for fixed L, provide similar information. This is, as stated above, because of lesser effective system size available for larger t_w.

A linear extrapolation to $x = \infty$, using data unaffected by finite-size effects, provides a value of λ close to 1.3. Invoking the linear behavior,

$$\lambda_i = \lambda - B/x, \tag{2.17}$$

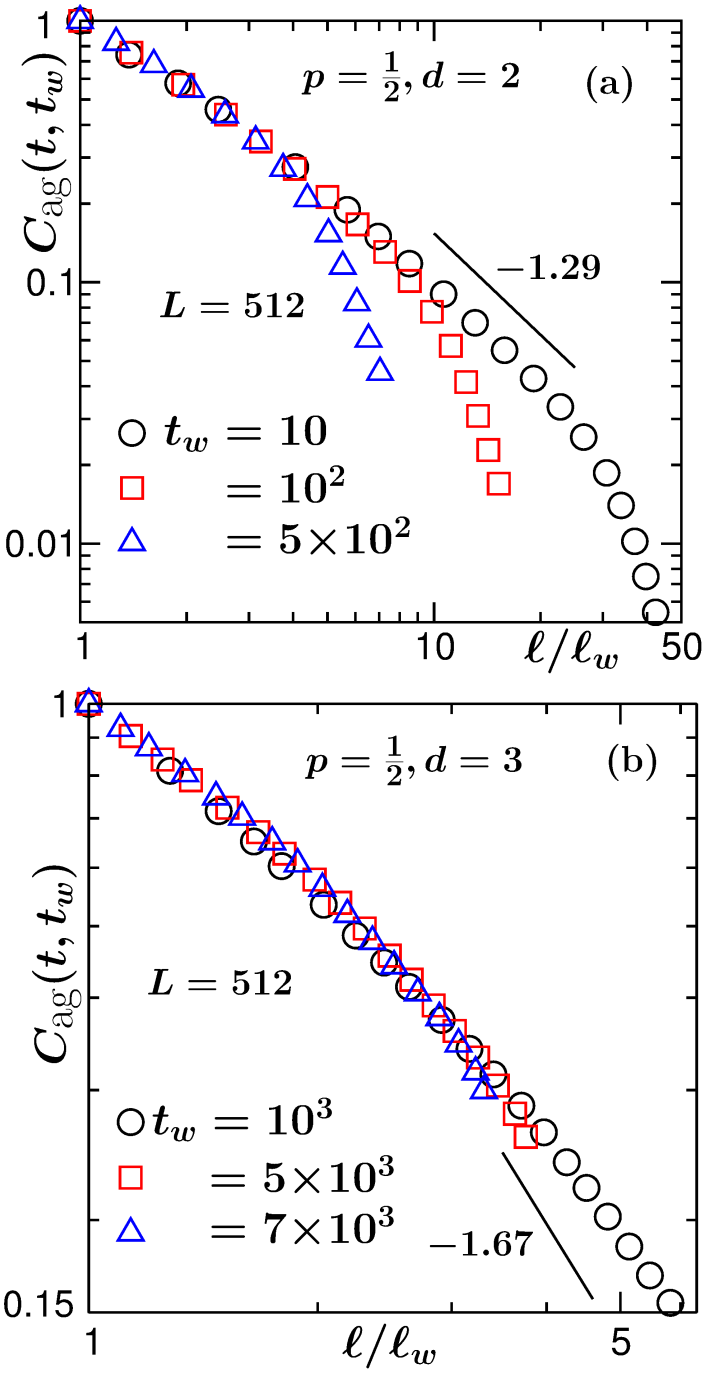

Figure 2.6: (a) The plots of the autocorrelation function, $C_{\rm ag}(t, t_w)$, versus ℓ/ℓ_w, from three different t_w values for $d = 2$, in log-log scale. The solid line represents a power-law decay with exponent given by LM (= 1.29) [5]. (b) Same as (a), but here the results are from $d = 3$. The solid line here has the power-law exponent $\lambda = 1.67$. All the results correspond to $p = 1/2$.

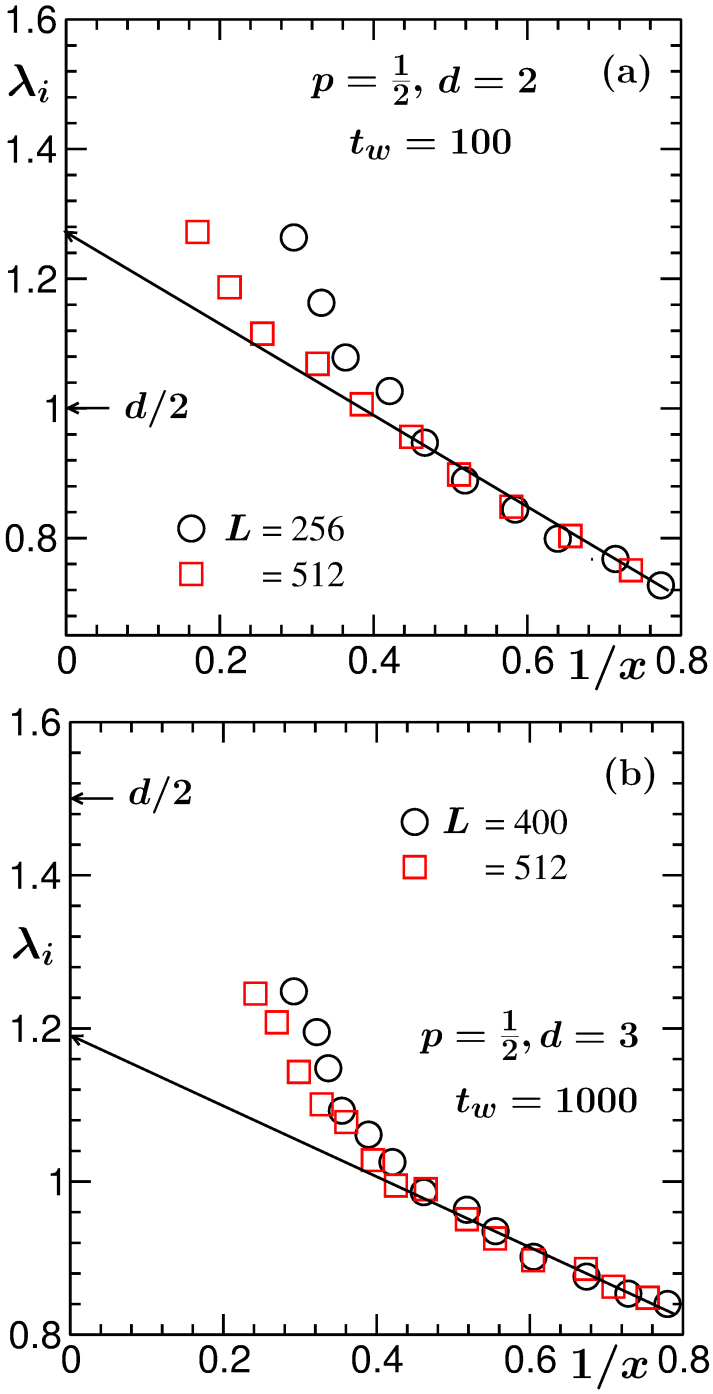

Figure 2.7: (a) Plots of instantaneous exponent, λ_i, versus $1/x$ $(= \ell_w/\ell)$, from two different system sizes for the case $d = 2$. We have fixed the value of t_w at 100. The solid line is a guide to the eye. (b) Same as (a), but the results here are from $d = 3$, and t_w is fixed at 1000. In both the figures the FH lower bounds have been marked by $d/2$. All the results were obtained by fixing p to 1/2.

in the definition in Eq. (2.16), one obtains the full form of the scaling function [15, 16], i.e.,

$$C_{\rm ag}(t, t_w) = Ae^{-B/x}x^{-\lambda}, \tag{2.18}$$

where A and B are constants.

This implies, a power law can be realized only in the $t >> t_w$ limit. Like in the critical phenomena here also it is natural to expect that the corrections should be described by power-laws. However, separately estimating exponents for corrections of different orders is a difficult task. Given the trend of the data sets, the exponential factor appears to describe the corrections reasonably well. We will make further comment on the accuracy of this full form later.

In Fig. 2.7(b), we present the results for $d = 3$. A linear extrapolation provides a value of λ close to 1.2 here. Recall that the LM prediction for λ in $d = 3$ was $\simeq 1.67$. So, in this case there exists discrepancy between the simulation results and LM prediction. Furthermore, $\lambda \simeq 1.2$ violates the FH lower bound as well. Note that for $d = 2$ in all temperatures [15, 33], including the one discussed here, and for $d = 3$, for higher temperatures, above the roughening transition [15], the value of λ obtained from the simulation studies are in good agreement with the LM prediction, and are well within the FH bound.

A finite-size scaling analysis can provide more accurate exponents [15, 16], given that the data for λ_i, at large x, may suffer from finite-size effects, preventing unambiguous choice of regions for performing a (linear) fit. Further, this will bring confidence in the empirical form of $C_{\rm ag}(t, t_w)$, given in Eq. (2.18). In addition, this will confirm our speculation on finite-size effects.

In a finite-size scaling method, one introduces a scaling function, Y, which is independent of the system size [15, 16, 35–37, 46]. To make Y independent of system size, one needs to appropriately choose a dimensionless scaling variable y. For the present problem

$$Y = C_{\rm ag}(t, t_w)e^{By/y_w}y_w^{\lambda}, \tag{2.19}$$

with

$$y = \frac{L}{\ell}. \tag{2.20}$$

See Appendix for details.

In Fig. 2.8, we present the results from the finite-size scaling analysis for $d = 2$ in (a) and for $d = 3$ in (b). These results are for $p = 1/2$. In the case of $d = 2$, very good collapse of data, along with consistency with the limiting behavior [see Eq. (A.2) in

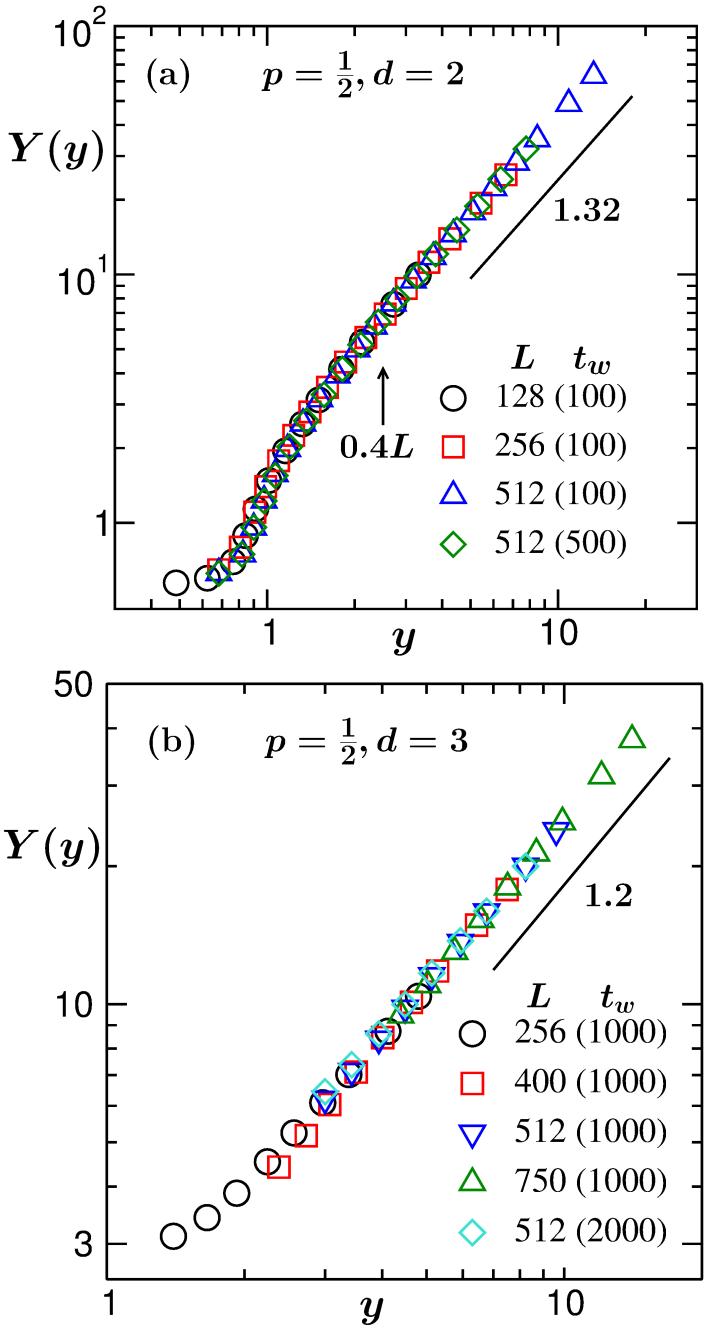

Figure 2.8: (a) The plot for the finite-size scaling analysis of $C_{\rm ag}(t, t_w)$ in $d = 2$. The vertical arrow marks the departure of the scaling function from the y^λ behavior. (b) Same as (a), but here it is for $d = 3$. The solid lines represent power-laws with the values of exponent mentioned next to them. All results are for $p = 1/2$.

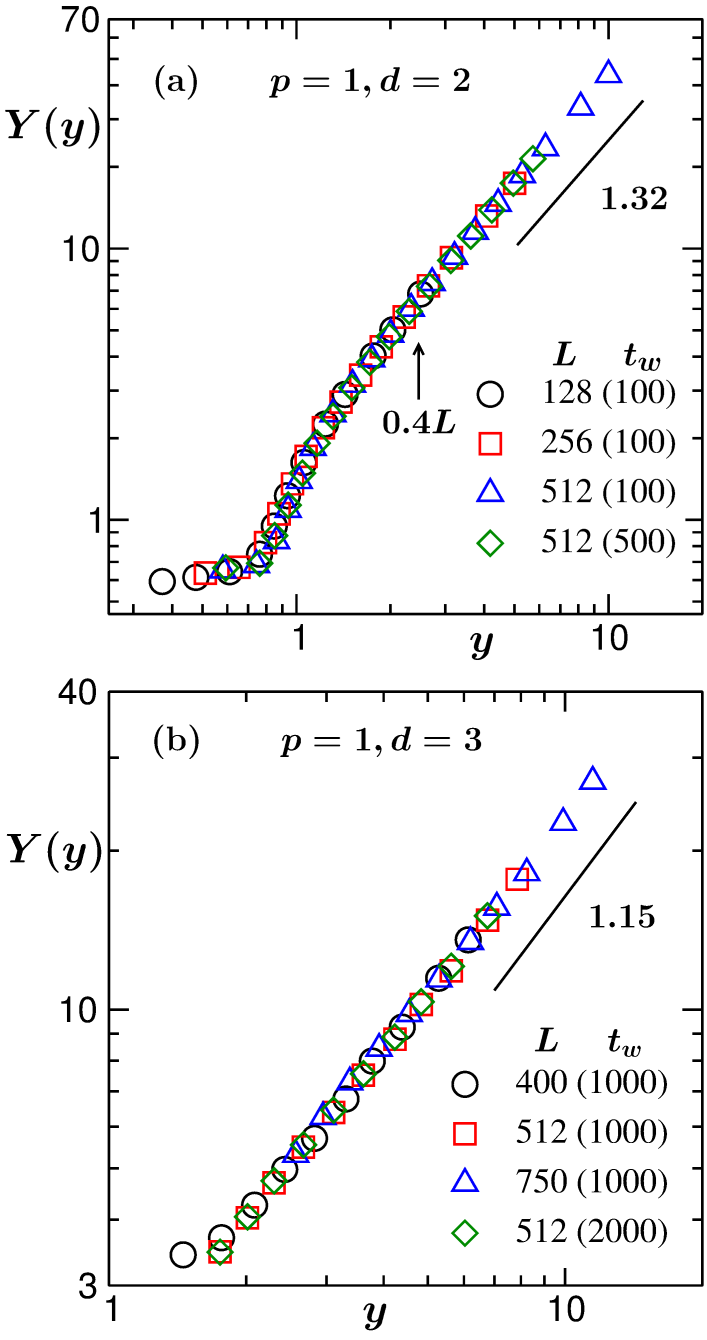

Figure 2.9: Same as Fig. 2.8 but here it is for $p = 1$.

Appendix], is obtained for $\lambda = 1.32$ and $B = 0.80$. This value, within statistical error, is consistent with the LM prediction, and also with a previous study [15] for $T_f = 0.6T_c$. In the large y limit the data are consistent with the power-law amplitude $A \simeq 2$. This can be appreciated by considering $C_{\rm ag}(t, t_w) = 1$ at $x = 1$ and $B = 0.8$. The departure from the power-law behavior is marked by a vertical arrow in Fig. 2.8(a). This corresponds to $\ell = 0.4L$ where finite-size effects occur. A robust power law behavior for Y till the finite-size effects appear, irrespective of the system size, provide confidence in the exponential correction factor. In this connection, also note that for $L = 512$ and $t_w = 100$, the power-law behavior extends over $t - t_w$ ranging between 0 and approximately 6000. One may think of improving accuracy in the estimation of λ by allowing for an adjustable exponent in Eq. (2.17), by replacing x by x^γ. This exponent will, of course, appear in the argument of the exponential correction factor. We have checked that best collapse appears for $\gamma \simeq 1$ and $\lambda \simeq 1.32$. Nevertheless, we caution here that the scaling analysis may be less reliable when there are large number of adjustable parameters.

In the case of $d = 3$ the value of exponent λ, from such analysis with $\gamma = 1$, turns out to be 1.2, which is very different from that at $0.6T_c$ [15], and also far below the FH lower bound. This is consistent with the results from instantaneous exponent analysis. Now our aim is to check whether the true violation of lower bound is occurring or not. This can perhaps be understood from the derivation of YRD which we will discuss shortly. In Fig. 2.8, before exhibiting a nearly flat behavior the 2D data fall rather sharply, compared to the 3D case. This may be related to the more prominent freezing phenomena in the latter dimension. This fact, as promised, we will discuss later.

The FSS results for $p = 1$ are shown in Fig. 2.9. Here also we obtain excellent collapse of data in both the dimensions. The presented results correspond to $\lambda = 1.32$ in $d = 2$ and 1.15 in $d = 3$. These numbers are consistent with those for $p = 1/2$. In both the figures, viz., Fig. 2.8 and Fig. 2.9, we have shown that data collapse can be obtained by considering different values of t_w. This is an important feature and is explained in the Appendix.

Using the structure factors at t_w and t, YRD arrived at

$$C_{\rm ag} \leq \ell^{d/2} \int_0^{2\pi/\ell} dk k^{d-1} [S(k, t_w) \tilde{S}(k\ell)]^{1/2}, \tag{2.21}$$

in which they substituted the small k behavior of $S(k, t_w)$ [cf. Eq. (2.13)], to obtain the lower bound. A plot of $S(k, t_w)$ versus k on a log-log scale is shown in Fig. 2.10 for $t_w = 0$ and 2000 from $d = 3$, the latter belonging to the scaling regime of $C_{\rm ag}(t, t_w)$,

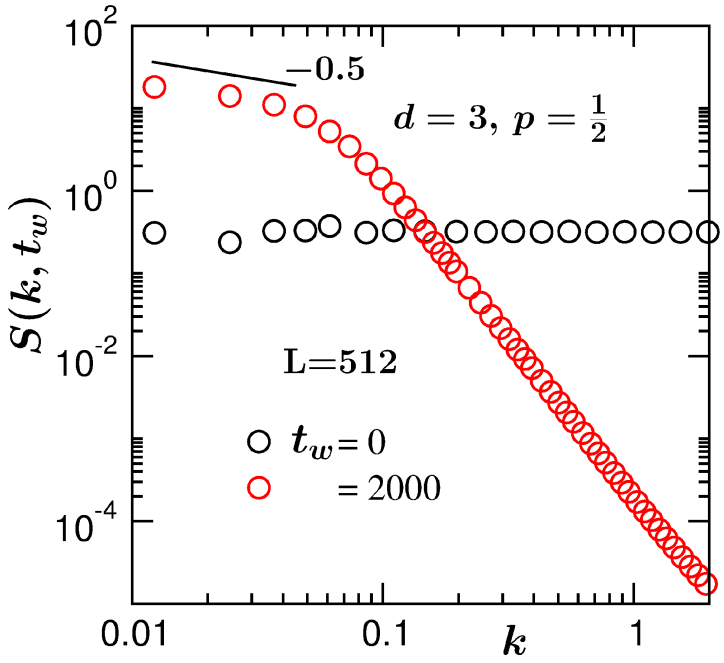

Figure 2.10: Plots of structure factor, $S(k, t_w)$, versus k, in $d = 3$, for two different t_w values. The solid line is a power-law for which exponent is mentioned in the figure. The results are for $p = 1/2$.

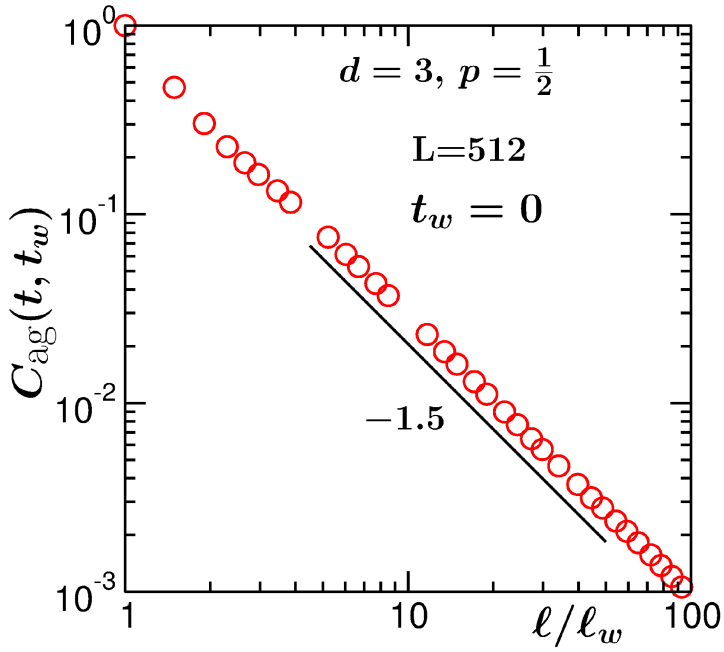

Figure 2.11: Log-log plot of the autocorrelation function, $C_{\rm ag}(t, t_w)$, versus ℓ/ℓ_w, for $t_w = 0$ in $d = 3$. The solid line represents the power-law decay with an exponent which is mentioned in the figure. The data are for $p = 1/2$.

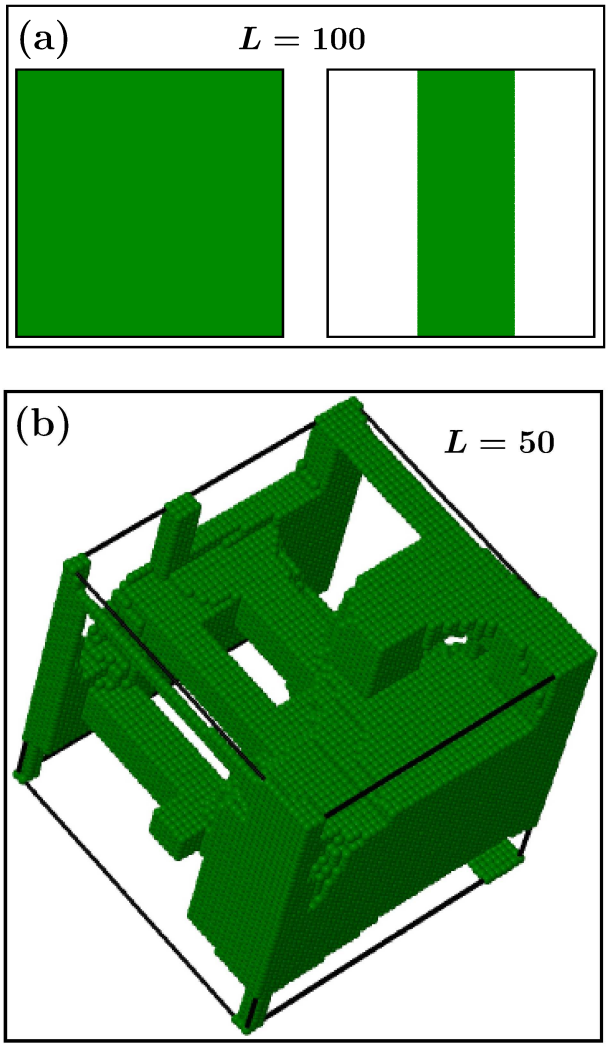

Figure 2.12: Typical representative final snapshots from (a) $d = 2$ and (b) $d = 3$. These snapshots were obtained by using $p = 1/2$.

for $p = 1/2$. The data from later waiting time are consistent with $\beta \simeq -0.5$ and thus, within numerical error, our quoted value of λ is in reasonable agreement with the YRD number. On the other hand, for $t_w = 0$ we expect a flat curve for $S(k, t_w)$, implying $\beta = 0$, which indeed is the case. Thus, for $t_w = 0$ the exponent λ should satisfy the FH lower bound. Furthermore, since the $S(k, t_w = 0)$ plot is completely flat, by taking lesson from Eq. (2.21) one may expect a "pure" power-law behavior of $C_{\rm ag}(t, t_w)$ for $t_w = 0$. In Fig. 2.11 we present a log-log plot of $C_{\rm ag}(t, t_w)$ versus x for $t_w = 0$ that matches this expectation, confirming the structure-dynamics-connection further. Here we mention that a $\beta = 0$ behavior in $S(k, t)$ may be realized in the scaling regime of $C_{\rm ag}(t, t_w)$ also. But to realize that, as well as if λ, in that case, crosses over to a higher

value, one needs to simulate systems 10 times larger than considered here, for extremely long time.

Nice collapse of data in the FSS analysis of $C_{\rm ag}$, along with the growth data, is suggestive of the fact that the length scales at the onset of finite-size effects vary linearly with L, which is one of the requirements for the validity of the analysis. Nevertheless, in view of the reported freezing phenomena it is important to directly check the relationship of the corresponding length scale with L. In case of a deviation, conclusions drawn so far will become invalid in the thermodynamic limit.

Typically, in many real physical situations, the final (frozen) length scale, ℓ_f, does not depend upon the system size [47–50]. In many systems the value of ℓ_f is set by a distance related to the repulsive barrier in the interacting potential [47–49]. Such a picture related to barrier, however, is not expected in the current situation. Nevertheless, to rule out that none of the presented results are affected by this freezing phenomena, we need to know if there exists any system-size dependence of ℓ_f.

In Fig. 2.12(a) we show final configurations from two different initial random compositions in $d = 2$. The one on the left corresponds to the ground state and the other represents a frozen state. In Fig. 2.12(b) we show a frozen configuration from $d = 3$. For both $d = 2$ and 3, the presented configurations are obtained by using $p = 1/2$. As opposed to the right frame in $d = 2$, where it is easily identifiable that no further growth can occur, the $d = 3$ structure is more complex. The 3D snapshot contains the step-like structures with spins that do not change the energy during the flips in the MC simulations. These are referred to as 'blinker spins', which are responsible for the frozen states in the system. Details on this can be found in Refs. [28, 29, 33, 51].

We observe that for a particular system size, for different initial configurations, ℓ_f varies significantly in $d = 3$, almost never reaching L [28, 29]. Whereas in $d = 2$, the frozen states are related to the stripe structure [32] seen in Fig. 2.12(a). Distributions of ℓ_f, $P(\ell_f)$, for both $p = 1/2$ and 1, obtained from such variation, are shown in Fig. 2.13(a), for $d = 2$, $L = 200$; and in Fig. 2.13(b), for $d = 3$, $L = 70$. The average values, $\langle \ell_f \rangle$, that can be extracted from these distributions turn out to be approximately same for $p = 1$ and $p = 1/2$. The observation is similar for other values of L. In the case of $d = 3$ we observe a single peak, with reasonably large width, whereas there exist two spikes in $d = 2$. These spikes are related to the ground and stripe states (we have ignored the diagonal stripes). From the height of the two peaks, it can be appreciated that the ground state is reached approximately twice as often as the stripe states [51]. This fact

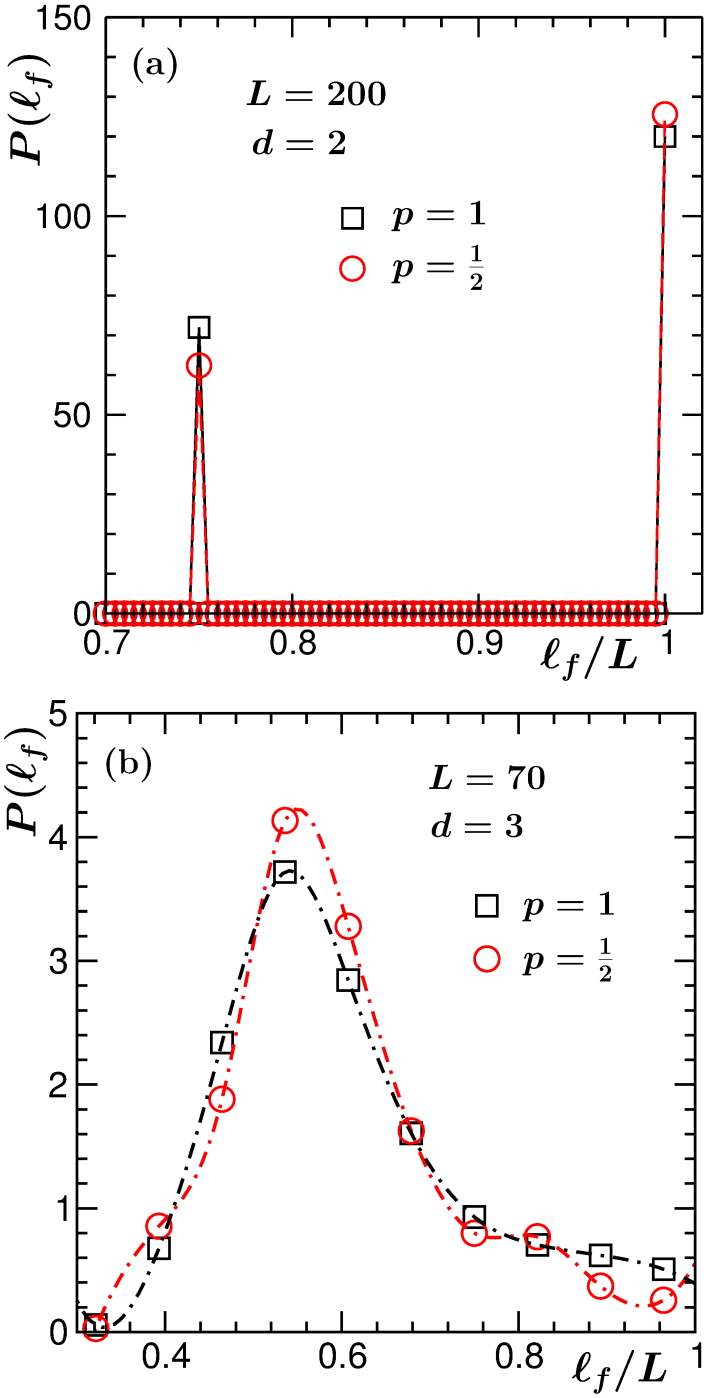

Figure 2.13: Plots of the distribution of final length, ℓ_f, versus the scaled length ℓ_f/L, for (a) $d = 2$, $L = 200$; (b) $d = 3$ and $L = 70$.

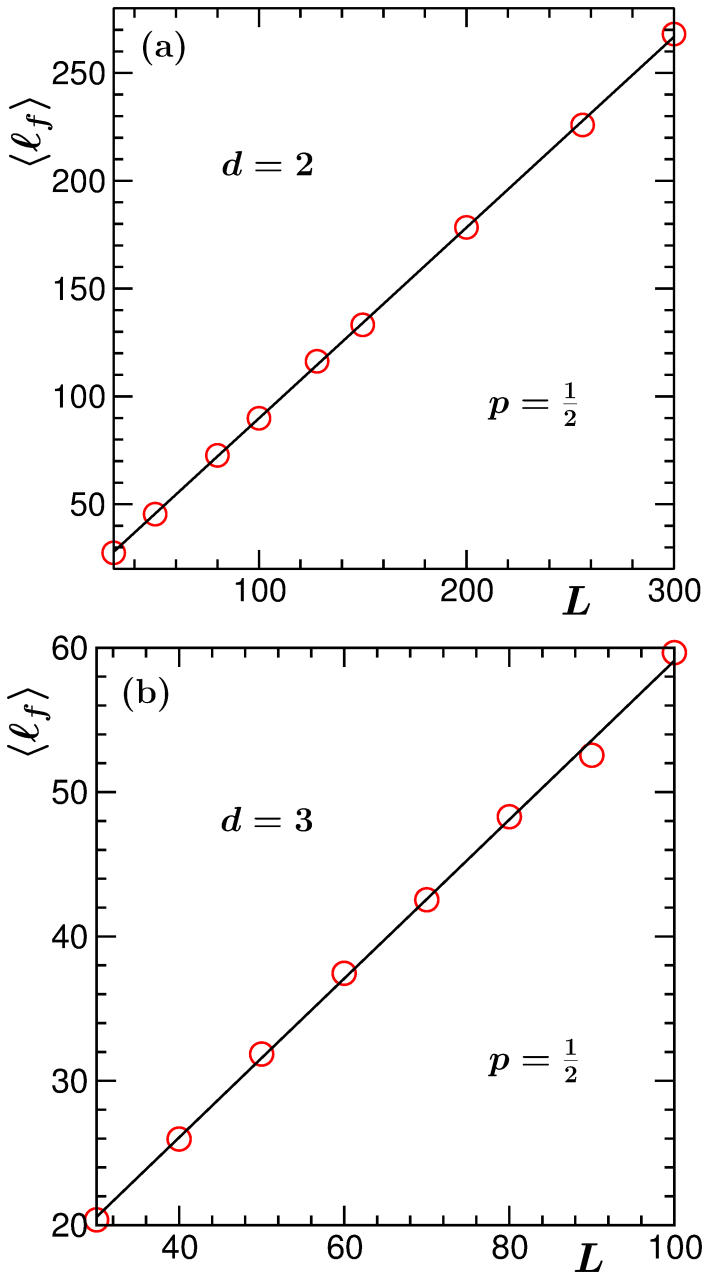

Figure 2.14: Average value of the final length is plotted versus system size, for $p = 1/2$ in (a) $d = 2$ and (b) $d = 3$. The solid lines represent linear fits to the simulation data sets.

also states that freezing is a more severe problem in $d = 3$ than in $d = 2$. [Analogous results were discussed in Refs. [28, 29] obtained from special initial configurations.]

In Fig. 2.14(a) and 2.14(b) we plot $\langle \ell_f \rangle$ as a function of L, for $p = 1/2$, in $d = 2$ and 3, respectively. The dependence in both the dimensions turns out to be linear. Here it is worth mentioning that occasionally artificial freezing in computer simulations can be observed, for slow dynamics, due to periodicity in random numbers, when system sizes are very large. To us, this also does not appear to be true in the present case. Here the phenomena can be attributed to the structure. How the system size at this temperature is affecting the structure and dynamics, to provide a linear relation between frozen length and system size, is an intriguing question. The observation, nevertheless, provides confidence, by looking at the numbers in the plots [Figs. 2.14(a) and 2.14(b)], that our presented results on growth and aging did not suffer from this effect. Here we recall that finite-size effects start appearing when $\ell \simeq 0.4L$, whereas $\langle \ell_f \rangle$ in both the dimensions are much larger than this limit. Furthermore, linear dependence of $\langle \ell_f \rangle$ on L, does not call for reanalysis of data via finite-size scaling method by replacing L by $\langle \ell_f \rangle$. Note that in Figs. 2.14(a) and 2.14(b) we presented results only up to $L = 300$ and 100, respectively, by considering the fact that achieving freezing for very large systems is computationally very difficult, particularly when our observation suggests a linear relationship.

2.4 Conclusion

We have studied pattern, growth and aging properties of the nearest neighbor Ising model via Monte Carlo simulations [35] in $d = 2$ and 3, using Glauber spin-flip mechanism [35, 40]. We quench our system to zero temperature in both the cases. Flips which did not change energy were accepted with two probabilities, viz., $p = 1$ and $1/2$, referred to as the Metropolis and Glauber algorithms, respectively, to check for their relative effects on the behavior of various quantities. We quantify the value of aging exponent λ via finite-size scaling [15, 16] and other methods of analysis. The results were compared with the corresponding results for quenches to nonzero temperatures [15].

The reason behind considering different values for the acceptance probability p is the following. Unusually slow growth was reported for $T_f = 0$ in $d = 3$. Furthermore, for $p = 0$ it was observed that coarsening practically does not occur. Thus, it is important to check the dependence of the choice of p on dynamics. Our observation with respect to this is important which we summarize below.

For $p = 1/2$, compared to $p = 1$, growth amplitude is lower. This fact is true for both $d = 2$ and 3. Thus, to observe the asymptotic scaling regime, e.g., $\alpha = 1/2$ behavior in the growth law in $d = 3$, one will require to simulate systems for longer period of time as p decreases. This is because of the fact that the crossover occurs at same length scale, irrespective of the value of p, implying delay (in time) of the onset as one lowers the value of p. This explains the fact why in the limiting case $p = 0$ coarsening gets completely arrested. For any nonzero p, however, if adequately large systems are simulated for long enough time, asymptotic scaling laws can be observed. In $d = 3$, nevertheless, the aging exponent for $T_f = 0$ did not appear to be the same as that for high temperature, even in the post crossover regime for growth. This and other features we summarize below.

The autocorrelations, in both the dimensions, exhibit good scaling with respect to ℓ/ℓ_w, and the late time decay can be described by a power-law with an exponent λ. In $d = 2$, the value of λ matches with the LM prediction. But for $d = 3$, the result is not consistent with the LM prediction and also differs from the high temperature results [15]. This also seems to be much below the FH lower-bound. We show that this is not a true violation of the bound, if the small k behavior of $S(k, t_w)$ is appropriately taken care of in the structure factor analysis. Here note that the zero temperature structure in $d = 3$, in the scaling regime, is incompatible with the well known Ohta-Jasnow-Kawasaki form. The role of structure on aging has been further demonstrated via the study of aging in $d = 2$ and pre-scaling regime in $d = 3$.

Since finite-size scaling analysis was performed for the estimation of the aging exponent, justification of this in the present situation is needed because the systems undergo freezing. This is to eliminate the possibility that freezing does not occur at a fixed length scale. In that case a finite-size or similar scaling arguments of statistical mechanics cannot be applied to obtain information on the behavior of a quantity in the thermodynamic limit. For this reason we have shown that the frozen length as well as the onset of size effects appear at fixed fractions of the system size.

Close to the frozen length, the dynamics is very slow for $d = 3$. If an analysis is performed, to arrive at the domain growth law, via scaling of the corresponding relaxation time with the system size, a different, misleading conclusion can be arrived at. We intend to address this issue of very late time dynamics in a future communication.

From simulations of very large systems we confirmed that in $d = 3$ also the growth at zero temperature follows the Lifshitz-Allen-Cahn law. Previously various authors have pointed out that the slow growth with $\alpha = 1/3$ could be due to lattice anisotropy. But such fact should be applicable in $d = 2$ as well. The observed differences between the 2D

and 3D cases can perhaps be explained via the difference with respect to the roughening transition. Nevertheless, questions remain. Observation of $\alpha = 1/2$ at very late time in $d = 3$ may imply that the anisotropy is unimportant for large structure. On the other hand, in the equilibrium context certain properties carry the information of anisotropy even in the thermodynamic limit [52].

Appendix

Finite-size scaling

Here we provide some details on the finite-size scaling analysis, results for which have been presented in section 2.3. Since $x\,(= \ell/\ell_w)$, in Eq. (2.18), is already dimensionless, we choose $y = x'/x$, where $x' = L/\ell_w$, given the requirement that y must be dimensionless. This provides the form of y in Eq. (2.20). For the sake of convenience, we intend to write $C_{\rm ag}(t, t_w)$ as a function of y. Then,

$$C_{\rm ag}(t, t_w) = Ae^{-By/y_w} \left(\frac{y_w}{y}\right)^{-\lambda}, \tag{A.1}$$

where $y_w = L/\ell_w$, i.e., the value of y at $t = t_w$. Realization of the form of Y in Eq. (2.19) is then straight-forward. Note that in Eq. (2.19) we have absorbed y^λ inside Y.

Given that we start our measurement from t_w, $x' = L/\ell_w$ provides the fraction of the total system size available to explore during the simulation. Coming back to the above comment "fraction of the total system size available to explore", we mention that this quoted fact allows a finite-size scaling analysis only via the variation of t_w, without exploring different system sizes. This is because, we state again, with the variation of t_w, the above mentioned fraction varies, providing different effective system sizes. This fact is demonstrated by achieving collapse of data from different values of L and t_w.

The limiting behavior of Y can be described as follows. In the thermodynamic limit, i.e., for $\ell << L$ $(y \to \infty)$, we can write

$$Y = Ay^\lambda, \tag{A.2}$$

so that Eq. (A.1) is recovered. In the other limit, in finite systems, particularly due to frozen dynamics, we do not expect $C_{\rm ag}(t, t_w)$ to vanish. This may lead to a rather flat appearance of Y for small y. Such characteristic features, along with a collapse

of data from various different L and t_w values, can be realized by choosing λ and B appropriately.

At nonzero temperatures, there exists coupling between equilibration of domain magnetization and that of the whole system [3], till large value of x. Given that the former is related to the critical fluctuation [53], for very low value of T_f, the relaxation related to the domain magnetization occurs very fast, to a value almost unity. Nevertheless, a minor jump in the autocorrelation function very close to $x = 1$, providing a higher effective exponent for very small x, exists. Thus, we avoided the data point corresponding to $x = 1$ in all cases, for the finite-size scaling analysis. Furthermore, for very small T_f values, the scaling of $C_{\rm ag}$, with respect to ℓ/ℓ_w, is expected to appear from smaller t_w values. Nevertheless, deviations at early time is observed, particularly in $d = 3$. This may be due to slow crossover to $t^{1/2}$ growth behavior extending up to very late time. Thus, for this scaling analysis, we have chosen rather large values of t_w in this dimension.

In one of the earlier studies for high temperature [15], a good data collapse was reported for finite-size scaling analysis, with the finite-size ℓ in the scaling variable y. But an ideal choice is the thermodynamic limit values. There can be two possible ways: (i) to adopt $\ell \sim t^{1/2}$ behavior, (ii) to use length from a much larger system size that does not exhibit finite-size effects over the time-scale of analysis. We followed the latter method here – for d = 2, ℓ was taken from L = 2048 and for d = 3, we used ℓ from L = 750. We believe that there is scope for the improvement of the 3D results via consideration of larger systems and by treating γ as an adjustable parameter in the finite-size scaling analysis.

Copyright and Permission

The results of this chapter have been published in:
Nalina Vadakkayil, Saikat Chakraborty, and Subir K. Das, "Finite-size scaling study of aging during coarsening in non-conserved Ising model: The case of zero temperature quench", J. Chem. Phys. **150**, 054702 (2019).

We have reproduced the materials here with kind permission from the American Institute of Physics Publishing. See the publication link below:
https://aip.scitation.org/doi/full/10.1063/1.5052418

References

[1] S. Chakraborty, *Dynamics of Coarsening in Systems of Non-living and Living Objects*, Ph. D. thesis, Jawaharlal Nehru Centre for Advanced Scientific Research, India, 2016.

[2] A.J. Bray, Adv. Phys. **51**, 481 (2002).

[3] S. Puri and V. Wadhawan (ed.), *Kinetics of Phase Transitions* (CRC Press, Boca Raton, 2009).

[4] D.S. Fisher and D.A. Huse, Phys. Rev. B **38**, 373 (1988).

[5] F. Liu and G.F. Mazenko, Phys. Rev. B **44**, 9185 (1991).

[6] S.N. Majumdar and D.A. Huse, Phys. Rev. E **52**, 270 (1995).

[7] C. Yeung, M. Rao, and R.C. Desai, Phys. Rev. E **53**, 3073 (1996).

[8] F. Corberi, E. Lippiello, and M. Zannetti, Phys. Rev. E **74**, 041106 (2006).

[9] M. Henkel, A. Picone, and M. Pleimling, Europhys. Lett. **68**, 191 (2004).

[10] T. Ohta, D. Jasnow, and K. Kawasaki, Phys. Rev. Lett. **49**, 1223 (1982).

[11] J.J. Arenzon, L.F. Cugliandolo, and M. Picco, Phys. Rev. E **91**, 032142 (2015).

[12] E. Lorenz and W. Janke, Europhys. Lett. **77**, 10003 (2007).

[13] J.J. Arenzon, A.J. Bray, L.F. Cugliandolo, and A. Sicilia, Phys. Rev. Lett. **98**, 145701 (2007).

[14] A. Sicilia, J.J. Arenzon, A.J. Bray, and L.F. Cugliandolo, Phys. Rev. E **76**, 061116 (2007).

[15] J. Midya, S. Majumder, and S.K. Das, J. Phys.: Condens. Matter **26**, 452202 (2014).

[16] J. Midya, S. Majumder, and S.K. Das, Phys. Rev. E **92**, 022124 (2015).

[17] C. Yeung and D. Jasnow Phys. Rev. B **42**, 10523 (1990).

[18] S.M. Allen and J.W. Cahn, Acta Metall. **27**, 1085 (1979).

[19] C. Yeung, Phys. Rev. Lett. **61**, 1135 (1988).

[20] S.N. Majumdar, D.A. Huse, and B.D. Lubachevsky, Phys. Rev. Lett. **73**, 182 (1994).

[21] S.K. Das and S. Chakraborty, Eur. Phys. J. Spec. Top. **226**, 765 (2017).

[22] H. van Beijeren and I.M. Nolden, in *Structure and Dynamics of Surfaces II: Phenomena, Models and Methods, Topics in Current Physics*, edited by W. Schommers and P. von Blanckenhagen (Berlin, Springer, 1987), Vol. 43.

[23] J.G. Amar and F. Family, Bull. Am. Phys. Soc. **34**, 491 (1989).

[24] J.D. Shore, M. Holzer, and J.P. Sethna, Phys. Rev. B **46**, 11376 (1992).

[25] A. Lipowski, Physica A **268**, 6 (1999).

[26] S. Cueille and C. Sire, J. Phys. A **30**, L791 (1997).

[27] F. Corberi, E. Lippiello, and M. Zannetti, Phys. Rev. E **78**, 011109 (2008).

[28] J. Olejarz, P.L. Krapivsky, and S. Redner, Phys. Rev. E **83**, 051104 (2011).

[29] J. Olejarz, P.L. Krapivsky, and S. Redner, Phys. Rev. E **83**, 030104(R) (2011).

[30] S. Chakraborty and S.K. Das, Phys. Rev. E **93**, 032139 (2016).

[31] T. Blanchard, F. Corberi, L.F. Cugliandolo, and M. Picco, Europhys. Lett. **106**, 66001 (2014).

[32] T. Blanchard, L.F. Cugliandolo, M. Picco, and A. Tartaglia, J. Stat. Mech. P113201 (2017).

[33] S. Chakraborty and S.K. Das, Europhys. Lett. **119**, 50005 (2017).

[34] K. Humayun and A.J. Bray, J. Phys. A: Math. Gen. **24**, 1915 (1991).

[35] D.P. Landau and K. Binder, *A Guide to Monte Carlo Simulations in Statistical Physics* (Cambridge University Press, Cambridge, 2009).

[36] M.E. Fisher, in *Critical Phenomena*, edited by M.S. Green (Academic, London, 1971).

[37] M.E. Fisher and M.N. Barber, Phys. Rev. Lett. **28**, 1516 (1972).

[38] D.W. Heermann, L. Yixue, and K. Binder, Physica A **230**, 132 (1996).

[39] S.K. Das, Molecular Simulation **41**, 382 (2015).

[40] R.J. Glauber, J. Math. Phys. **4**, 294 (1963).

[41] S. Majumder and S.K. Das, Phys. Rev. E **84**, 021110 (2011).

[42] D.A. Huse, Phys. Rev. B **34**, 7845 (1986).

[43] V. Spirin, P.L. Krapivsky, and S. Redner, Phys. Rev. E **63**, 036118 (2001).

[44] P. Mullick and P. Sen, Phys. Rev. E **95**, 052150 (2017).

[45] S. Majumder and S.K. Das, Phys. Rev. E **81**, 050102 (2010).

[46] S. Majumder and W. Janke, Phys. Rev. E **93**, 032506 (2016).

[47] S.K. Das, Europhys. Lett. **97**, 46006 (2012).

[48] S.K. Das, Phys. Rev. E **87**, 012135 (2013).

[49] E. Mani and H. Löwen, Phys. Rev. E **92**, 032301 (2015).

[50] C. Tung, J. Harder, C. Valeriani, and A. Cacciuto, Soft Matter **12**, 555 (2016).

[51] J. Olejarz, P.L. Krapivsky, and S. Redner, Phys. Rev. Lett. **109**, 195702 (2012).

[52] S.K. Das, S.A. Egorov, P. Virnau, D. Winter, and K. Binder, J. Phys.: Condens. Matter **30**, 255001 (2018).

[53] M.E. Fisher, Rep. Prog. Phys. **30**, 615 (1967).

Chapter 3

Influence of Roughening Transition on Nonequilibrium Dynamics of the Three-Dimensional Ising model

3.1 Introduction

Over past several decades there has been significant interest [1–25] in the understanding of ordering dynamics following quenches of paramagnetic configurations to the ferromagnetic region by crossing the critical temperature T_c. A large fraction of the literature, in this direction, is related to the studies of Ising model. Metastability in this model, following quenches to the final temperature $T_f = 0$, due to interesting structure formation, drew attention recently [6–8, 10, 11, 13–17]. Evolution to such frozen states, in space dimension $d = 3$, is thought to be much slower [7, 12–14] than that for quenches to nonzero values of T_f ($< T_c$). Some works speculated [9, 15–17], as mentioned in the previous chapter, that such *glass-like* slow dynamics may not be specific to $T_f = 0$. Rather, this may have the origin at the roughening transition [26], that occurs at a much higher temperature T_R ($< T_c$). Note that the roughening transition [26] is related to the change of interface from rough to smooth. The corresponding temperature, T_R, is the roughening transition temperature. Above this temperature, the interface thickness grows with the system size. Given that below T_R interfaces are sharp, a thought for slow dynamics and freezing has justification. Nevertheless, validity of this should be established via thorough investigations.

The rest of the discussion in this section, except for the last paragraph, is similar to that in the Introductory section of Chapter 2. Only for the sake of completeness we repeat it here.

Some of the key aspects of ordering dynamics [23–25, 27–37] are: i) self-similarity and scaling property of structure, ii) growth of the latter, and iii) related aging. The structure is typically probed via the two-point equal time (t) correlation function [27], which, for a spin system, reads,

$$C(r,t) = \langle S_i(t)S_j(t)\rangle - \langle S_i(t)\rangle\langle S_j(t)\rangle, \tag{3.1}$$

S_i and S_j representing orientations of spins or atomic magnets at sites i and j, located r distance apart. It is also customary to study the Fourier transform of $C(r,t)$, the structure factor, $S(k,t)$, k being the wave number [27]. The latter has direct experimental relevance. These quantities obey certain scaling properties when the growth is self-similar. E.g., in simple situations, when structures are non-fractal, $C(r,t)$ satisfies a scaling form [27],

$$C(r,t) \equiv \tilde{C}(r/\ell), \tag{3.2}$$

ℓ being the average domain size or the characteristic length scale of the growing system at time t and $\tilde{C}(x)$ a time-independent master function. In such a situation ℓ is expected [27] to grow as $\sim t^{\alpha}$. A power-law behavior is expected for aging phenomena also. In the latter case the autocorrelation function [28, 29], defined as,

$$C_{\rm ag}(t,t_w) = \langle S_i(t)S_i(t_w)\rangle - \langle S_i(t)\rangle\langle S_i(t_w)\rangle, \tag{3.3}$$

should scale as $\sim (\ell/\ell_w)^{-\lambda}$, in the asymptotic limit when $\ell >> \ell_w$. Here, t_w ($\leq t$) is the waiting time or age of the system and ℓ_w is the value of ℓ at $t = t_w$.

For uniaxial ferromagnets one expects [27, 36] $\alpha = 1/2$. The structure in this case is supposed to be described by the Ohta-Jasnow-Kawasaki (OJK) function [24, 27]:

$$C(r,t) = \frac{2}{\pi}\sin^{-1}[\exp(-r^2/Dt)], \tag{3.4}$$

D being a constant. Note that while the form of $C(r,t)$ and the value of α are independent of space dimension, λ changes with d. The values of λ for this ordering, as obtained by Liu and Mazenko (LM) [23], are expected to be $\simeq 1.67 = \lambda^3_{\rm LM}$ in $d = 3$, whereas in $d = 2$, it is $\lambda^2_{\rm LM} \simeq 1.29$. Unless otherwise mentioned, in the rest of the chapter all our discussions are for $d = 3$.

While these theoretical predictions were observed to be valid for moderately high values of T_f, striking deviations were reported for $T_f = 0$. In the latter case, several works concluded that $\alpha = 1/3$ or the growth is even slower. A few studies [9, 15–17], however, hinted that α remains $1/2$ even for $T_f = 0$, only arrival at such a scaling gets extraordinarily delayed. Most recently it was reported that the OJK function does not [17] describe the pattern at $T_f = 0$. Furthermore, λ was also estimated [17] to be much weaker than $\lambda^3_{\rm LM}$. We repeat, these observations were thought to be specific to $T_f = 0$. However, thorough investigations, we believe, are necessary, in order to arrive at the correct and complete picture. It needs to be understood if such anomalies bear any connection with any other special point. If such a special point turns out to be that of the roughening transition, important relation concerning structure and dynamics [38] can be established in the nonequilibrium context.

As evident from the discussion above, in this work we present results from the Monte Carlo (MC) simulations [37] of the Ising model [37] in $d = 2$ and 3, emphasis being on the latter dimension, for nonconserved order-parameter dynamics, by using Glauber spin-flip dynamics [37, 39] that mimics ordering in a uniaxial ferromagnet. We consider a wide range of final temperature, starting configurations always being perfectly random mix of up and down spins in 50:50 proportion. Our observations are the following. The above mentioned anomalous features in $d = 3$ are not specific to $T_f = 0$. In fact the onset of the anomalies occurs at the roughening transition. This was hitherto unconfirmed. This observation promises us to establish important structure-dynamics connection for ferromagnetic ordering. Structure can affect dynamics [38]. Our observation reconfirms this in an interesting context. The roughening transition here leads to the mismatch of the correlation function with the OJK function on the lower side of T_R. This has the origin in the departure of the distribution of an order-parameter related auxiliary field from the Gaussian character at low temperature. Phenomena observed in Ising model have been instrumental in understanding plethora of experimental observations on phase transitions [37, 40]. We believe that these results will inspire novel investigations, thereby explaining intriguing dynamical phenomena in the nonequilibrium domain. Our key results have been verified by sophisticated finite-size scaling analysis [33, 41, 42].

3.2 Model and Methods

The model and methods are similar to those of chapter 2. Readers, thus, may like to move to the next section.

We choose $J > 0$ in the Ising Hamiltonian [37, 40]

$$H = -J \sum_{<ij>} S_i S_j, \tag{3.5}$$

where S_i and S_j can take values $+1$ and -1, corresponding to up and down orientations of the atomic magnets. We study this model on a simple cubic lattice, having $T_c \simeq 4.51 J/k_B$ [37], where k_B is the Boltzmann constant. For the limited set of results in $d = 2$, we considered square lattice. Note that in this case $T_c = 2.269185...J/k_B$ [37]. In $d = 3$, the value of T_R for this model is $\simeq 2.57 J/k_B$ [26], whereas a non-zero roughening transition temperature does not exist in $d = 2$.

Moves in our MC simulations were tried by randomly choosing a spin and changing its sign. These were accepted by following standard Metropolis criterion [37]. Unit of time in our simulations is a MC step (MCS) that consists of L^d trial moves, L being the linear dimension of a cubic or a square box, in units of the lattice constant.

All our results are presented after averaging over runs with 50 independent random initial configurations, with $L = 512$. Periodic boundary conditions were applied in all possible directions. Average domain lengths were measured, from the simulation snapshots, as the first moments [35] of the domain size distribution function, in which length of a domain was estimated as the distance between two successive interfaces along any Cartesian direction. Results on the structure and growth were obtained after appropriately eliminating the thermal noise in the snapshots via a majority spin rule [35]. We repeat, unless otherwise stated, the results are from $d = 3$.

3.3 Results

In Fig. 3.1 we show ℓ versus t plots for several values of T_f. For $T_f = 0$ few early works were suggestive of [7, 12–14] an exponent $\alpha = 1/3$ or even slower growth. Similar quantitative behavior is seen here as well, after a rapid initial growth. However, at very late time a crossover [15, 17] of the exponent to a higher value, viz., $\alpha = 1/2$, can be appreciated. The very early works could not capture this, either due to consideration of small systems or simulations over short periods, owing, perhaps, to inadequate computational resources. As can be seen, such a *slow looking* early growth is not unique to $T_f = 0$. The data sets for nonzero T_f values also exhibit similar trend. However, with the increase of T_f departure from this slow behavior occurs earlier, finally the $1/3$ regime ceasing to exist for $T_f = T_R = 2.57$. At this stage, it is worth warning that the

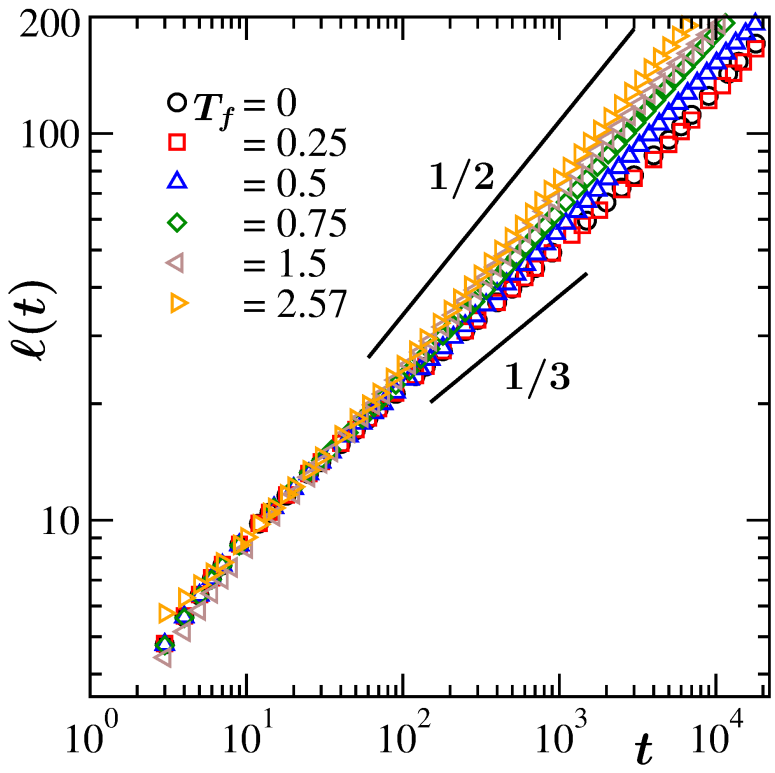

Figure 3.1: Average domain lengths, $\ell(t)$, are plotted versus time, on a log-log scale. Results from several different final temperatures are presented. The solid lines are power-laws. The values of the exponents are mentioned in appropriate places.

early evolution should not be taken seriously, at the quantitative level. This is because, during this period satisfaction of the scaling property of the correlation function is not observed, as demonstrated below.

In Fig. 3.2(a) we show plots of $C(r,t)$, from different times, by scaling the distance axis by ℓ, for $T_f = 0.5$. It appears that the collapse starts from $t \gtrsim 1000$, approximately the time since when departure to $\alpha = 1/2$ behavior starts. This general picture is true for other low temperatures also. In Fig. 3.2(b) we have shown $C(r,t)$, again versus r/ℓ, from the scaling regimes of different T_f values. Interestingly, $\tilde{C}(r/\ell)$ at different T_f values do not agree with each other. However, with the increase of T_f the agreement with the OJK function $[\tilde{C}_{\rm OJK}(r/\ell)]$ [24] keeps getting better. This observation suggests that perhaps there exists a special temperature $T_{\rm sp}$ $(< T_c)$, beyond which the coarsening dynamics is more unique than below it. In fact for $T_f = T_R$ the agreement between simulation data and the OJK function is quite well. We will return to this central theme after discussion of the basic results on aging.

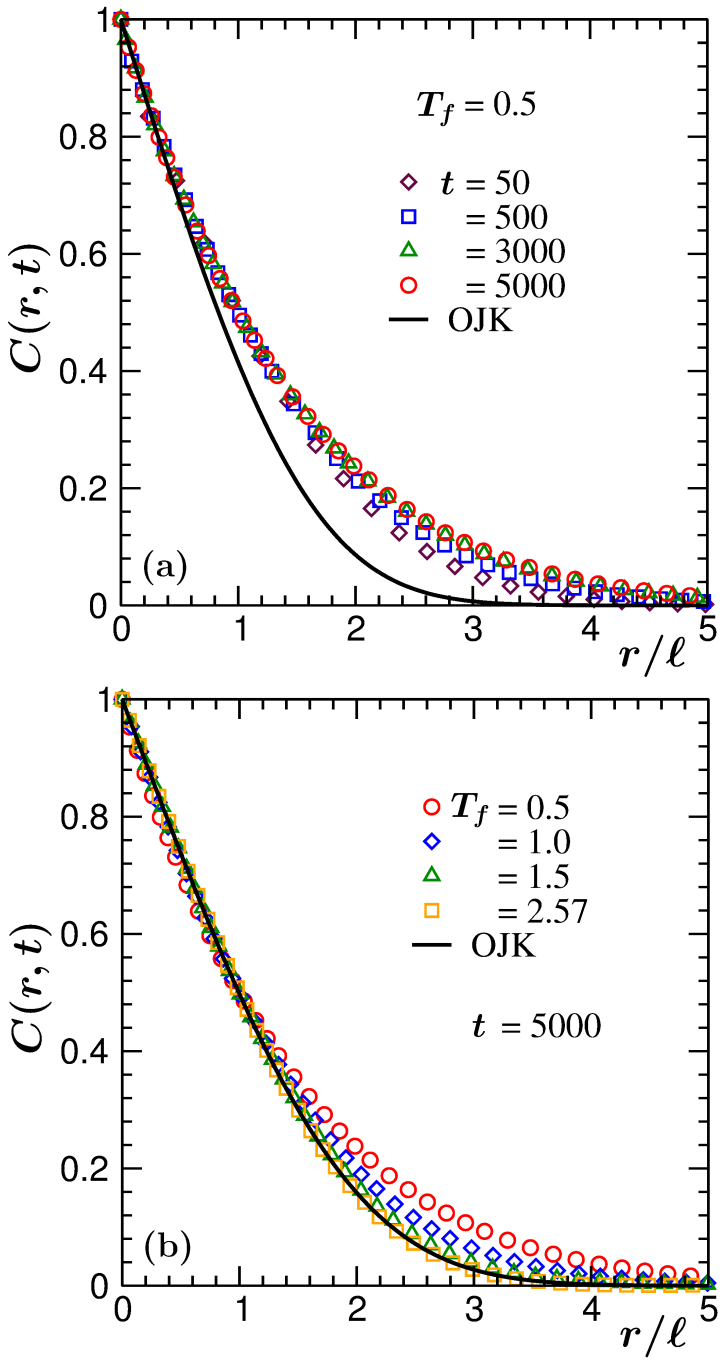

Figure 3.2: (a) Two-point equal time correlation functions, $C(r,t)$, are plotted versus the scaled distance r/ℓ, for $T_f = 0.5$. Data from few different times are shown. (b) Same as (a) but here we have shown $C(r,t)$ from different final temperatures. In each of the cases we have chosen $t = 5000$ that fall in the scaling regimes. In both (a) and (b) the continuous lines represent the Ohta-Jasnow-Kawasaki (OJK) function. The correlation functions have been plotted in such a way that there exists good collapse in the early abscissa range. Thus, the values of ℓ, when extracted from the collapse, will not have quantitative agreement with those in Fig. 3.1.

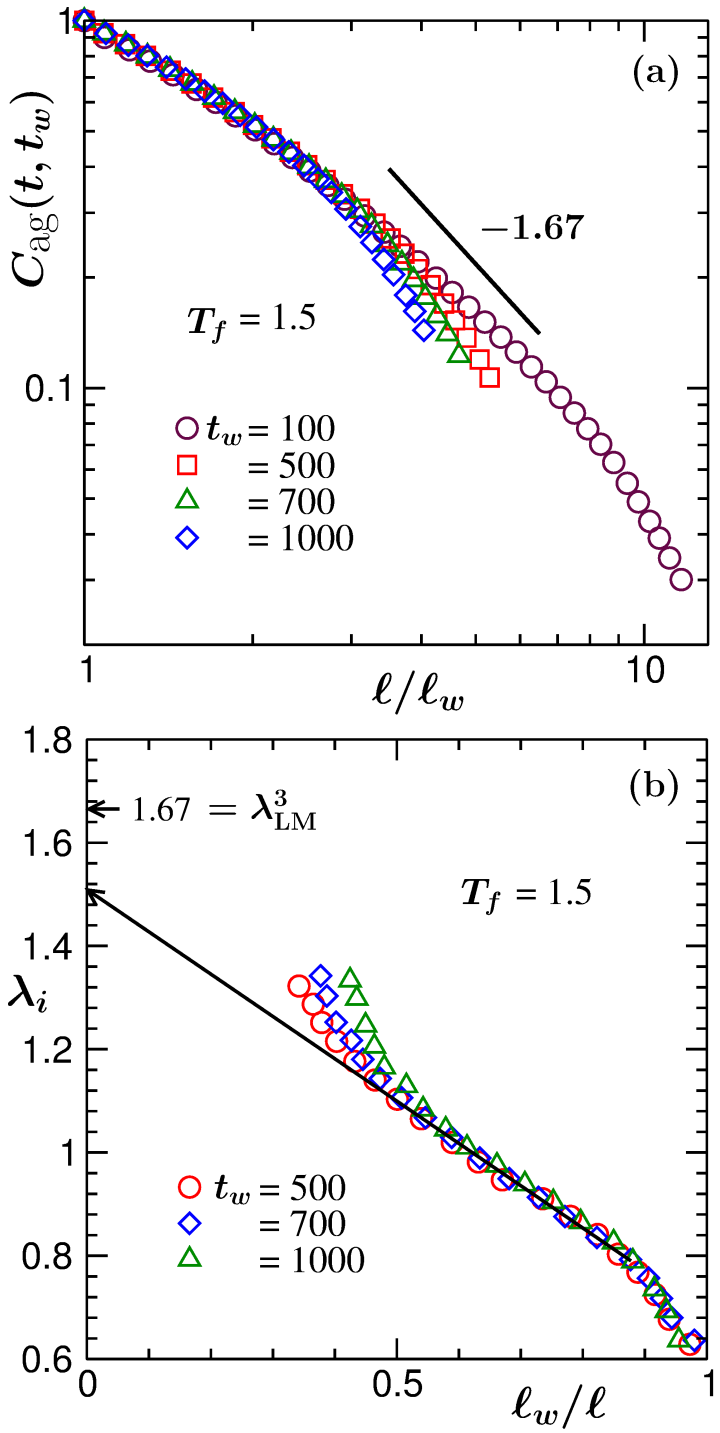

Figure 3.3: (a) $C_{\rm ag}(t, t_w)$, the autocorrelation function, is plotted versus ℓ/ℓ_w, on a log-log scale. Data from different t_w, for $T_f = 1.5$, are included. The solid line is a power-law with $\lambda = \lambda^3_{\rm LM} = 1.67$. (b) The instantaneous exponent λ_i is shown as a function of ℓ_w/ℓ, for the same final temperature. The arrow-headed line is a linear extrapolation to the $\ell/\ell_w = \infty$ limit, done by excluding the late time finite-size affected as well as early time domain magnetization relaxation parts.

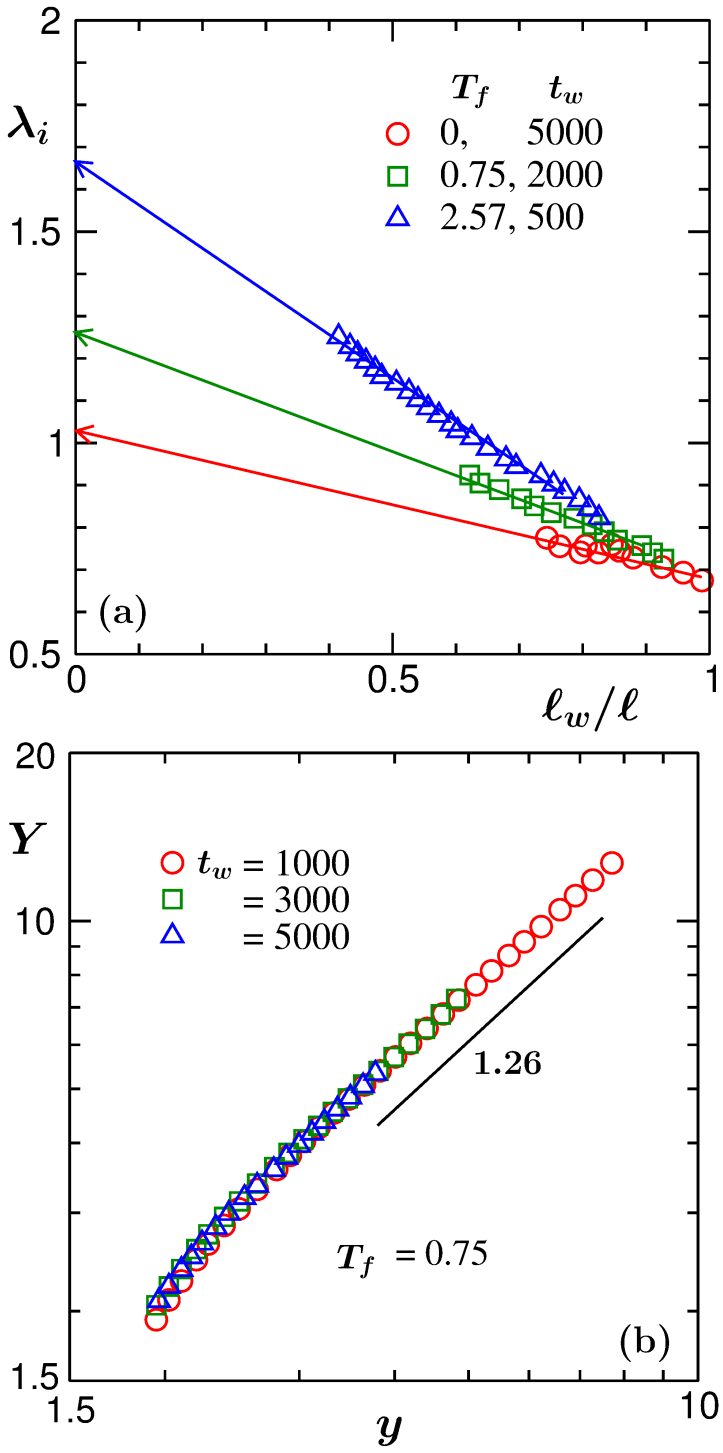

Figure 3.4: (a) Here we have shown λ_i, as a function of ℓ_w/ℓ, for a few different values of T_f. In each of the cases t_w belongs to the scaling regime. The arrow-headed lines are linear guides to the eyes. (b) Finite-size scaling plot of $C_{\rm ag}(t, t_w)$ for $T_f = 0.75$. The solid line there corresponds to a power-law with the value of the exponent mentioned near the line.

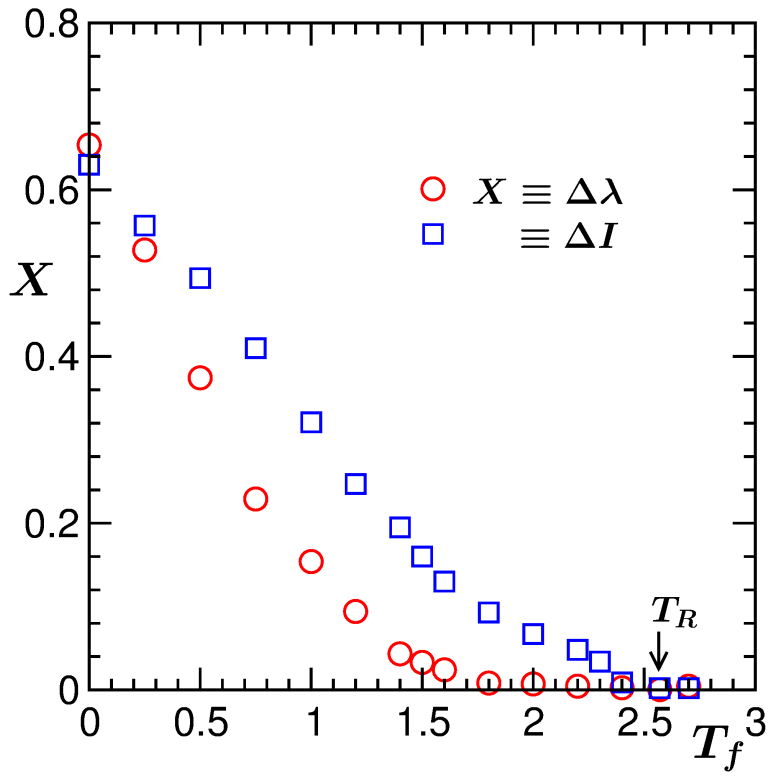

Figure 3.5: Plots are shown by comparing $\Delta\lambda$ and ΔI with the variation of T_f. The value of T_R is marked in the figure.

Fig. 3.3(a) shows plots of $C_{\rm ag}(t, t_w)$, with the variation of ℓ/ℓ_w. The value of T_f for this representative case is set at 1.5. Data sets from a few different waiting times are shown. Good collapse of data is visible for the considered values of t_w. There exist deviations from the master curve, for $\ell/\ell_w >> 1$. These are related to finite-size effects [33]. Decay in the finite-size unaffected regime does not appear consistent with the LM value [23] – see the disagreement with the solid line. In Fig. 3.3(b) we show the instantaneous exponent [29, 33] λ_i $[= -{\rm d}\ln C_{\rm ag}(t, t_w)/{\rm d}\ln(\ell/\ell_w)]$ as a function of ℓ_w/ℓ, for multiple choices of t_w lying in the scaling regime. The data sets appear linear in the finite-size unaffected regimes. Note that the early deviation is related to relaxation of domain magnetization and should be discarded from the process of estimation of λ. A linear extrapolation to $\ell/\ell_w = \infty$ provides $\lambda \simeq 1.5$. Given that the above quoted number lies between $\lambda^3_{\rm LM}$ and λ $(T_f = 0)$, being significantly different from each of these, one gets a strong hint on the presence of a special point.

In Fig. 3.4(a) we show plots of λ_i, as a function of ℓ_w/ℓ, for few different values of T_f. Here we discarded the parts corresponding to finite-size effects and equilibration of

domain magnetization. Furthermore, in each of the cases the results are from well inside the scaling regimes of t_w. The arrow-headed lines are related to the estimations of the values of λ, from linear extrapolations to the $\ell_w/\ell = \infty$ limit. Clearly, λ depends strongly on T_f. The accuracy of these estimates is validated by the independent quantifications of λ via a finite-size scaling method [33, 42]. A representative exercise related to this is shown in Fig. 3.4(b), for $T_f = 0.75$. In this figure Y is a t_w-independent scaling function and y is a dimensionless scaling variable. Note that here we have avoided studying systems of different sizes, contrary to the standard practice in the literature of such analysis. Instead, we have obtained collapse of data from different t_w values. Note that when t_w is varied a system has different effective sizes to grow further. Details of the scaling construction is provided below.

The behavior of λ_i in Fig. 3.3(b) and Fig. 3.4(a) suggests $\lambda_i = \lambda - B/x$, with $x = \ell/\ell_w$ and B being a constant, in the finite-size unaffected late time regime. This leads to a form [33, 42],

$$C_{\rm ag}(t, t_w) = Ae^{-B/x}x^{-\lambda}. \tag{3.6}$$

By taking $y = L/\ell$ as a scaling variable and $y_w = L/\ell_w$, a finite-size scaling function can be written as [17]

$$Y = C_{\rm ag}(t, t_w)e^{By/y_w}y_w^{\lambda}, \tag{3.7}$$

where Y contains a factor y^{λ}. When results from different t_w are plotted, for appropriate choices of the unknown parameters, including λ, there will be collapse of data sets that will satisfy the expected y^{λ} behavior at large y. This is demonstrated in Fig. 3.4(b) for $T_f = 0.75$. Here the collapse is obtained for $\lambda = 1.26$, the number being consistent with the value that was suggested by the exercise in Fig. 3.4(a).

Next we quantify the special temperature from a more systematic study. In Fig. 3.5 we show $\Delta\lambda = \lambda^3_{\rm LM} - \lambda(T_f)$, as a function of T_f. Given that the general expectation is $\lambda^3_{\rm LM}$, it is meaningful to look at the stated difference. There appears to be a nice convergence of the data set to zero as $T_f \to T_{\rm R} \simeq 2.57$. With respect to the deviation of $\tilde{C}(r/\ell)$ from the OJK form [24], that we observed above, there may also be a similar trend. In this case an appropriate quantity to consider is,

$$\Delta I = \int dr[\tilde{C}(r/\ell) - \tilde{C}_{\rm OJK}(r/\ell)]. \tag{3.8}$$

Here note that there exists an LM form for $C(r, t)$ as well [23]. However, this practically overlaps with the OJK function. It will be interesting to see if ΔI approaches zero at the same T_f as in the case of $\Delta\lambda$. Thus, in Fig. 3.5 we have included the T_f-dependence

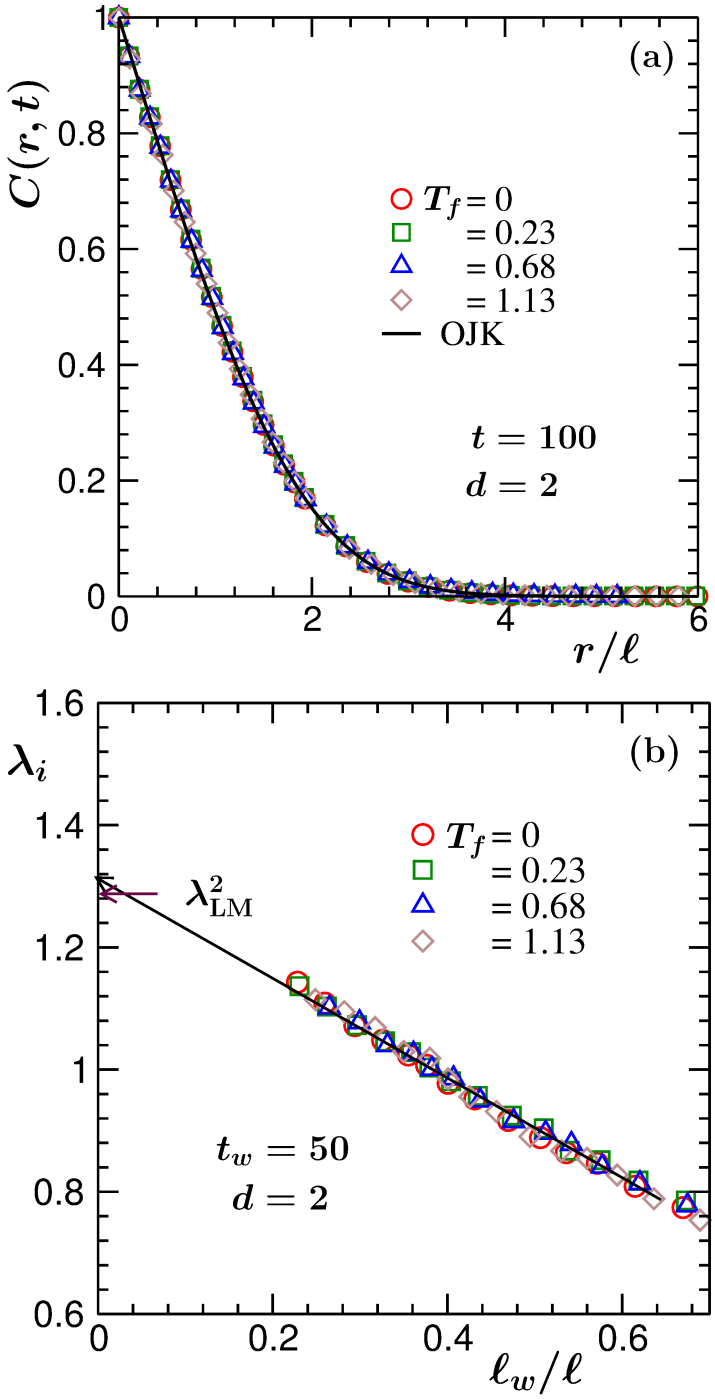

Figure 3.6: (a) Plots of scaled two-point equal time correlation functions, $C(r,t)$, from $d = 2$, for different T_f values. The time has been chosen from the scaling regime. The continuous line represents the OJK function. (b) The instantaneous exponent λ_i is plotted as a function of ℓ_w/ℓ, for different T_f values. The solid line is a common linear extrapolation of the data sets. The arrow-headed horizontal line points to the LM value of λ in $d = 2$.

of ΔI as well. Trend-wise, the presented data sets are in nice agreement with each other, over a wide range of temperature, within a factor. For the calculation of ΔI we have, for each T_f, superimposed small r values of $C(r,t)$ with the OJK form as best as possible.

In Fig. 3.6 we show analogous results from $d = 2$. Fig. 3.6(a) contains results for the scaled $C(r,t)$ and in Fig. 3.6(b) we have shown data for λ_i, as a function of ℓ_w/ℓ. For each of the cases results from a wide range of T_f are included. The anomalies present in $d = 3$ are clearly absent in this case. No detectable T_f-dependence can be observed. The theoretical expectations are satisfied over the whole range of T_f. Recall that in this dimension, a nonzero roughening transition temperature does not exist for this model.

3.4 Conclusions

From extensive Monte Carlo simulations [37], we have presented results on nonequilibrium dynamics in the Glauber [37, 39] Ising model. This mimics ordering in uniaxial ferromagnets. Our quantitative analysis of data from space dimension $d = 3$ on structure, growth and aging, over a wide range of temperatures below the critical point, suggests that the low temperature behavior is anomalous.

We show that the anomalies are not unique to the case of zero temperature quench, as was previously thought. Various quantities exhibit zero-temperature-like trend till a certain nonzero value of T_f. Above this temperature, behavior of all the aspects becomes consistent with various theoretical expectations [23, 24, 27, 36]. This *transition or special temperature* coincides with that of the roughening transition [26]. Such a conclusion appears more meaningful from the fact that these anomalies are absent in $d = 2$ and for this dimension roughening transition temperature is zero.

This is the first quantitative report on this matter. We believe, this will inspire further theoretical and experimental studies, being beneficial in understanding nonequilibrium dynamics of various types.

This article has been submitted to arXiv and is in communication with an American Physical Society Journal. See the arXiv link below:
https://arxiv.org/abs/2106.16232

References

[1] V. Spirin, P.L. Krapivsky, and S. Redner, Phys. Rev. E **63**, 036118 (2001).

[2] V. Spirin, P.L. Krapivsky, and S. Redner, Phys. Rev. E **65**, 016119 (2001).

[3] P.M.C. de Oliveira, C.M. Newman, V. Sidoravicious, and D.L. Stein, J. Phys. A **39**, 6841 (2006).

[4] G. Kondrat and K. Sznajd-Weron, Phys. Rev. E **79**, 011119 (2009).

[5] J.J. Arenzon, A.J. Bray, L.F. Cugliandolo, and A. Sicilia, Phys. Rev. Lett. **98**, 145701 (2007).

[6] J. Olejarz, P.L. Krapivsky, and S. Redner, Phys. Rev. Lett. **109**, 195702 (2012).

[7] J. Olejarz, P.L. Krapivsky, and S. Redner, Phys. Rev. E **83**, 051104 (2011).

[8] J. Olejarz, P.L. Krapivsky, and S. Redner, Phys. Rev. E **83**, 030104 (2011).

[9] F. Corberi, E. Lippiello, and M. Zannetti, Phys. Rev. E **78**, 011109 (2008).

[10] T. Blanchard, F. Corberi, L.F. Cugliandolo, and M. Picco, Europhys. Lett. **106**, 66001 (2014).

[11] T. Blanchard, L.F. Cugliandolo, M. Picco, and A. Tartaglia, J. Stat. Mech. 2017, P113201.

[12] J.G. Amar and F. Family, Bull. Am. Phys. Soc. **34**, 491 (1989).

[13] J.D. Shore, M. Holzer, and J.P. Sethna, Phys. Rev. B **46**, 11376 (1992).

[14] S. Cueille and C. Sire, J. Phys. A **30**, L791 (1997).

[15] S.K. Das and S. Chakraborty, Eur. Phys. J. Spec. Top. **226**, 765 (2017).

[16] S. Chakraborty and S.K. Das, Europhys. Lett. **119**, 50005 (2017).

[17] N. Vadakkayil, S. Chakraborty, and S.K. Das, J. Chem. Phys. **150**, 054702 (2019).

[18] J. Denholm and B. Hourahina, J. Stat. Mech. **2020**, 093205 (2020).

[19] C. Godriche and M. Pleimling, J. Stat. Mech. **2018**, 043209 (2018).

[20] P. Mullick and P. Sen, Phys. Rev. E **95**, 052150 (2017).

[21] U. Yu, J. Stat. Mech. **2017**, 123203 (2017).

[22] L.F. Cugliandolo, Comptes Rendus Physique **16**, 257 (2015).

[23] F. Liu and G.F. Mazenko, Phys. Rev. B **44**, 9185 (1991).

[24] T. Ohta, D. Jasnow, and K. Kawasaki, Phys. Rev. Lett. **49**, 1223 (1982).

[25] C. Yeung, Phys. Rev. Lett. **61**, 1135 (1988).

[26] H. van Beijern and I. Nolden, in *Structure and Dynamics of Surfaces II: Phenomena, Models and Methods, Topics in Current Physics*, Vol. **43**, ed. W. Schommers and P. von Blanckenhagen (Springer, Berlin, 1987).

[27] A.J. Bray, Adv. Phys. **51**, 481 (2002).

[28] S. Puri and V. Wadhawan (ed.), *Kinetics of Phase Transitions* (CRC Press, Boca Raton, 2009).

[29] D.S. Fisher and D.A. Huse, Phys. Rev. B **38**, 373 (1988).

[30] C. Yeung, M. Rao, and R.C. Desai, Phys. Rev. E **53**, 3073 (1996).

[31] M. Henkel, A. Picone, and M. Pleimling, Europhys. Lett. **68**, 191 (2004).

[32] E. Lorenz and W. Janke, Europhys. Lett. **77**, 10003 (2007).

[33] J. Midya, S. Majumder, and S.K. Das, J. Phys.: Condens. Matter **26**, 452202 (2014).

[34] D.A. Huse, Phys. Rev. B **34**, 7845 (1986).

[35] S. Majumder and S.K. Das, Phys. Rev. E **84**, 021110 (2011).

[36] S.M. Allen and J.W. Cahn, Acta Metall. **27**, 1085 (1979).

[37] D.P. Landau and K. Binder, *A Guide to Monte Carlo Simulations in Statistical Physics* (Cambridge University Press, Cambridge, 2009).

[38] J. Midya and S.K. Das, Phys. Rev. Lett. **118**, 165701 (2017).

[39] R.J. Glauber, J. Math. Phys. **4**, 294 (1963).

[40] M.E. Fisher, Rep. Prog. Phys. **30**, 615 (1967).

[41] M.E. Fisher and M.N. Barber, Phys. Rev. Lett. **28**, 1516 (1972).

[42] J. Midya, S. Majumder, and S.K. Das, Phys. Rev. E **92**, 022124 (2015).

Chapter 4

Initial Correlation Dependence of Aging in Ordering Ferromagnets in Two and Three Space Dimensions

4.1 Introduction

Having been prepared at a high starting temperature (T_s), when a homogeneous mixture is quenched to a final temperature (T_f), that falls inside the miscibility gap, it renders unstable to fluctuation and separates into regions or domains rich in particles of similar type [1–5]. Kinetics of such phase separation is of immense interest from both scientific and technological viewpoints.

The discussion in the rest of the section has similarity with that in the Introductory part of Chapter 2.

The structure of a system during the evolution is usually characterized by the two-point equal time correlation function, $C(r,t)$, which is defined as,

$$C(r,t) = \langle \psi(\vec{r},t)\psi(\vec{0},t)\rangle - \langle \psi(\vec{r},t)\rangle\langle \psi(\vec{0},t)\rangle. \tag{4.1}$$

Here ψ, chosen to be a scalar, is a space ($\vec{r}$) and time (t) dependent order parameter. In many growth processes $C(r,t)$ exhibits a scaling behavior,

$$C(r,t) \equiv \tilde{C}(r/\ell(t)), \tag{4.2}$$

where $\ell(t)$ is a characteristic length scale, measured as the average size of the domains formed during this nonequilibrium evolution. To probe the aging during such evolution, often one studies the decay of the two-time auto-correlation function [6],

$$C_{\rm ag}(t,t_w) = \langle\psi(\vec{r},t)\psi(\vec{r},t_w)\rangle - \langle\psi(\vec{r},t)\rangle\langle\psi(\vec{r},t_w)\rangle, \tag{4.3}$$

where t and t_w ($\leq t$) are referred, respectively, to as the observation and waiting times.

Due to the violation of time-translation invariance in nonequilibrium systems, $C_{\rm ag}(t,t_w)$ for different t_w are not equivalent to each other. In other words, if this correlation function is plotted versus $t-t_w$, there will be no collapse of data for different values of t_w. However, it is found that in many systems $C_{\rm ag}(t,t_w)$ exhibits the scaling behavior [6–23]

$$C_{\rm ag}(t,t_w) \sim (\ell/\ell_w)^{-\lambda}, \tag{4.4}$$

where ℓ and ℓ_w are the average sizes of domains at times t and t_w, respectively. Note that ℓ typically has a power-law time dependence [1–4, 6]

$$\ell \sim t^{\alpha}, \tag{4.5}$$

in phase ordering systems. Here λ and α are referred to as the aging and growth exponents, respectively. Values of these exponents, along with few other properties [2, 24], define the nonequilibrium universality classes [2, 20].

It has been argued that, depending upon the spatial correlation in the initial configurations there can be different universality classes [20–22] – one for $T_s = \infty$ and the other for $T_s = T_c$, the latter being the critical temperature. Note here that at $T_s = \infty$ a system, in standard picture, has a correlation length $\xi = 0$ and at $T_s = T_c$, $\xi = \infty$, when the system is of thermodynamically large size [2, 3, 25]. For ordering in uniaxial ferromagnets [2, 25], this fact of universality has been studied in space dimension $d = 2$ [20, 21]. There the understanding is that even though α remains the same [20], λ and other dynamic and structural quantities are different in the two classes [20, 21, 26–28]. Note that the value of α here [2, 29] is $1/2$.

For quenches from T_c, the estimation of λ remained difficult, because of the complexity associated with it in the computer simulations. There exist two sources of finite size effects [30] in this case. First one is due to non-accessibility of $\xi = \infty$ in the initial correlation [30] and the second is related to the fact [31, 32] that $\ell < \infty$, always. Despite having these difficulties in understanding the aging behavior quantitatively, significant

progress has recently been made, following adoption of methods of analysis that are analogous to the popular techniques used for extracting information about equilibrium systems.

There has been studies on quantification of λ in phase separating binary mixtures in different space dimensions, d, [14, 15], via formulation and application of finite-size scaling technique [14, 30] to Monte Carlo (MC) simulation results, for quenches with initial $\xi = 0$. For this and a number of other situations, including the ferromagnetic case, there are studies which demonstrated [14–18] that λ satisfies certain bounds. Here note that Fisher and Huse (FH) argued [7]:

$$\lambda \geq \frac{d}{2}. \tag{4.6}$$

Later, Yeung, Rao and Desai (YRD) [9] provided a more accurate and generic bound:

$$\lambda \geq \frac{d+\beta}{2}, \tag{4.7}$$

where β is an exponent related to the short wave number (k) behavior of structure factor [33], viz.,

$$S(k \to 0, t_w) \sim k^{\beta}. \tag{4.8}$$

For random initial configurations ($\xi = 0$), $\beta = 0$ and so, the YRD bound coincides with that of FH. For nonconserved order parameter, when $T_s = \infty$, $\beta = 0$ even in the long time limit. The latter, however, is not true for the conserved order parameter case [33–35]. This is one of the reasons why the values of λ in these two cases differ vastly, irrespective of space dimension, for quenches with $\xi = 0$.

When started from $T_s = T_c$, it is expected that one will have different structural scaling [20, 21]. If so, the bounds on λ will also be different from that when quenched from $T_s = \infty$. This provides an intuitive understanding that λ will be different for $T_s = \infty$ and $T_s = T_c$, giving rise to different universalities. This is demonstrated, as already stated, theoretically and computationally, for the nonconserved case [20, 21] in $d = 2$.

Here our objective is to estimate λ for $\xi = \infty$ in the three-dimensional Ising model via Monte Carlo simulations and also to revisit the case of $d = 2$, in the case of nonconserved order parameter dynamics. The results are discussed in the background of available analytical information [7, 9, 21], and we also show that the obtained values of λ are

consistent with the YRD bound. We will compare our results with the case of conserved order parameter dynamics [2] for the quenches from $T_s = \infty$ as well as $T_s = T_c$.

4.2 Model and Methods

In view of the fact that the model and methods for this contribution are already described in Chapters 2 and 3, readers may move to the next section.

We study nonequilibrium dynamics in uniaxial ferromagnets, via Glauber spin flip [36] Monte Carlo methods [37–39], using the Ising model [25] on a 2D square lattice in $d = 2$ and on a simple cubic lattice in $d = 3$, with periodic boundary conditions [38] applied in all the directions. The Hamiltonian of the model is given by [25, 38]

$$H = -J \sum_{<ij>} S_i S_j;\ S_i = \pm 1;\ J > 0, \tag{4.9}$$

where the values $+1$ and -1 correspond to up and down spins. The value of critical temperatures of this model [25, 38] in $d = 2$ and 3 are $= 2.269185...J/k_B$ and $\simeq 4.51 J/k_B$, respectively, where J is the interaction strength and k_B is the Boltzmann constant.

A trial move in the Glauber Ising model (GIM) is performed by flipping a randomly selected spin. The probability of acceptance of trial moves is given by [37–39]

$$P(i \to j) = \min(1, \exp(-(E_j - E_i)/k_B T_f)), \tag{4.10}$$

where $E_{i(j)}$ is the energy of the state $i(j)$. Time in our simulation is estimated in units of MC steps (MCS), where one MCS is equivalent to L^2 and L^3 trial moves in $d = 2$ and 3 respectively, L being the linear dimension of a square/cubical box, in units of the lattice constant a. In the rest of the chapter, we set J, k_B and a to unity.

We mostly quench the systems from $T_s = T_c^L$, T_c^L being the system-size dependent critical temperature [30, 40], except for a few cases for which we performed quenches from $T_s = \infty$, only for the purpose of comparison. For both the starting temperatures the final temperature was $T_f = 0.6 T_c$. Here note that for quenches to $T_f < T_c$ the asymptotic values of α are said to be same [21] for both $T_s = \infty$ and $T_s = T_c$. On the other hand, following a quench to T_c from other temperatures relaxation of a system is dictated by different value of the exponent.

In order to obtain the equilibrium configurations at T_c^L, we have performed simulations using Wolff algorithm [41], that, to a good degree, helps avoiding the critical

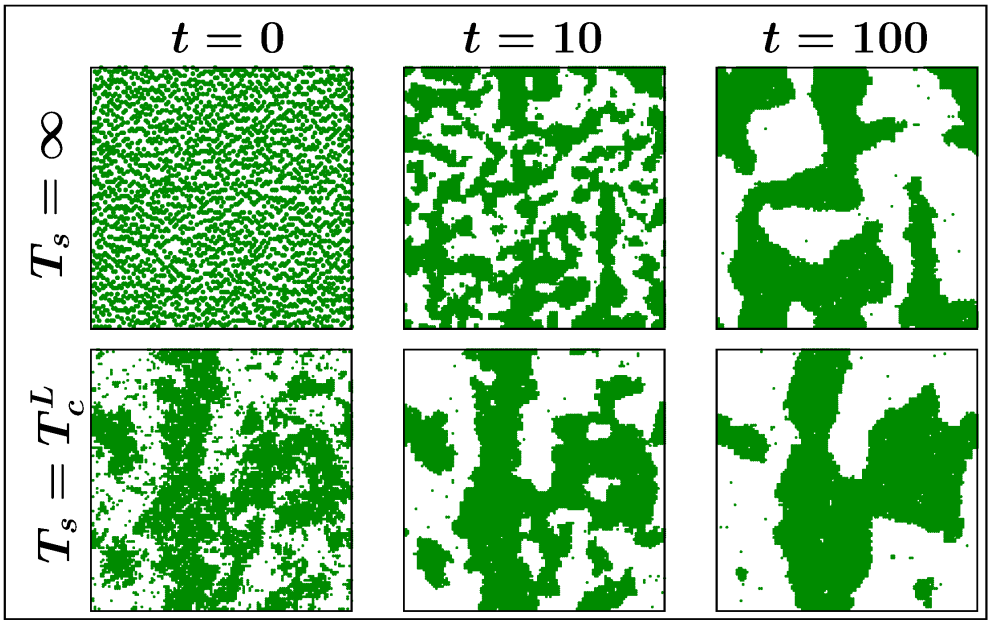

Figure 4.1: The evolution snapshots, recorded during the Monte Carlo simulations of the nonconserved Ising model in $d = 2$, are presented for quenches to $T_f = 0.6T_c$. In each of the cases pictures from three different times are shown. At the top of each of the frames we have mentioned the corresponding time. We have included snapshots for quenches from finite-size critical temperature as well as from $T_s = \infty$, with $L = 128$. In all the frames the down spins are left unmarked.

slowing down [42]. Here, instead of a single spin, a randomly selected cluster of similar spins is flipped.

The average domain lengths of a system during evolution have been calculated via [32, 43]

$$\ell(t) = \int P(\ell_d, t)\ell_d d\ell_d, \tag{4.11}$$

where $P(\ell_d, t)$ is a domain-size distribution function, and ℓ_d is the distance between two successive interfaces in a specific direction. In the calculation of the autocorrelation functions [see Eq. (4.3)], the order parameter ψ at a space point corresponds to the value of spin in Eq. (4.9) at a lattice site. All the presented results are averaged over a large number of independent initial configurations, ranging between 100 and 500, depending upon the system size. The value of L in $d = 3$ varies from 10 to 300, and in $d = 2$, it varies from 64 to 1024.

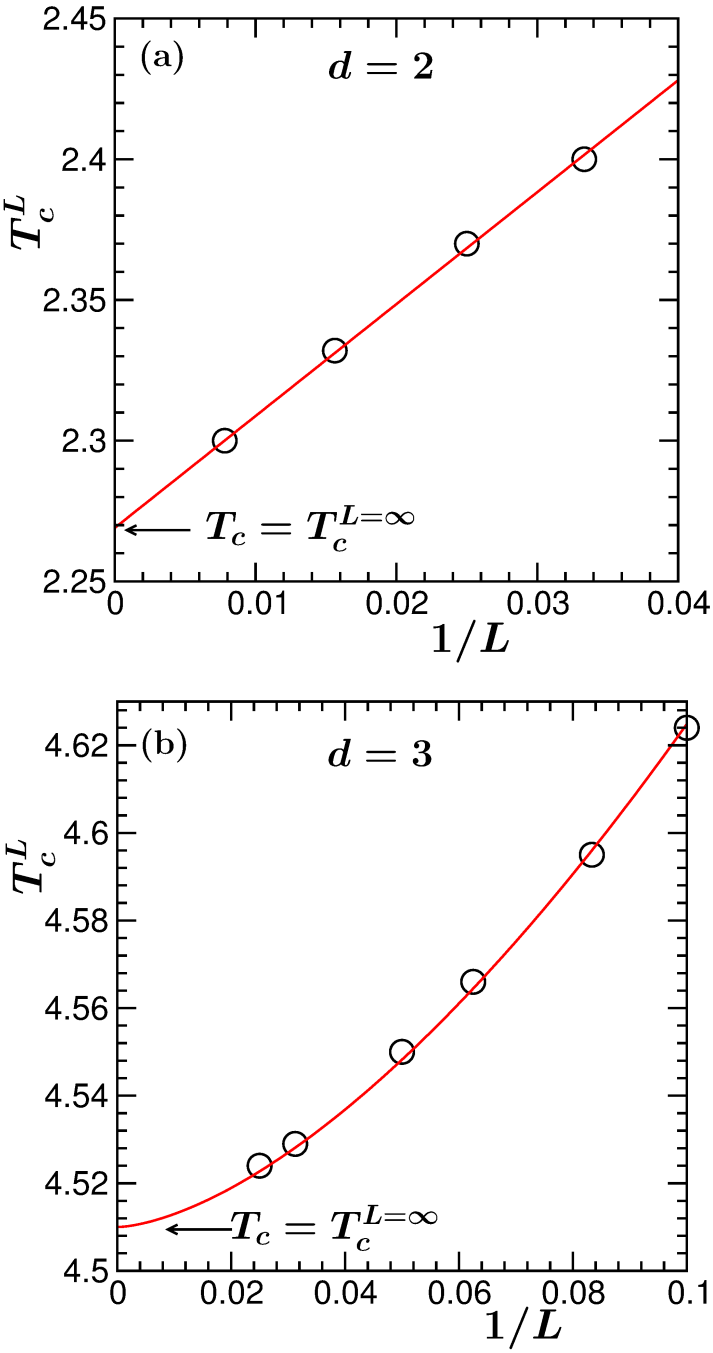

Figure 4.2: (a) Plot of finite-size critical temperatures T_c^L as a function of the inverse system size $1/L$. The continuous line is a fit of the data set to the scaling form in Eq. (4.13), by fixing T_c and ν to their 2D Ising values, i.e., $T_c = 2.269$ and $\nu = 1$. This figure is reproduced from Ref. [46] (Fig. 2). (b) Same as (a) but for $d = 3$. Here the value of ν is 0.63 and $T_c = 4.51$. This figure is reproduced from Ref. [49] (Fig. 1). Unless otherwise mentioned, all the results below will correspond to $T_s = T_c^L$.

4.3 Results

We start by presenting the evolution snapshots for different T_s values, $T_s = \infty$ and $T_s = T_c^L$, from $d = 2$. The upper frame corresponds to the case with $T_s = \infty$ and the lower frame corresponds to the case of $T_s = T_c^L$. All the pictures are from simulations with $L = 128$. The difference in structure in the two cases is recognizable, even though there exist strong finite-size effects in the initial configurations [30, 38] for $T_s = T_c^L$. The latter is in addition to the standard finite-size effects [31, 32, 43] that is observed for $T_s = \infty$, when ℓ approaches L. As is well known [25],

$$\xi \sim \epsilon^{-\nu};\ \epsilon = \frac{T_s - T_c}{T_c}, \tag{4.12}$$

ν being a static critical exponent. For a true phase transition, achievable in thermodynamically large systems, of course, $\xi = \infty$ at the critical point. However for $L < \infty$, which is always the case for computer simulations, ξ is finite, the maximum attainable value being $\xi = L$. Because of that, for finite L, when $T_s = T_c^L$, following quenches the systems quickly deviate from the desired [20, 21] scaling form, different from that for quenches with $T_s = \infty$, of the nonequilibrium structure. This can be realized by taking a closer look at the snapshots for $T_s = T_c^L$ in Fig. 4.1 – the fractality is changing with time. This additional finite-size effect must be taken care of via appropriate extrapolation of the size-affected quantitative data in the $L = \infty$ limit. This requires knowledge of T_c^L for various values of L. Related results we present next before showing data for the autocorrelation functions.

Phase behavior for a model can be obtained via computer simulations by calculating the temperature dependent, appropriately defined, order-parameter distribution functions [38, 40]. Such a phase diagram or coexistence curve will always suffer from finite-size effects due to the fact that, as mentioned above, in simulations we always have $L < \infty$. Nevertheless, via the applications of well-established scaling principles phase behavior, including the critical point, in the thermodynamic limit, can be satisfactorily obtained [40, 44, 45].

In the two-phase or coexistence region the order-parameter distribution will have a double peak structure, locations of the peaks representing points along the coexistence curve. On the other hand, in the homogeneous (one-phase) region these distributions will have single peak shape (with temperature dependent width). The temperature at which the crossover from double peak to single peak structure occurs is identified as the value of T_c^L. Plots of T_c^L versus $1/L$ in $d = 2$ and 3 are shown in Fig. 4.2 (a) and

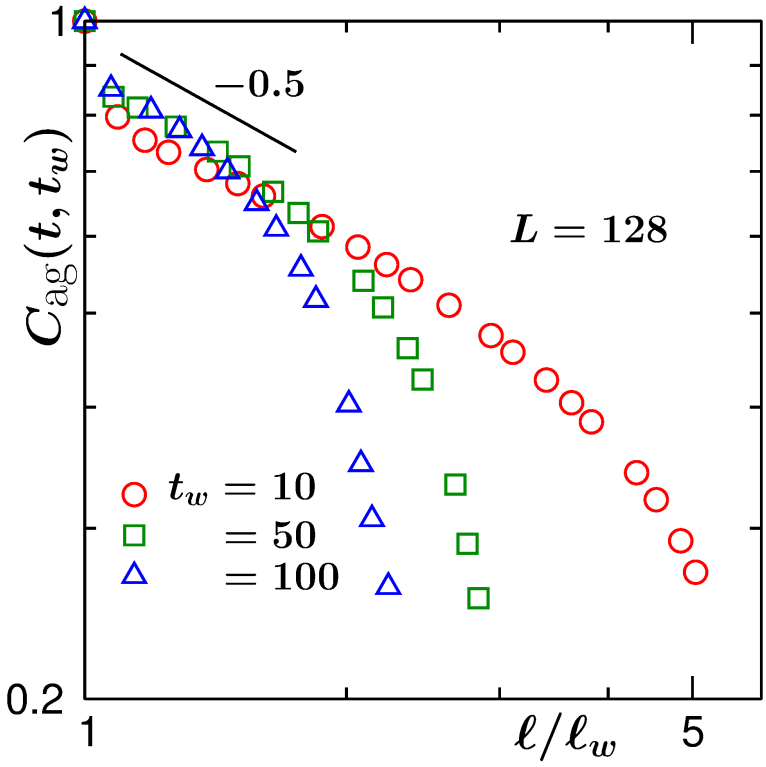

Figure 4.3: Log-log plots of the order-parameter autocorrelation function, $C_{\rm ag}(t, t_w)$, versus ℓ/ℓ_w, in $d = 3$. Data for a few different values of t_w are included. These results are for $L = 128$. The figure is reproduced from Ref. [49] [Fig. 4(a)].

(b), respectively. These results were obtained by discarding snapshots from early time non-equilibrium regime. Note that the results for T_c^L are expected to satisfy the scaling form [38, 40, 44, 45]

$$T_c^L - T_c \sim L^{-1/\nu}, \tag{4.13}$$

validity of which can be checked from its consistency with Eq. (4.12). For the Ising model (universality class) $\nu = 1$ in $d = 2$, and $\nu = 0.63$ in $d = 3$. The data sets in Fig. 4.2, thus, are in agreement with this expected critical point behavior. Note that the continuous lines in Fig. 4.2 are fits of the simulation data sets to the scaling form in Eq. (4.13), by fixing ν and T_c to the 2D and 3D Ising values. We use the amplitude ($\simeq 3.9$ in $d = 2$ and $\simeq 4.4$ in $d = 3$) obtained from the fits to extract T_c^L for L larger than the presented ones.

Following the discussion and presentation of results relevant for the scaling analysis of the aging data for the critical starting point, we now focus on the primary objective. In Fig. 4.3 we present results for $C_{\rm ag}(t, t_w)$, versus ℓ/ℓ_w, for $d = 3$, by fixing the system size, for few different values of t_w. The observations are the following.

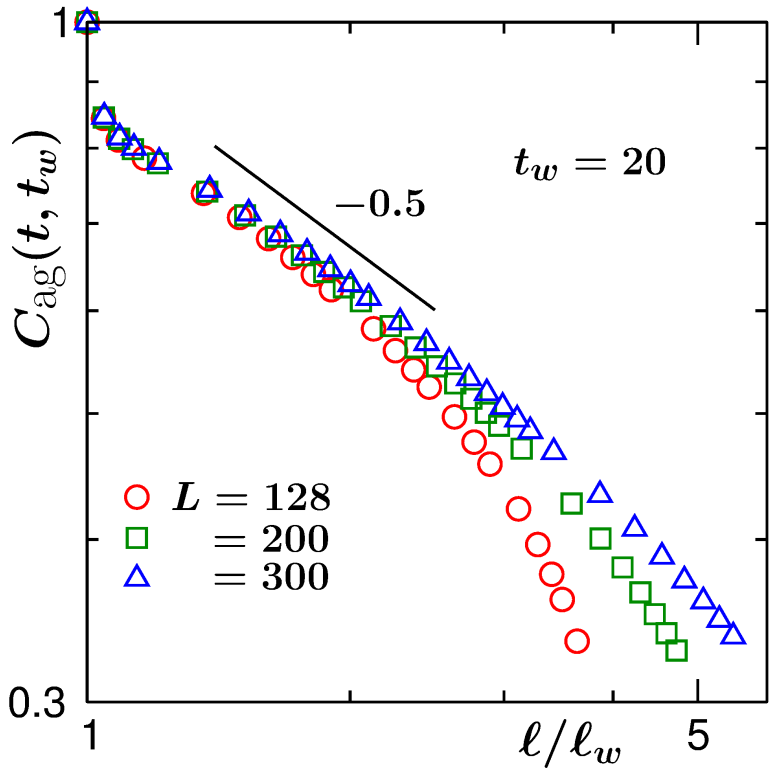

Figure 4.4: Plots of $C_{\rm ag}(t, t_w)$ versus ℓ/ℓ_w, on a log-log scale, from three different system sizes, L, in $d = 3$. The value of t_w is fixed to 20 here. The solid line corresponds to a power-law decay with an exponent mentioned near it.

There exist sharp departures of the data sets from each other at large ℓ/ℓ_w. Higher the value of t_w the departure occurs earlier from the plot for a smaller t_w. This is related to 'standard' nonequilibrium finite-size effects [14, 15]. With the increase of t_w a system has less effective size available to grow or age for. Furthermore, even in the small ℓ/ℓ_w region the collapse of the data set for $t_w = 10$ with those for the larger t_w values is rather poor. This, we believe, is due to the fact that in the scaling regime the structure is different [33] from the initial configuration [46]. (Also note that the scaling structure for $T_s = T_c$ is different from that for $T_s = \infty$.) During this switch-over to the scaling behavior the extraction of ℓ is also ambiguous, due to continuous change in the structure that, thus, lacks the property of Eq. (4.2). If we believe that by $t_w = 50$ the scaling regime has arrived (see the reasonably good collapse of data sets for $t_w = 50$ and 100 in the small ℓ/ℓ_w regime), the corresponding decay is consistent with $\lambda = 0.5$, a value that was predicted theoretically [21]. Nevertheless, given the complexity of finite-size and other effects, further analysis is required, before arriving at a conclusion with confidence.

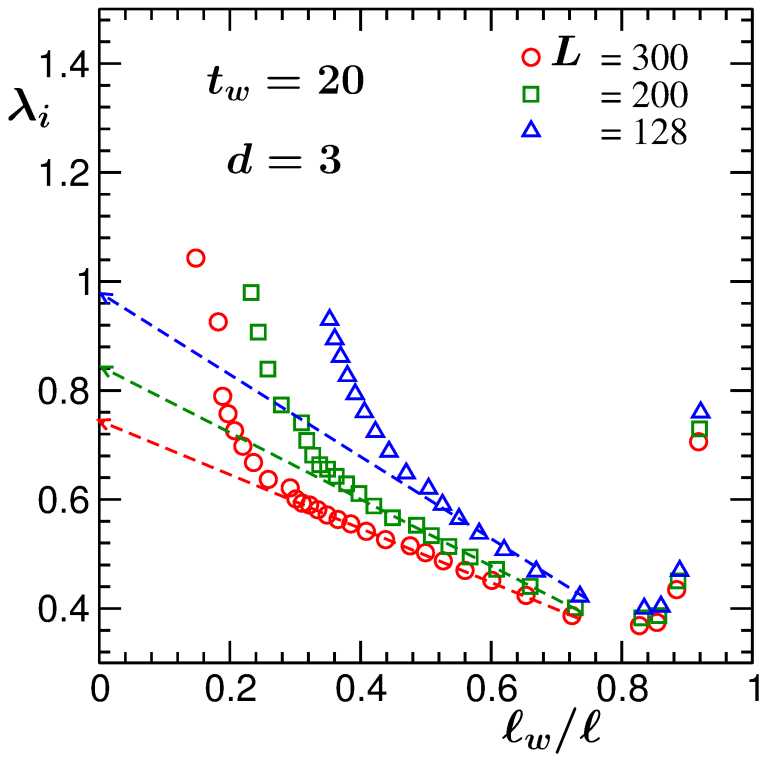

Figure 4.5: Instantaneous exponents λ_i are plotted versus ℓ_w/ℓ, for three values of L, in $d = 3$. In each of the cases we have $t_w = 20$. We extract L-dependent value, λ_L, from the extrapolation of linear region to the y-axis.

Here one may also get an impression that the exponent λ has a tendency to increase with the increase in t_w values. To check for the convergence to the scaling regime, we require more systematic study involving both t_w and L. We will perform this in the rest of the chapter.

In Fig. 4.4, we present the data for $C_{\rm ag}(t, t_w)$, as a function of ℓ/ℓ_w, from three different system sizes, in $d = 3$. The results are for $t_w = 20$. From this figure, it can be seen that for a fixed t_w, with the increase of system size the exponents keep staying stable for longer ranges. Also, the rate of change of the exponent with the increase of L keeps decreasing. That way one may like to consider a very large system to obtain λ value that will be very close to that for $L = \infty$. We, however, would like to rely on an extrapolation method using relatively smaller systems. Note that faster decay of the autocorrelation for large ℓ/ℓ_w is unavoidable, because of the finite value of ξ when $L < \infty$. Only in the $L = \infty$ limit, $C_{\rm ag}(t, t_w)$ will decay indefinitely with unique exponent. We mention here: an advantage of using smaller systems is that one can get better statistics by running simulations with many independent initial configurations, using the same computational

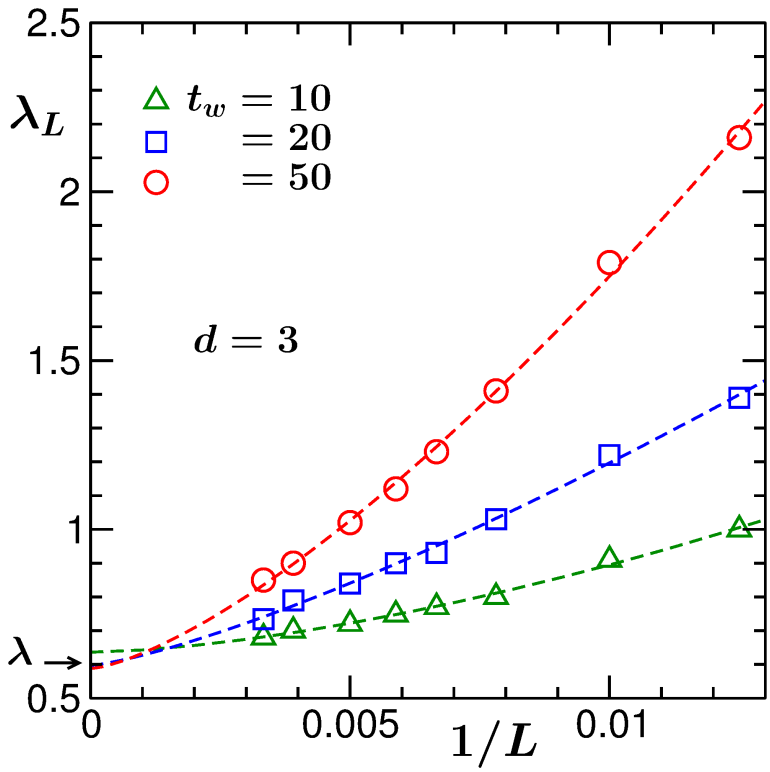

Figure 4.6: Plots of λ_L as a function of $1/L$. Data from a few different values of t_w are shown. The dashed lines are power-law fits to the simulation data sets. The arrow-headed horizontal line marks the estimated value of λ. All results are from $d = 3$. This plot is taken from Ref. [49] [Fig. 6(b)].

power that is needed to run single large system. Here note that reduction of error is not directly proportional to the size of a system [31, 43].

For the purpose of extrapolation, we need to obtain the exponent values in the stabilized regions accurately. For this we take help of the instantaneous exponent [15, 47, 48]

$$\lambda_i = -\frac{d \ln C_{\rm ag}(t, t_w)}{d \ln x}; \; x = \frac{\ell}{\ell_w}. \tag{4.14}$$

In Fig. 4.5, as illustration, we plot this quantity as a function of $1/x$, in $d = 3$, for three values of L, by fixing t_w to 20. The L dependent exponent, λ_L, we obtain from the extrapolation of the linear region to $\ell_w/\ell \to 0$ (i.e., $\ell \to \infty$) limit, from the plots. We expect that λ_L in the limit $L = \infty$ will have same convergence for all values of t_w, because of the following reasons. For the meaningful scaling evolution, in the $L = \infty$ limit the structure should obey certain self-similarity all along [20, 21]. If so, the value of λ should not be affected by the choice of t_w. Note that in such a situation the bound of

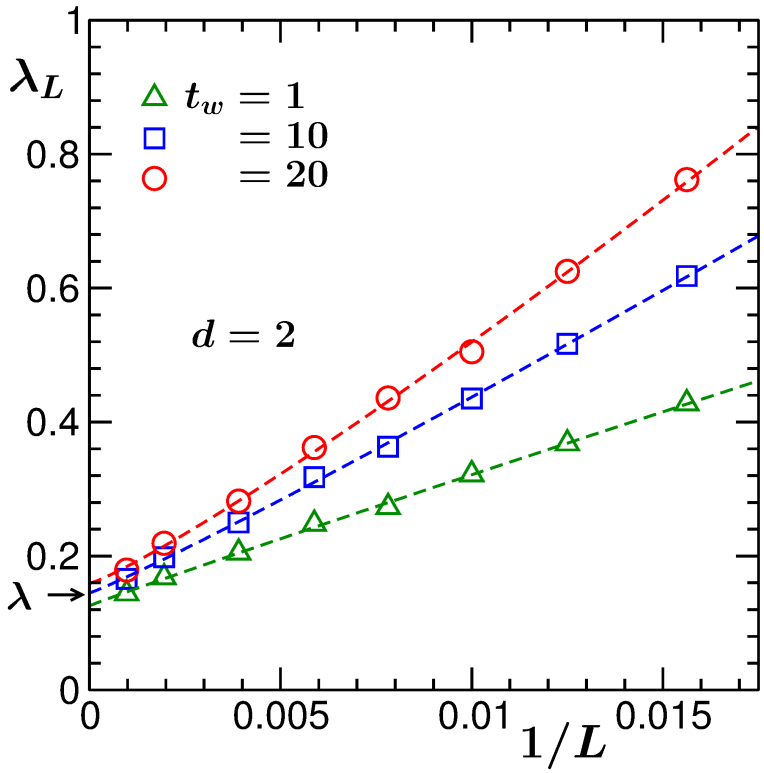

Figure 4.7: Same as Fig. 4.6 but here it is for $d = 2$. This figure is taken from Ref. [49] [Fig. 7(b)].

Eq. (4.7) does not change. For finite L, of course, the situation is different, as discussed and being observed. However, the intended extrapolation is expected to lead us to the thermodynamic λ, same for all t_w. If this is the case and the corresponding λ is different from that of $T_s = \infty$ it gives an indirect evidence that there exist different structural scalings for $T_s = \infty$ and $T_s = T_c$. We followed the similar procedure for $d = 2$ as well. In both the cases, we have performed this exercise for multiple values of t_w.

Data for λ_L, when plotted versus $1/L$, for multiple values of t_w, should provide a good sense of convergence [46, 49]. Corresponding number should be the value of λ for a thermodynamically large system. This exercise has been shown in Fig. 4.6 for $d = 3$, and in Fig. 4.7 for $d = 2$. The dashed lines there are fits to the form

$$\lambda_L = \lambda + AL^{-b}, \tag{4.15}$$

where A and b are constants. For both the dimensions, fits to each of the data sets provide λ value quite consistent with each other. The obtained values of λ, along with those for uncorrelated initial configurations [8, 14, 15], are quoted in Table 4.1. Here

the corresponding values of λ for $T_s = \infty$ and $T_s = T_c$ in the case of conserved order parameter dynamics are also included. These values are taken from references [46] and [49] for the comparison, which were obtained from the Kawasaki exchange Ising model (KIM) [50].

Table 4.1: List of values of λ for the nearest neighbor Ising model. This is reproduced from Ref. [49] (Table I).

Model	$d = 2$		$d = 3$	
	Correlated	Uncorrelated	Correlated	Uncorrelated
GIM	0.14 ± 0.02	1.32 ± 0.04	0.57 ± 0.07	1.69 ± 0.04
KIM	0.13 ± 0.02	3.6 ± 0.2	0.64 ± 0.05	7.5 ± 0.4

From the table it is clearly seen that the values of λ for $T_s = \infty$ and $T_s = T_c$ universality classes are vastly different. The results for the nonconserved model are certainly in extremely good agreement with the theoretical prediction [20, 21], viz., $\lambda = 0.125$ in $d = 2$ and $\lambda = 0.5$ in $d = 3$. Also, for $T_s = T_c$, GIM and KIM results are close to each other. We mention here that in the previous simulation studies [19–21] no such attempts have been made to estimate λ for $T_s = T_c$. Only checks for the consistency with the analytical theory were performed.

Table 4.2: List of β values for the nearest neighbor Ising model. Validity of YRD bound can be checked by putting these numbers in Eq. (4.7) and comparing with the results quoted in Table 4.1. While preparing this table η in $d = 3$ has been set to zero (see discussion in the context of Fig. 4.8). We have put the values of the bounds [9] inside the parentheses. This table is taken from Ref. [49] (Table II).

Model	$d = 2$		$d = 3$	
	Correlated	Uncorrelated	Correlated	Uncorrelated
GIM	-1.75 (0.125)	0 (1)	-2 (0.5)	0 (1.5)
KIM	-1.75 (0.125)	4 (3)	-2 (0.5)	4 (3.5)

Next we aim at checking whether these numbers satisfy the YRD bound. The behavior of the equal time structure factor in $d = 3$, for a thermodynamically large system, at criticality is expected to be [25, 38, 51]

$$S(k, 0) \sim k^{-2}, \tag{4.16}$$

given that in $d = 3$ the critical exponent η ($\simeq 0.036$, as opposed to 0.25 in $d = 2$), the Fisher exponent that characterizes the power-law factor of the critical correlation as

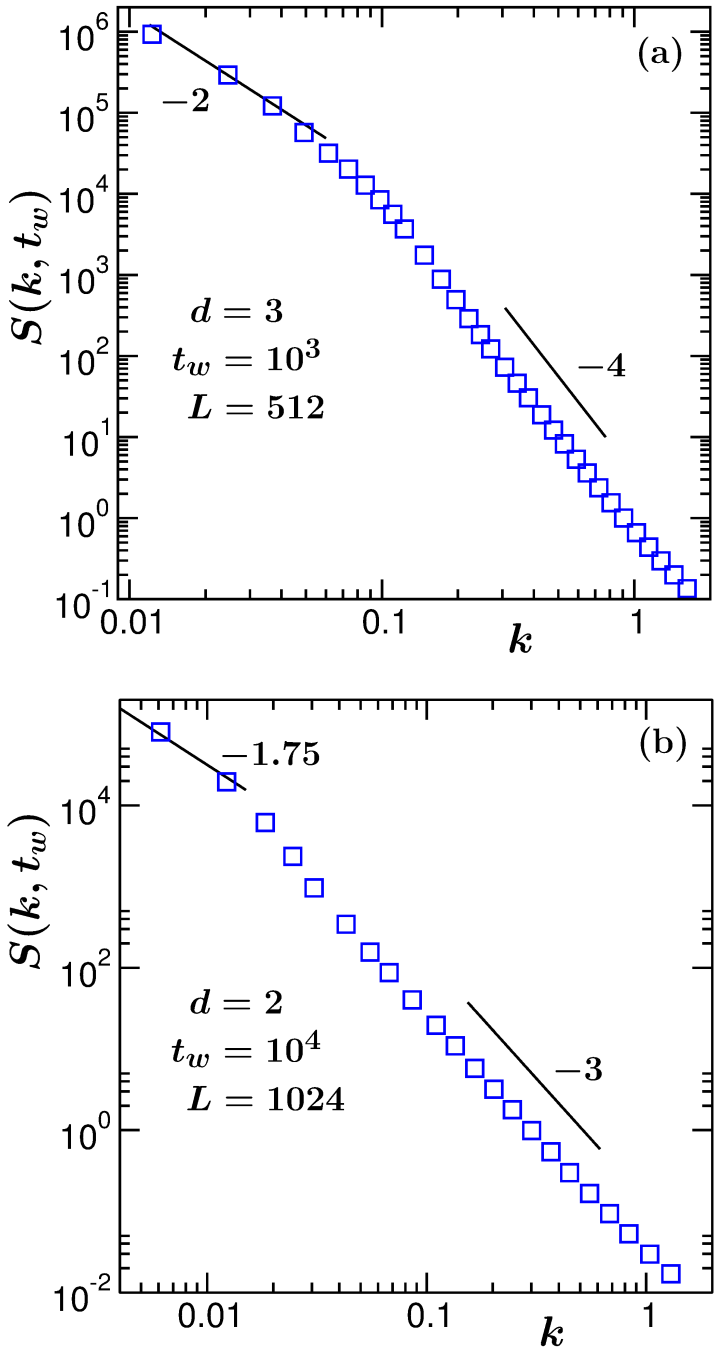

Figure 4.8: (a) Log-log plots of structure factor versus wave vector, from $d = 3$. (b) Same as (a) but here we show the results for $d = 2$. The solid lines are power-laws with exponent values noted in the figure. The values of t_w and L are also mentioned. These figures are reproduced from Ref. [49] (Fig. 3).

$r^{d-2+\eta}$, has a small value. Typically, in most of the coarsening systems scaling in the decay of autocorrelation function [cf. Eq. (4.4)] starts from a reasonably large value of t_w. By then the structure is expected to have changed from that at the beginning. Thus, the exponent '-2' in Eq. (4.16) should be verified before being taken as the value of β in the YRD bound for the understanding of results following quenches from T_c. Furthermore, for $T_s = T_c$, one may even ask about the validity of a stable β. This is related to the question whether there exists a scaling regime or the structure is continuously changing. Keeping this in mind, in Fig. 4.8 we present plots of $S(k, t_w)$ versus k for large enough values of L and t_w, from $d = 3$ in part (a). In fact β appears to be stable at '-2' even though the character of structure changes at large k, e.g., an appearance of the Porod law [2] ($S(k) \sim k^{-4}$) is clearly visible that corresponds to the existence of domain boundaries. Results from $d = 2$ is presented in part (b). Here also the small k behavior remains unaltered from that in the initial configuration, i.e., we have [25] $\beta = -7/4$. In this dimension the Porod law [2] demands $S(k) \sim k^{-3}$.

For the comparison of λ values obtained and the YRD bound, we have quoted the values of β in Table 4.2. Here also the values of β corresponding to the conserved order parameter dynamics [46, 49] are included.

It appears that the bounds are satisfied for $T_s = T_c^L$ also. From the values of β, it is clear that the corresponding YRD bound for λ is below the values obtained from the simulation, i.e., $\lambda \simeq 0.14$ and $\lambda \simeq 0.57$, in $d = 2$ and 3, respectively.

4.4 Conclusion

We have presented results for aging phenomena in the nearest neighbor Ising model [25] in $d = 2$ and 3. The results were obtained from Monte Carlo simulations [37–39] with the implementation of Glauber dynamics. Our objective was to estimate the aging exponent λ, related to the power-law decay of the order-parameter autocorrelation function [7] $C_{\rm ag}(t, t_w)$, corresponding to the universality class [20, 21] decided by quenches from $T_s = T_c$, for which one has infinitely correlated configurations [25].

For quenches from the critical point, simulation results suffer significantly from finite-size effects. This problem was appropriately taken care of by implementing finite-size scaling technique of equilibrium critical phenomena and devising an extrapolation method for analysis of the out-of-equilibrium data. We believe that our results are quite accurate for thermodynamically large systems.

It appears that the values of λ for $T_s = T_c$ are drastically smaller than those for the universality class corresponding [8, 14, 15] to $T_s = \infty$ in both the dimensions. Our simulation results are also in reasonable agreement with an analytical prediction [21]. The source of deviations that exist may have its origin in the estimation error for T_c^L as well as in the statistical error in nonequilibrium simulations. Nevertheless, the obtained values for $T_s = T_c$ satisfy the lower bounds predicted by Yeung, Rao and Desai [9]. This we have checked via the analysis of structure, a property that is embedded in the construction of the bound.

Overall it also appears that there exists strong qualitative similarity between cases with conserved and nonconserved dynamics, as far as the universalities with respect to quenches from correlated and decorrelated initial configurations are concerned. Even though for quenches with $\xi = 0$ the values of λ differ significantly in the two cases, for quenches from the critical point, i.e., for $\xi = \infty$, the exponents are practically same in both the dimensions.

This work, combined with a few others [14, 15, 21, 26–28, 46], provides near-complete information on the universality in coarsening dynamics in the Ising model, involving "realistic" space dimensions, conservation property of the order parameter, and spatial correlations in the initial configurations. Analogous studies in other systems should be done, by employing the methods used here, to obtain a complete understanding, e.g., the influences of hydrodynamics on relaxation in out-of-equilibrium systems with long range initial correlations.

Copyright and Permission

The results of this chapter have been published in:
1) Subir K. Das, Koyel Das, **Nalina Vadakkayil**, Saikat Chakraborty, and Subhajit Paul, "Initial correlation dependence of aging in phase separating solid binary mixtures and ordering ferromagnets", J. Phys.: Condens. Matter **32**, 184005 (2020).
©IOP Publishing. Reproduced with permission. All rights reserved.
See the publication link below:
https://iopscience.iop.org/article/10.1088/1361-648X/ab6d10/meta

2) Koyel Das, **Nalina Vadakkayil**, and Subir K. Das, Phys. Rev. E **101**, 062112 (2020).
We have reproduced the materials here following Copyright Policy of American Physical Society, the publisher of the article. See the publication link below:
https://journals.aps.org/pre/abstract/10.1103/PhysRevE.101.062112

In each of the figure captions we have cited the appropriate source. The text for results from $d = 2$ have been borrowed from publication 1) above. The text for the discussion of results from $d = 3$ have been borrowed from publication 2).

References

[1] K. Binder, in *Phase Transformation of Materials*, edited by R.W. Cahn, P. Haasen, and E.J. Kramer (Wiley VCH, Weinheim, 1991), Vol. 5. p. 405.

[2] A.J. Bray, Adv. Phys. **51**, 481 (2002).

[3] A. Onuki, *Phase Transition Dynamics* (Cambridge University Press, Cambridge, UK, 2002).

[4] R.A.L. Jones, *Soft Condensed Matter* (Oxford University Press, Oxford, UK, 2002).

[5] J.D. Gunton, R. Toral, and A. Chakrabarti, Physica Scripta. **T33**, 12 (1990).

[6] M. Zannetti, in *Kinetics of Phase Transitions*, edited by S. Puri and V. Wadhawan (CRC Press, Boca Raton, 2009).

[7] D.S. Fisher and D.A. Huse, Phys. Rev. B **38**, 373 (1988).

[8] F. Liu and G.F. Mazenko, Phys. Rev. B **44**, 9185 (1991).

[9] C. Yeung, M. Rao, and R.C. Desai, Phys. Rev. E **53**, 3073 (1996).

[10] M. Henkel, A. Picone, and M. Pleimling, Europhys. Lett. **68**, 191 (2004).

[11] C. Yeung and D. Jashnow, Phys. Rev. B **42**, 10523 (1990).

[12] F. Corberi, E. Lippiello, and M. Zannetti, Phys. Rev. E **74**, 041106 (2006).

[13] E. Lorenz and W. Janke, Europhys. Lett. **77**, 10003 (2007).

[14] J. Midya, S. Majumder, and S.K. Das, J. Phys.: Condens. Matter **26**, 452202 (2014).

[15] J. Midya, S. Majumder, and S.K. Das, Phys. Rev. E **92**, 022124 (2015).

[16] N. Vadakkayil, S. Chakraborty, and S.K. Das, J. Chem. Phys. **150**, 054702 (2019).

[17] S. Paul and S.K. Das, Phys. Rev. E **96**, 012105 (2017).

[18] S. Roy, A. Bera, S. Majumder, and S.K. Das, Soft Matter **15**, 4743 (2019).

[19] F. Corberi and R. Villavicencio-Sanchez, Phys. Rev. E **93**, 052105 (2016).

[20] K. Humayun and A.J. Bray, J. Phys. A: Math. Gen. **24**, 1915 (1991).

[21] A.J. Bray, K. Humayun, and T.J. Newman, Phys. Rev. B **43**, 3699 (1991).

[22] S.B. Dutta, J. Phys. A: Math. Theor. **41**, 395002 (2008).

[23] S. Puri and D. Kumar, Phys. Rev. Lett. **93**, 025701 (2004).

[24] A.J. Bray, S.N. Majumdar, and G. Schehr, Adv. Phys. **62**, 225 (2013).

[25] M.E. Fisher, Rep. Prog. Phys. **30**, 615 (1967).

[26] S. Chakraborty and S.K. Das, Eur. Phys. J. B **88**, 160 (2015).

[27] S. Chakraborty and S.K. Das, Phys. Rev. E **93**, 032139 (2016).

[28] T. Blanchard, L.F. Cugliandolo, and M. Picco, J. Stat. Mech.: Theor. Expt. P12021 (2014).

[29] S.M. Allen and J.W. Cahn, Acta Metall. **27**, 1085 (1979).

[30] M.E. Fisher and M.N. Barber, Phys. Rev. Lett. **28**, 1516 (1972).

[31] D.W. Heermann, L. Yixue, and K. Binder, Physica A **230**, 132 (1996).

[32] S. Majumder and S.K. Das, Phys. Rev. E **84**, 021110 (2011).

[33] C. Yeung, Phys. Rev. Lett. **61**, 1135 (1988).

[34] H. Furukawa, Phys. Rev. B **40**, 2341 (1989).

[35] S.N. Majumdar, D.A. Huse, and B.D. Lubachevsky, Phys. Rev. Lett. **73**, 182 (1994).

[36] R.J. Glauber, J. Math. Phys. **4**, 294 (1963).

[37] K. Binder and D.W. Heermann, *Monte Carlo Simulations in Statistical Physics* (Springer, Switzerland, 2019).

[38] D.P. Landau and K. Binder, *A Guide to Monte Carlo Simulations in Statistical Physics* (Cambridge University Press, Cambridge, 2009).

[39] D. Frenkel and B. Smit, *Understanding Molecular Simulations: From Algorithms to Applications* (Academic Press, San Diego, 2002).

[40] E. Luijiten, M.E. Fisher, and A.Z. Panagiotopoulos, Phys. Rev. Lett. **88**, 185701 (2002).

[41] U. Wolff, Phys. Rev. Lett. **62**, 361 (1989).

[42] P.C. Hohenberg and B.I. Halperin, Rev. Mod. Phys. **49**, 435 (1977).

[43] S. Majumder and S.K. Das, Phys. Rev. E **81**, 050102 (2010).

[44] S. Roy and S.K. Das, Europhys. Lett. **94**, 36001 (2011).

[45] J. Midya and S.K. Das, J. Chem. Phys. **146**, 044503 (2017).

[46] S.K. Das, K. Das, N. Vadakkayil, S. Chakraborty, and S. Paul, J. Phys.: Condens. Matter **32**, 184005 (2020).

[47] J.G. Amar, F.E. Sullivan, and R.D. Mountain, Phys. Rev. B **37**, 196 (1988).

[48] D.A. Huse, Phys. Rev. B **34**, 7845 (1986).

[49] K. Das, N. Vadakkayil, and S.K. Das, Phys. Rev. E **101**, 062112 (2020).

[50] K. Kawasaki, in *Phase Transition and Critical Phenomena*, edited by C. Domb and M.S. Green (Academic, New York, 1972), Vol. 2, p. 443.

[51] M. Plischke and B. Bergersen, *Equilibrium Statistical Physics* (World Scientific, London, 2005).

Chapter 5

Should a Hotter Paramagnet Transform Quicker to a Ferromagnet? Monte Carlo Simulation Results for Ising Model

5.1 Introduction

When quenched to the same lower temperature T_f, should a hotter system equilibrate faster than a colder one? An answer in affirmative is counter-intuitive and relates to the Mpemba effect (ME) [1, 2]. ME can have important applications in memory devices [3] and elsewhere. In spite of such practical importance and the knowledge since the time of Aristotle [2, 4–8], explanation of ME remains elusive. Following the work [1] by Mpemba and Osborne, there has been a surge of interest in understanding it [2, 3, 9–20], particularly during the last decade [3, 10–20]. Nevertheless, the progress remains limited. Interestingly, there still exists hot debate on the very existence of the effect. Experimental reports are available in favor of [9, 10, 18, 19, 21] as well as against [20, 21] it.

Historically the effect has been attached with cooling or solidification of liquids [4–7, 22, 23], like water and milk. Recently there exist efforts to extend the domain by asking the same question for other systems [3, 12–19]. These include cooling granular gases [14], coarsening spin glasses [3], etc. In the case of spin glasses [3, 24–26], ME is observed due to the variation of the correlation length (ξ) with the shifting of the

starting temperature T_s. Likewise, in each type of systems [3, 12–19] certain anomaly decides on the existence of ME. Some of the studies [3, 14] provide the impression that the effect has connection with aging systems [27–29]. However, it is not clear whether the connection is only with the aging systems having glass-like slow dynamics [3, 24–26] or simpler aging systems, undergoing standard clustering or phase transitions [30, 31], are also good candidates for the exhibition of the effect.

With the variation of T_s it is expected that certain structural quantities will undergo change. In the context of critical phenomena [31, 32], ξ exhibits the divergence [32]:

$$\xi \sim |T_s - T_c|^{-\nu}, \tag{5.1}$$

as T_s approaches T_c, the critical temperature. If variation in quantities associated with structure is responsible for the observation of ME, choice of a thermodynamic region close to T_c is then ideal [3, 33, 34] for preparing the systems before quenching to a T_f. Furthermore, to establish the reasons behind the effect, in addition to studies of systems having glass-like ingredients, materials of other varieties should also be considered. It is important to study simpler prototype systems. If the effect is observed, such systems can provide easier path to understanding, thereby putting the criticisms on the existence of ME to rest.

In this work we consider the standard nearest neighbor *ferromagnetic* Ising model [30–32]. We explore a wide range of T_s, lying above T_c. It is convincingly shown that following quenches to a T_f, below T_c, decay of energy for systems with higher T_s occurs faster. This, indeed, is the expectation [3] when ME is present. Our finding, which we confirmed via various means, is striking, given that, unlike the spin glasses, there is no in-built frustrated interaction in this model. Observation of ME in such a simple system hints that the effect is rather common. Furthermore, we provide a quantitative critical scaling picture to elucidate the outcome of the study.

5.2 Model and Methods

Model and methods are similar to those described in the previous chapters. Nevertheless, for the sake of completeness we briefly restate here.

The Hamiltonian of the model is [30–32]

$$H = -J \sum_{\langle ij \rangle} S_i S_j,\ S_i = \pm 1, \tag{5.2}$$

where $J\,(>0)$ is the interaction strength between nearest neighbors. The spin values ± 1 correspond to up and down orientations of the atomic magnets. We study this model via Monte Carlo (MC) simulations [35–37], in space dimension $d = 2$, on a square lattice. The value of T_c for this system [35] is $= 2.269185...J/k_B$, where k_B is the Boltzmann constant.

Following quenches to a T_f, the MC simulations were performed by employing the Glauber dynamics [35, 38]. In this method a trial move is performed by flipping a randomly chosen spin. This does not conserve [30] the system-integrated order parameter and the dynamics corresponds to ordering in a uniaxial ferromagnet. L^2 such moves, L being the linear dimension of a square simulation box, in units of the lattice constant a, make a single MC step (MCS). This is the unit of our time (t).

In the vicinity of T_c, the divergence in the relaxation time makes the preparation of initial configurations time taking. To avoid this, we used the Wolff algorithm [39], where, instead of a single spin flip, a randomly selected cluster is flipped. Initial configurations prepared at different values of T_s, via this method, are quenched to several values of T_f.

We have applied periodic boundary conditions in both directions. Unless otherwise mentioned, presented results are averaged over 100000 independent initial configurations. All results are for $L = 256a$. In the following we set, for the sake of convenience, J, k_B and a to unity.

5.3 Results

In Figs. 5.1(a) and (b) we show typical equilibrium snapshots from two values of T_s, each having critical, i.e., 50:50 proportion of up and down spins. The difference in the extent of spatial correlations between the two temperatures is easily identifiable from these pictures. Such critical enhancements [32] are demonstrated quantitatively in Fig. 5.2 and Fig. 5.3. In Fig. 5.2 we show the probability distributions for order-parameter (m) fluctuation [36, 40]. The width is much higher for the temperature that is closer to T_c, implying enhanced susceptibility [32, 36, 40].

In Fig. 5.3(a) we have presented the structure function [32], $S(k)$, versus k, the latter being the wave number, for the same two temperatures. This structure function is related to the spatial fluctuation in the concentration field when the overall composition is fixed at the critical value [40–42]. In the $k \to 0$ limit, stronger enhancement in $S(k)$, for T_s closer to T_c, is again related to higher susceptibility. In part (b) of Fig. 5.3 we show $1/S(k)$ as a function of k^2, in a small k regime. Linear appearances are consistent

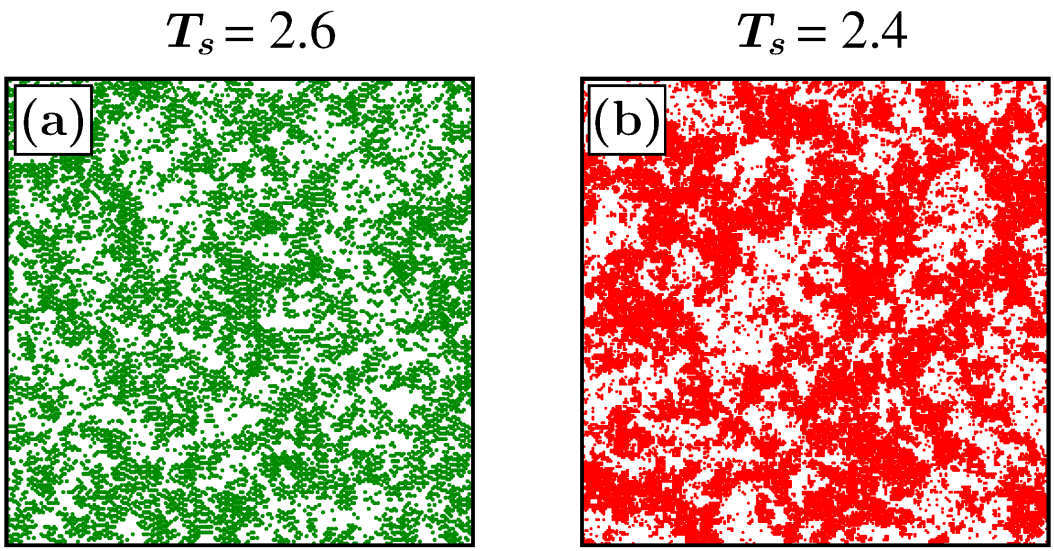

Figure 5.1: (a)-(b) Typical equilibrium configurations are shown from two starting temperatures, T_s. Each of the configurations has 50:50 proportion of up and down spins. The locations of the up spins are marked.

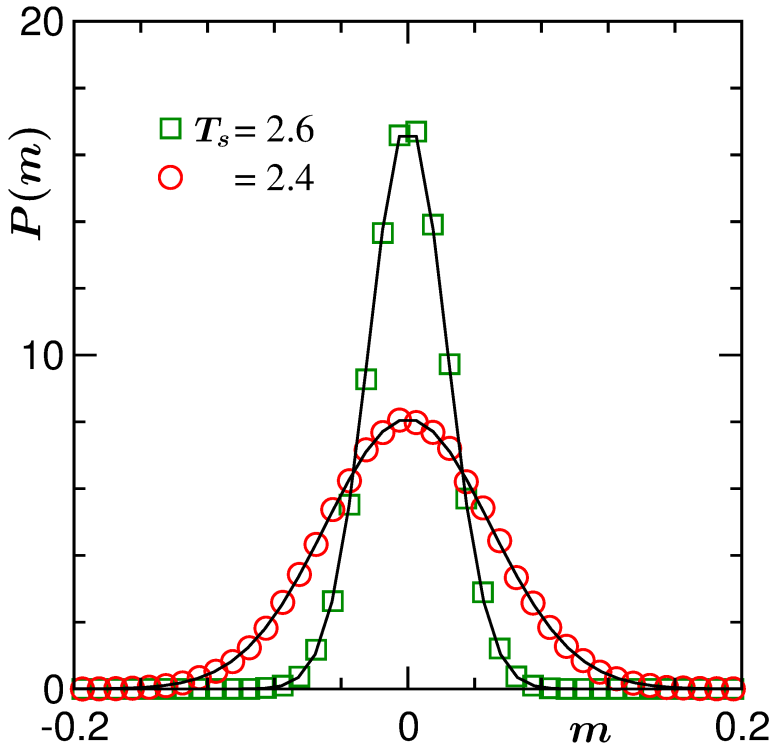

Figure 5.2: Plots of equilibrium probability distributions for magnetisation are shown from the T_s values for which the snapshots are presented in Fig. 5.1. These results were obtained by exploiting the composition fluctuations in the simulations via the Wolff algorithm. The continuous lines are Gaussian fits.

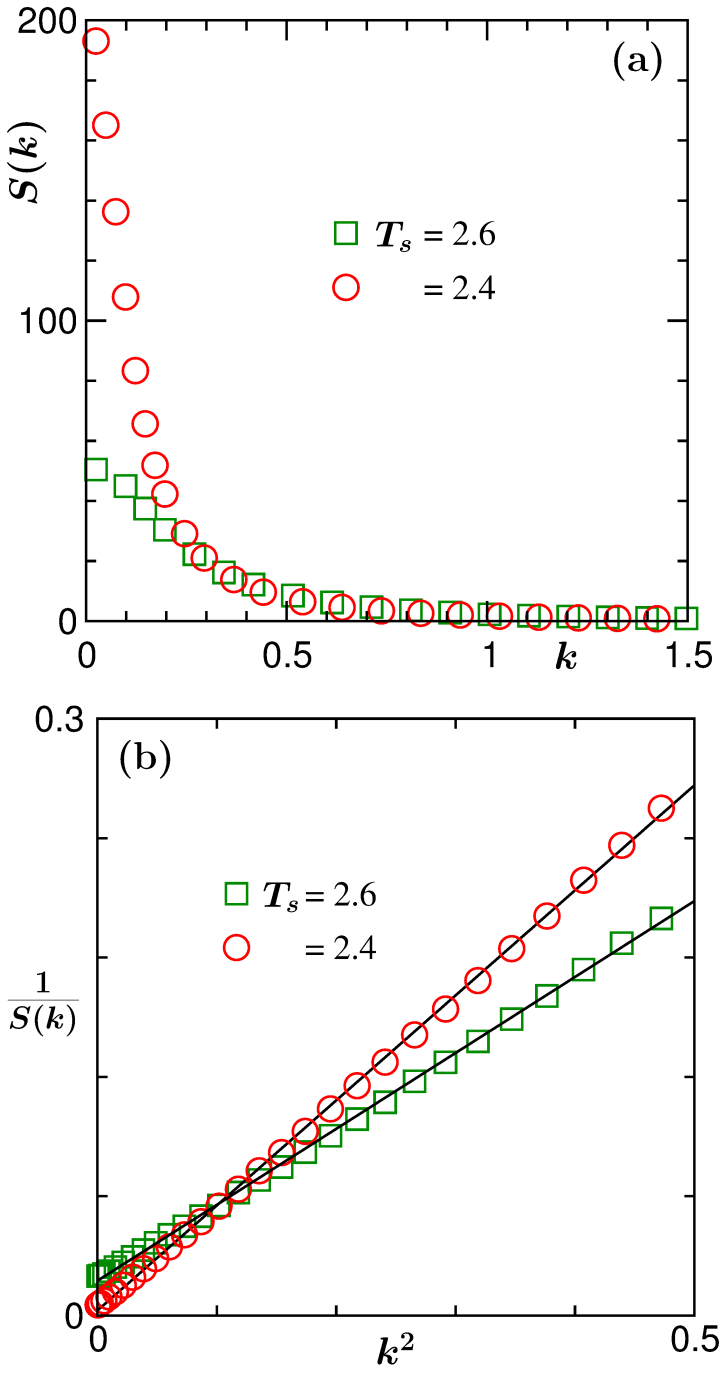

Figure 5.3: (a) $S(k)$, the structure factor, is plotted versus the wave number k, for 50:50 equilibrium configurations. These results are also presented from the same two T_s values mentioned in Fig. 5.1. (b) Plots of $1/S(k)$ versus k^2. Here the continuous lines represent linear behavior.

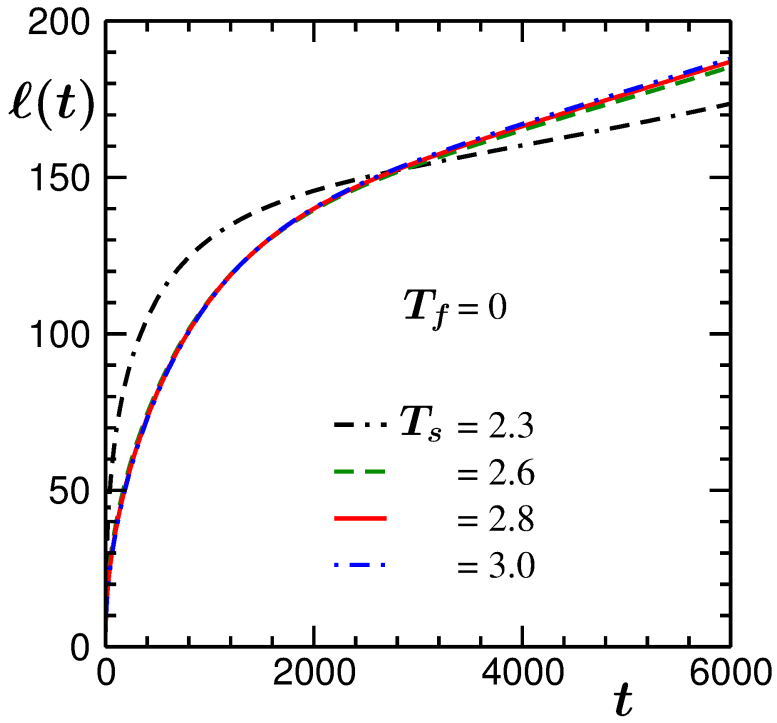

Figure 5.4: Average domain lengths, following quenches to $T_f = 0$, from different values of T_s, are plotted versus time.

with the Ornstein-Zernike [32, 41] behavior. Steeper slope for smaller T_s signifies an enhancement [32, 42] in ξ with the approach to T_c. With such temperature dependent initial configurations, we study the *equilibration* dynamics following quenches to various T_f below T_c.

In Fig. 5.4 we present plots for the growth of average domain length (ℓ), following quenches of initial configurations prepared at different values of T_s. In each of these cases the value of T_f was set at zero. These lengths were calculated from the first moment of the domain size distribution function [43], size of *a domain* being estimated as the distance between two successive interfaces, while scanning along different Cartesian directions. It is clearly seen in Fig. 5.4 that there exist crossings among curves and for a lower value of T_s the late time average domain lengths are smaller than those for a higher T_s. This suggests that the systems starting from higher T_s are relaxing faster.

A requirement for the validity of the above discussed picture, on the growths of lengths, is the existence of the self-similar property among the evolving domains [30], for different T_s, at any given instant of time within the relevant period. This feature

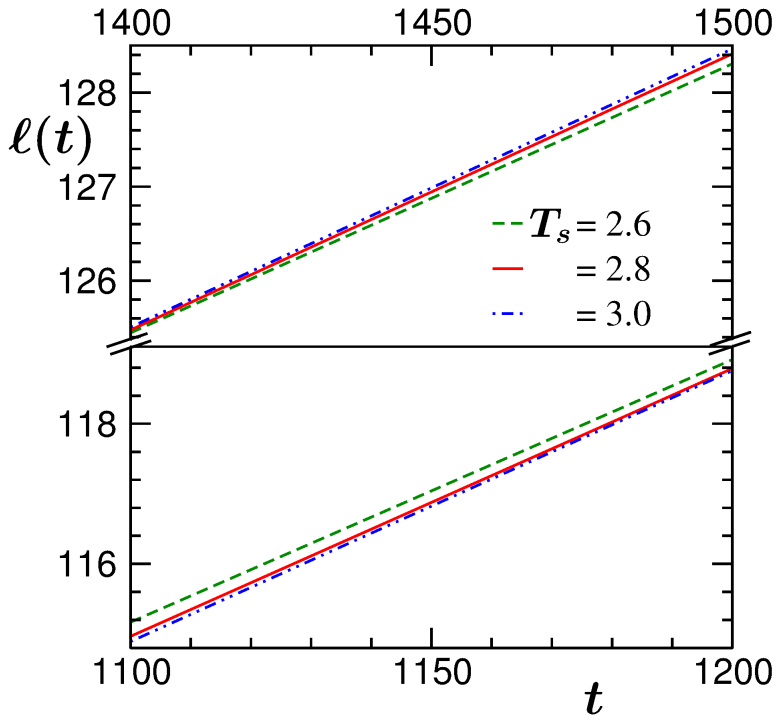

Figure 5.5: Same as Fig. 5.4. Here we have enlarged plots for three of the considered T_s values. The broken frame is adopted to bring clarity on the differences among early as well as late time data sets.

should get reflected in the *simple* scaling property [30],

$$C(r, T_s) \equiv \tilde{C}(r/\ell), \tag{5.3}$$

of the two-point equal time correlation function,

$$C(r, T_s) = \langle S_i S_j \rangle - \langle S_i \rangle \langle S_j \rangle. \tag{5.4}$$

Here r is the scalar distance between the points i and j, while $\tilde{C}(x)$ is a master function that should be independent of T_s. We intend to demonstrate the validity of the above mentioned scaling property for times below, equal to, and greater than the crossing times. For this purpose in Fig. 5.5 we have shown enlarged plots for a subset of T_s values considered in Fig. 5.4 [broken frames are used to bring clarity in both early and late time data sets]. From this figure it appears that the crossings among these length data sets occur around $t = 1300$. Thus, we have shown the scaling plots for the correlation functions, in Fig. 5.6 (a), (b) and (c), for $t = 1100$, 1300 and 1500. In each of the cases good collapse of data can be observed. This fact states that comparisons

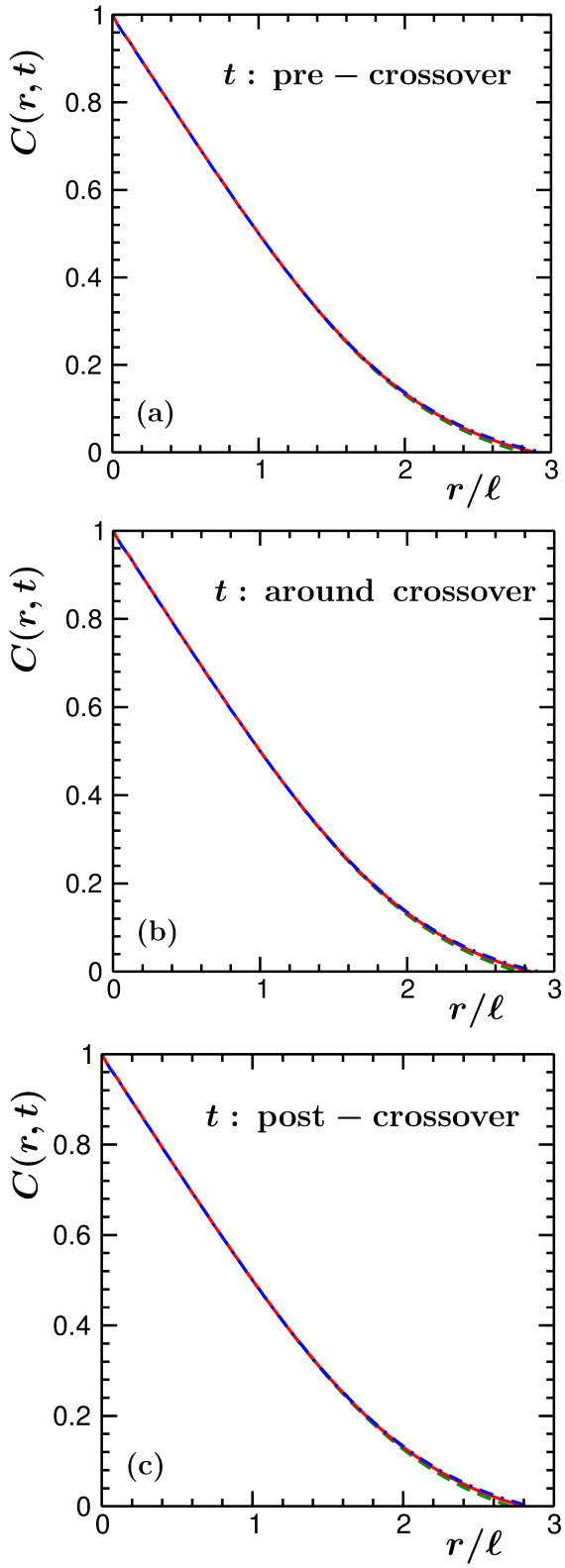

Figure 5.6: (a)-(c) Two-point equal time correlation functions, from different T_s, as used in Fig. 5.5, for three different times, are plotted versus r/ℓ, for quenches to $T_f = 0$. See text for details.

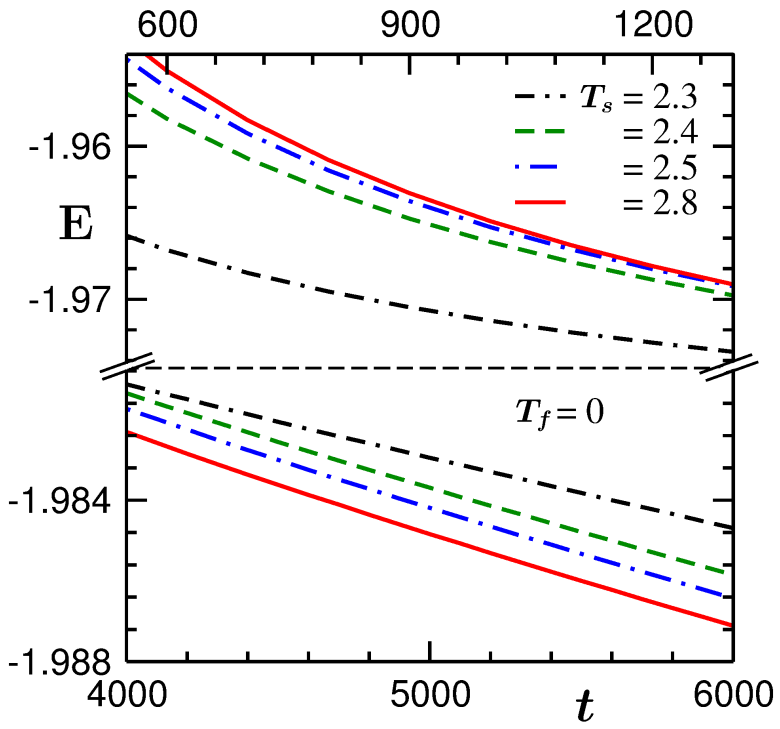

Figure 5.7: Energy per spin, E, is plotted as a function of time. Results from several different choices of T_s are shown. In each of these cases the systems were quenched to $T_f = 0$. The frame has been broken to bring clarity in both early time and late time trends in the data sets.

among length data from different T_s are meaningful. Here it is worth mentioning that the initial configurations with large enough spatial correlation is fractal in nature [32]. In that case the scaling at early enough times should follow the form [32, 44–46]

$$C(r, T_s) \equiv r^{d-d_f} \tilde{C}(r/\ell), \tag{5.5}$$

where d_f is the fractal dimension. This is consistent with the Ornstein-Zernike form [32, 41] $r^{-p}e^{-r/\xi}$. However, the observation of good data collapse for $d_f = d$ implies that the fractal features practically disappeared well before the crossing times. In the following we present results on energy decay. This is an alternative route for the confirmation of ME [3].

In Fig. 5.7 we show the time dependence of E, energy per spin, during evolutions for different T_s values, again by fixing T_f to zero. Like in Fig. 5.4, there exist crossings here as well. Systems with higher T_s, i.e., larger starting energy, are approaching new equilibrium faster. This, indeed, is the basic essence of ME. The crossings are very

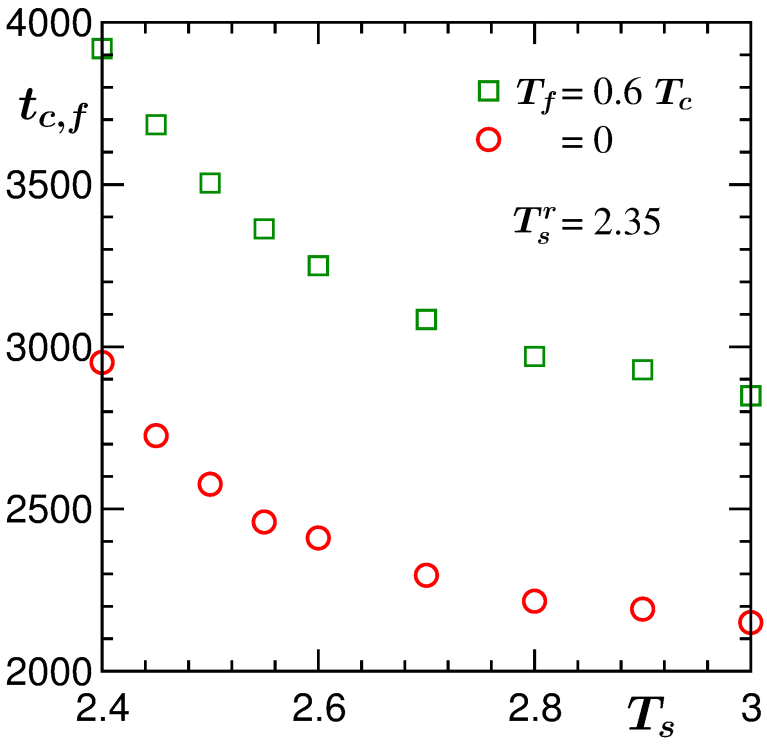

Figure 5.8: Plots of crossing times, $t_{c,f}$, versus T_s, of energy curves for different T_s values with that of a lower reference starting temperature, viz., $T_s^r = 2.35$. We have shown data for two values of T_f, viz., $T_f = 0$ and $T_f = 0.6T_c$.

systematic. This is owing to extremely good statistics. A better quantitative information on the trend of crossings is demonstrated in Fig. 5.8. Here we have plotted the crossing times, $t_{c,f}$, of energy curves for different values of T_s, following quenches to a T_f, with that for a reference value $T_s^r = 2.35$. We have shown results for $T_f = 0$ and $0.6T_c$. Each of these data sets conveys the message that energy plots for higher values of T_s are crossing the reference plot earlier. This indirectly implies that there exists crossing between any chosen pair of curves. This required feature is present in the plots for both the values of T_f.

A comparison between the two plots in Fig. 5.8 suggests that with the increase of T_f crossing between curves for two different T_s values has become delayed. This may imply that the crossing time will diverge with the approach of T_f towards T_c. A comprehensive exercise related to that is shown in Fig. 5.9. Here $t_{c,f}$ represent the crossing times between the energy curves for $T_s = 2.5$ and 2.6, following quenches to different T_f. The trend is consistent with the above anticipated singularity and points to a possibility that a phase transition is necessary to observe the ME, i.e., T_s and T_f

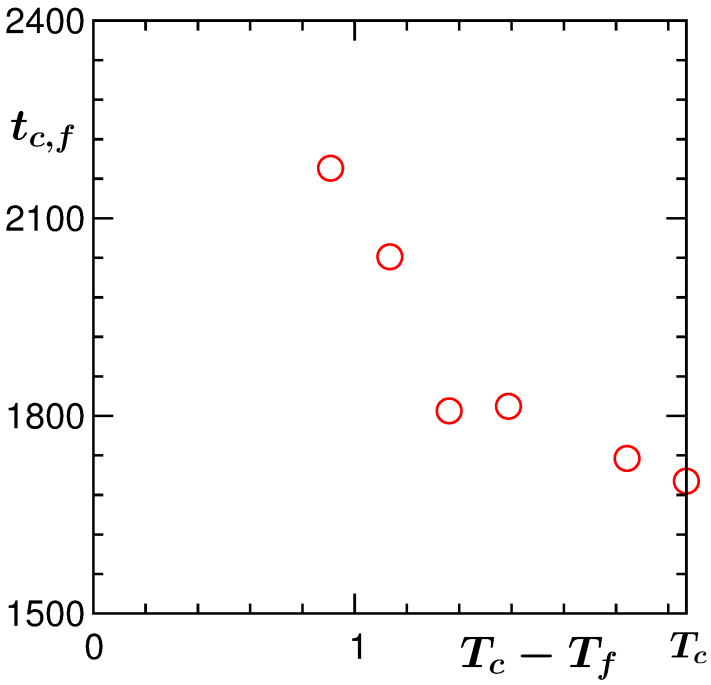

Figure 5.9: Plot of $t_{c,f}$, as a function of $T_c - T_f$, for crossings between energy curves from two T_s values, viz., 2.5 and 2.6. The data set is presented after averaging over 200000 independent initial realizations.

should lie on two sides of the critical point. However, for a concrete statement on the latter independent studies are needed by fixing T_s and T_f on the same sides of T_c.

To further ascertain the effects of critical fluctuations at T_f, on the magnitude of ME, we present additional results in Fig. 5.10. Given the debates on the topic, while good statistics is a necessity, it is also essential to demonstrate that there exists no bias in the presented results due to the averaging over a specific set of initial configurations. Keeping that in mind we have calculated the Pearson correlation coefficient [47],

$$r_{t_{c,f}T_f} = \sum_{f=1}^{n} x_f y_f \Big/ \sqrt{\sum_{f=1}^{n} x_f^2} \sqrt{\sum_{f=1}^{n} y_f^2}. \tag{5.6}$$

Here x_f and y_f are, respectively, $t_{c,f} - \overline{t}_c$ and $T_f - \overline{T}$, with $\overline{t}_c$ and $\overline{T}$ being averages of crossing times and quench temperatures for a sample of size n (= 6 here). We have calculated this coefficient by using $t_{c,f}$ versus T_f data that were obtained by averaging over increasing number (N) of initial configurations. The $r_{t_{c,f}T_f}$ versus N plot in Fig. 5.10 clearly conveys the message that the correlation between $t_{c,f}$ and T_f is positive, thereby discarding the possibility of aforementioned biasness unambiguously.

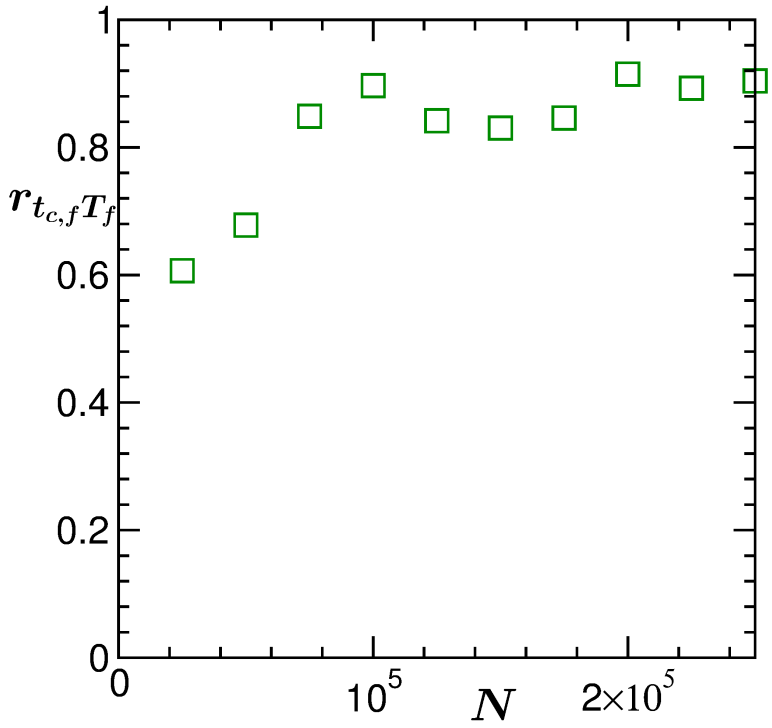

Figure 5.10: Pearson correlation coefficient, $r_{t_{c,f}T_f}$, is shown with the variation of N, the number of initial configurations used in the averaging.

5.4 Conclusion

We have studied the kinetics of phase transitions [30] in the two-dimensional nearest neighbor Ising model [32], via Monte Carlo simulations [35], using Glauber spin-flip dynamics [38]. This mimics the ordering dynamics in uniaxial ferromagnets. The objective has been to investigate the presence of the Mpemba effect [1]. For this purpose we have prepared initial configurations at various starting temperatures T_s, lying between T_c and ∞. These configurations, with 50:50 compositions of up and down spins, were quenched to various final temperatures T_f ($< T_c$). We observe that systems with higher T_s tend to approach the equilibrium at a T_f faster than the ones with lower T_s. This is the basic fact of the Mpemba effect [1].

While Mpemba effect itself is a counter-intuitive phenomena, observation of it in a simple system that is considered here is even more surprizing. Note that the model has no glassy ingredient. We have presented results for multiple values of T_f. In each of the cases, the effect is clearly identifiable. We have also shown that as T_f increases towards T_c, the crossing time between energy curves for a pair of starting temperatures increases.

This may imply that a phase transition is necessary for the observation of ME. However, further studies are necessary to arrive at such a conclusion.

Despite no in-built glassy feature, the model has been recognized [28, 48, 49] to exhibit unusual structure and slow dynamics at $T_f = 0$, particularly in $d = 3$. Such behavior may be considered to be a reason behind our striking observation. Nevertheless, interestingly, the effect is also observed for much higher values of T_f and in $d = 2$. Our results suggest that it persists at least till T_f is less than T_c. This work, thus, we expect to inspire further novel investigations, experimental as well as theoretical, with simple systems, providing path towards better understanding of the Mpemba effect.

In this work we have considered initial configurations with 50:50 compositions of up and down spins. It is equally important to study the case of asymmetric starting compositions. In this case also variation of the correlation length in the starting configurations can be realized with the change in temperature. Thus, the effect may be observed for non-zero initial magnetization as well. Our preliminary studies support this expectation. Nevertheless, more thorough studies are needed. Here we have considered the Glauber dynamics [38] for which the order parameter does not remain conserved over time. It will be interesting to extend the investigation to the conserved order-parameter dynamics via the implementation of Kawasaki exchange kinetics [36]. A systematic study of this, however, can be time taking. Note that in the case of Kawasaki kinetics, due to significantly slower growth [43] the crossings may occur at much later times.

Copyright and Permission

The results of this chapter have been published in:
Nalina Vadakkayil and Subir K. Das, "Should a hotter paramagnet transform quicker to a ferromagnet? Monte Carlo simulation results for Ising model", Phys. Chem. Chem. Phys. **23**, 11186 (2021).

We have reproduced the materials here following Copyright Policy of Royal Society of Chemistry, the publisher. See the publication link below:
https://pubs.rsc.org/en/content/articlelanding/2021/CP/D1CP00879J

References

[1] E.B. Mpemba and D.G. Osborne, Physics Education **4**, 172 (1969).

[2] M. Jeng, Am. J. Phys. **74**, 514 (2006).

[3] M. Baity-Jesi, E. Calore, A. Cruz, L.A. Fernandez, J.M. Gil-Narvión, A. Gordillo-Guerrero, D. Iñiguez, A. Lasanta, A. Maiorano, E. Marinari, V. Martin-Mayor, J. Moreno-Gordo, A.M. Sudupe, D. Navarro, G. Parisi, S. Perez-Gaviro, F. Ricci-Tersenghi, J.J. Ruiz-Lorenzo, S.F. Schifano, B. Seoane, A. Tarancoń, R. Tripiccione, and D. Yllanes, Proc. Natl. Acad. Sci. U. S. A. **116**, 15350 (2019).

[4] Aristotle, *Meteorologica*, translated by H.D.P. Lee (Harvard University Press, 1962), Book I, Chap. XII, pp. 85-87.

[5] R. Descartes, *Discourse on Method, Optics, Geometry, and Meteorology*, translated by P.J. Olscamp (Bobb-Merrill, Indianapolis, 1965), Chap. 1, p. 268.

[6] R. Bacon, *The Opus Majus of Roger Bacon*, translated by R.B. Burke (Russell and Russell, New York, 1962), Vol. II, Part 6, p. 584.

[7] F. Bacon, *"Novum Organum," in The Physical and Metaphysical Works of Lord Francis Bacon*, edited by J. Devey (H.G Bohn, York street, 1853), Book II, Chap. L, p. 559.

[8] J. Black, Phil. Trans. R. Soc. Lon. **65**, 124 (1775).

[9] D. Auerbach, Am. J. Phys. **63**, 882 (1995).

[10] X. Zhang, Y. Huang, Z. Ma, Y. Zhou, J. Zhou, W. Zheng, Q. Jiang, and C.Q. Sun, Phys. Chem. Chem. Phys. **16**, 22995 (2014).

[11] J. Jin and W.A. Goddard III, J. Phys. Chem. C **119**, 2622 (2015).

[12] P.A. Greaney, G. Lani, G. Cicero, and J.C. Grossman, Metall. Mater. Trans. A **42**, 3907 (2011).

[13] Z. Lu and O. Raz, Proc. Natl. Acad. Sci. U. S. A. **114**, 5083 (2017).

[14] A. Lasanta, F.V. Reyes, A. Prados, and A. Santos, Phys. Rev. Lett. **119**, 148001 (2017).

[15] A. Torrente, M.A. López-Castaño, A. Lasanta, F.V. Reyes, A. Prados, and A. Santos, Phys. Rev. E **99**, 060901(R) (2019).

[16] I. Klich, O. Raz, O. Hirschberg, and M. Vucelja, Phys. Rev. X **9**, 021060 (2019).

[17] A. Gal and O. Raz, Phys. Rev. Lett. **124**, 060602 (2020).

[18] A. Kumar and J. Bechhoefer, Nature **584**, 64 (2020).

[19] P. Chaddah, S. Dash, K. Kumar, and A. Banerjee, arXiv.1011.3598 (2010).

[20] H.C. Burridge and P.F. Linden, Scientific Reports **6**, 37665 (2016).

[21] T.S. Kuhn, *The Structure of Scientific Revolutions* (The University of Chicago Press, Chicago, 1970), 2nd ed.

[22] P. Zalden, F. Quirin, M. Schumacher, J. Siegel, S. Wei, A. Koc, M. Nicoul, M. Trigo, P. Andreasson, H. Enquist, M.J. Shu, T. Pardini, M. Chollet, D. Zhu, H. Lemke, I. Ronneberger, J. Larsson, A.M. Lindenberg, H.E. Fischer, S. Hau-Riege, D.A. Reis, R. Mazzarello, M. Wuttig, and K. Sokolowski-Tinten, Science **364**, 1062 (2019).

[23] X.L. Phuah, W. Rheinheimer, Akriti, L. Dou, and H. Wang, Scr. Mater. **195**, 113719 (2021).

[24] K. Binder and A.P. Young, Rev. Mod. Phys. **58**, 801 (1986).

[25] H. Rieger, Annual Rev. of Computational Physics II, 295 (1995).

[26] V. Lubchenko and P.G. Wolynes, Annual Review of Physical Chemistry **58**, 235 (2007).

[27] D.S. Fisher and D.A. Huse, Phys. Rev. B **38**, 373 (1988).

[28] N. Vadakkayil, S. Chakraborty, and S.K. Das, J. Chem. Phys. **150**, 054702 (2019).

[29] S. Puri and V. Wadhawan (ed.), *Kinetics of Phase Transitions* (CRC Press, Boca Raton, 2009).

[30] A.J. Bray, Adv. Phys. **51**, 481 (2002).

[31] A. Onuki, *Phase Transition Dynamics* (Cambridge University Press, Cambridge, UK, 2002).

[32] M.E. Fisher, Rep. Prog. Phys. **30**, 615 (1967).

[33] S. Chakraborty and S.K. Das, Eur. Phys. J. B **88**, 160 (2015).

[34] S. Chakraborty and S.K. Das, Phys. Rev. E **93**, 032139 (2016).

[35] K. Binder and D.W. Heermann, *Monte Carlo Simulations in Statistical Physics* (Springer, Springer Nature, Switzerland, 2019).

[36] D.P. Landau and K. Binder, *A Guide to Monte Carlo Simulations in Statistical Physics* (Cambridge University Press, Cambridge, 2009).

[37] D. Frenkel and B. Smit, *Understanding Molecular Simulations: From Algorithms to Applications* (Academic Press, San Diego, 2002).

[38] R.J. Glauber, J. Math. Phys. **4**, 294 (1963).

[39] U. Wolff, Phys. Rev. Lett. **62**, 361 (1989).

[40] S.K. Das, J. Horbach, K. Binder, M.E. Fisher, and J.V. Sengers, J. Chem. Phys. **125**, 024506 (2006).

[41] J.-P. Hansen and I.R. McDonald, *Theory of Simple Liquids* (Academic Press, London, 1986).

[42] S.K. Das, J. Horbach, and K. Binder, J. Chem. Phys. **119**, 1547 (2003).

[43] S. Majumder and S.K. Das, Phys. Chem. Chem. Phys. **15**, 13209 (2013).

[44] T. Vicsek, M. Swesinger, and M. Matsnshita, *Fractals in Natural Sciences* (World scientific, Singapore, 1994).

[45] J. Midya and S.K. Das, Phys. Rev. Lett. **118**, 165701 (2017).

[46] S. Paul, A. Bera, and S.K. Das, Soft Matter **17**, 645 (2021).

[47] K. Pearson, Proc. R. Soc. London **58**, 240 (1895).

[48] J. Olejarz, P.L. Krapivsky and S. Redner, Phys. Rev. E **83**, 030104(R) (2011).

[49] T. Blanchard, L.F. Cugliandolo, M. Picco, and A. Tartaglia, J. Stat. Mech. P113201 (2017).

Chapter 6

Dynamics of Cluster Growth during Phase Transitions in a Three-dimensional Single Component Lennard-Jones System

6.1 Introduction

When a homogeneous system is suddenly quenched inside the coexistence region, the system becomes unstable. It evolves towards the new equilibrium state via clustering or domain coarsening, till a complete phase change occurs [1–29]. Based on the conservation of relevant order parameter, these transition kinetics are typically divided into categories of nonconserved or conserved dynamics [1]. In the case of conserved order parameter dynamics, the relevant system integrated order-parameter does not change during a phase change. Examples of this category include phase separation processes in various passive [6–26] and active [27–30] matter systems. In both the passive and active cases, types of phase transitions can be vapor-liquid, solid-liquid or vapor-solid, depending on the values of thermodynamic parameters involved. In this chapter we will be focusing on the latter type of phase transition in the context of a single component Lennard-Jones system, representing a passive scenario.

Coarsening mechanism in systems, where one or more phases are fluid, hydrodynamics plays important role. Manifestation of the latter depends on the composition or overall densities [1–5]. For quenches of fluids with critical compositions or densities,

domain morphology is bicontinuous in nature [1–10], as often observed during spinodal decomposition. The growth occurs due to pressure gradient across the tube-like domains, as discussed by Siggia [11]. On the other hand, for an off-critical fluid, i.e., for quenches with density or composition close to one of the branches of the coexistence curve, coarsening progresses following nucleation of disconnected droplets of the minority phase [6, 11, 12]. There, the growth proceeds via the inelastic collisions among droplets that undergo thermal motion of various types [12, 13]. This picture may apply to vapor-solid transitions as well. For diffusive motion of the droplets a quantitative picture was provided by Binder and Stauffer (BS) [12]. Here, note that, in the case of off-critical solid binary mixtures, as discussed by Lifshitz, Slyozov and Wagner [15, 16], the big droplets get bigger by concentration diffusion in the absence of hydrodynamics. In fluids, the coupling between velocity and concentration (or density) fields makes the process more complicated [1, 11, 12, 17–19]. Furthermore, when density and temperature are very low, following nucleation, fractal structures may appear in a single component system undergoing vapor-solid transition [22]. The growth mechanism in this case was shown to be rather different from the standard ones typically discussed in the literature. The latter study was for spatial dimension $d = 2$. In this chapter, we investigate the mechanism of formation and growth of fractal structures in a single-component system in $d = 3$, by exploring a broad region of the temperature-density phase diagram.

In general, the domain growth during a phase separation process obeys a power-law [1, 2]:

$$\ell(t) \sim t^{\alpha}, \tag{6.1}$$

where $\ell(t)$ is the average domain length in the system and α is the growth exponent. Usually the evolution proceeds in a self-similar manner where the domain morphologies at different times differ only in the values of $\ell(t)$. The growing structure is typically probed via the two-point equal time correlation function [1, 2],

$$C(r,t) = \langle \psi(\vec{r},t)\psi(\vec{0},t)\rangle - \langle \psi(\vec{r},t)\rangle\langle \psi(\vec{0},t)\rangle;\ r = |\vec{r}|. \tag{6.2}$$

Here ψ is the order parameter. For the *standard* self-similar structures, this follows the scaling form [1, 2],

$$C(r,t) \equiv \tilde{C}(r/\ell(t)), \tag{6.3}$$

where $\tilde{C}(x)$ is a time independent master function.

To determine the value of the growth exponent, α, in the case of BS mechanism, one can write the rate of decrease in droplet density, n, that occurs due to merger following

collisions, as [6, 11, 12]

$$\frac{dn}{dt} = -Bn^2, \tag{6.4}$$

where B is a positive constant. In terms of the average domain length, noting that $n \propto 1/\ell^d$, the above equation modifies to

$$\frac{d\ell}{dt} = B' \frac{1}{\ell^{d-1}}, \tag{6.5}$$

providing $\alpha = 1/d$, B' being another positive constant. This give a value 1/3 in the present case ($d = 3$). If we consider the fractal structure formation and break down of the BS mechanism at very low densities and temperatures, it is important to check for the possibility of ballistic aggregation [31] in the system. For ballistic aggregation of fractal or non-fractal objects, the rate of change of droplet density can be written as [22, 31]

$$\frac{dn}{dt} = -\text{`Collision cross section'} \times \langle v_{rel} \rangle \times n^2, \tag{6.6}$$

where $\langle v_{\rm rel} \rangle$ is the average relative velocity of the clusters. This will be equal to the root mean square velocity, v_{rms}, in the case of uncorrelated motion of the clusters [31]. The collision cross section is the area which can be written as R_g^2 in $d = 3$. Here, R_g is the radius of gyration, which is an appropriate length scale in the case of fractal objects. By incorporating these facts in Eq. (6.6), one arrives at

$$\frac{dn}{dt} = -R_g^2 \times v_{rms} \times n^2. \tag{6.7}$$

The growth in the system can be examined by calculating the average mass of the clusters, $M(t)$, which has typically a power-law behavior in time as [22]

$$M(t) \sim t^{\beta}. \tag{6.8}$$

Here $M(t)$ can be related to the droplet density as

$$n \propto 1/M. \tag{6.9}$$

Also $M(t)$ in terms of R_g can be written as [22]

$$M(t) \sim R_g^{d_f}, \tag{6.10}$$

where d_f is the fractal dimensionality of the system. Following the incorporation of the above facts and the assumption that v_{rms} has a power-law behavior [22]

$$v_{rms} \sim M^{-v_r}, \tag{6.11}$$

Eq. (6.7) gets modified to

$$M(t) \sim t^{1/(v_r+1-2/d_f)}, \tag{6.12}$$

implying [22, 28, 29]

$$\beta = \frac{1}{v_r + 1 - \frac{2}{d_f}}. \tag{6.13}$$

Our objective here is to investigate the above discussed ballistic aggregation mechanism in the considered model for fractal clusters over a reasonably wide region inside the coexistence curve. In the next section, a brief discussion on the model and methods is given, followed by the results and conclusion in the subsequent sections.

6.2 Model and Methods

Our model system consists of unit diameter ($\sigma = 1$) particles, with an overall (particle) density $\rho = 0.04$, interacting with each other via a truncated, shifted, and force-corrected Lennard-Jones (LJ) potential of the form [10, 18]

$$U(r) = u(r) - u(r_c) - (r - r_c)\left(\frac{du}{dr}\right)_{r=r_c}, \tag{6.14}$$

where

$$u(r) = 4\varepsilon\left[\left(\frac{\sigma}{r}\right)^{12} - \left(\frac{\sigma}{r}\right)^{6}\right], \tag{6.15}$$

with r_c ($= 2.5\sigma$) being the cut-off distance. The critical density, ρ_c, and the critical temperature, T_c, for the vapor-liquid transition within this model are estimated to be 0.316 and $0.939\varepsilon/k_B$, respectively [26], k_B being the Boltzmann constant. Along with σ, we set ε (interaction strength) and k_B also to unity. The system is kept inside a cubic simulation box of linear dimension $L = 128$, measured in units of σ. We use molecular dynamics (MD) simulations in canonical (NVT) ensemble by implementing the velocity Verlet algorithm [32, 33], with periodic boundary conditions imposed along all directions. The temperature was controlled via the implementation of a Nosé-Hoover (NHT) thermostat [34, 35] which is considered to be good for preserving hydrodynam-

ics. Homogeneous systems of low overall density (0.04, as mentioned above), which is prepared at very high temperature, is quenched to different final temperatures (T_f) that fall inside the coexistence region. The time in our simulation is measured in units of $(m\sigma^2/\varepsilon)^{1/2}$. The integration time step, Δt, was varied between 0.005 and 0.01, for the solution of the dynamical equations.

The average domain length, $\ell(t)$, is calculated via the equation [18, 21],

$$\ell(t) = \int P(\ell_d, t)\ell_d d\ell_d, \tag{6.16}$$

$P(\ell_d, t)$ being a distribution function and ℓ_d, the size of a domain, is the distance between two successive interfaces in a specific direction. In order to obtain $C(r, t)$ and $\ell(t)$, we mapped the systems to a simple cubic lattice by assigning particles on the lattice points according to the local density [18, 20, 21]. If the local density of a site is greater than the critical density, we assign a particle to the particular site, otherwise, we let the site be empty. This makes the system resemble a two-component Ising system having spin values $+1$ or -1 at each of the sites. Following this, a noise removal has also been performed by applying the majority spin rule, where a site gets occupied by a particle if the majority of the nearest neighboring sites are occupied. For the calculation of M, we have appropriately identified the domain boundaries [18, 20].

All the presented results below are averaged over a minimum of 20 initial configurations.

6.3 Results

We start by presenting the evolution snapshots of a system, following a quench to $T_f = 0.2$, in Fig. 6.1. The formation of disconnected clusters is clearly visible. The early time snapshot contains spherical droplets. At later time, filament-like fractal structures appear. Below we try to understand the reason behind the formation and growth of such clusters.

In the low density regime, a natural expectation for cluster growth is via the diffusive transport of droplets [12]. The average domain length of the system, as explained above, in this case, should have a power-law behavior with the exponent $\alpha = 1/3$ in $d = 3$. In Fig. 6.2, we present a plot of the average droplet size $\ell(t)$, versus t, on a double logarithmic scale. From the figure, it appears that the power-law exponent is smaller.

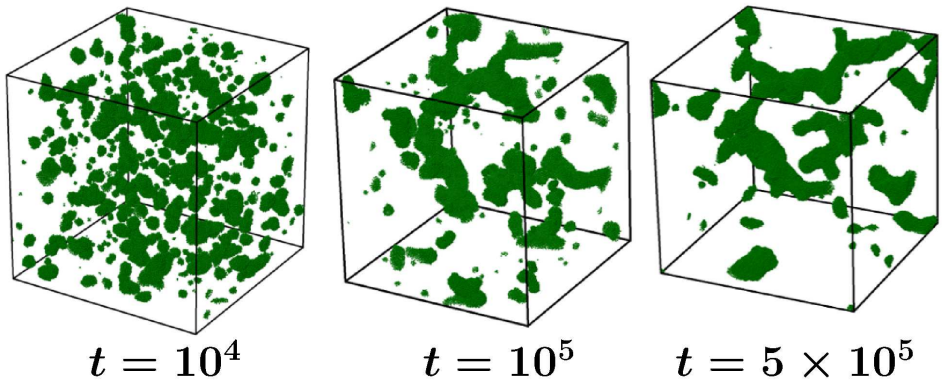

Figure 6.1: Evolution snapshots of a system, following a quench to $T_f = 0.2$, with $L = 128$, are shown from different times. The late time snapshots contain fractal clusters.

It is $\simeq 0.24$, deviating by about 30% from the expectation. To investigate for this, we look for the mechanism other than diffusive coalescence in these systems.

To understand the cluster motion in our system of interest, we calculate the mean squared displacement (MSD) of the clusters [36] at late times. A plot of MSD, versus the translated time, $t' = t - t_0$, for two different clusters are shown in a log-log scale in Fig. 6.3(a). Here t_0 is the time from when the calculation started. The MSD has been calculated for the clusters over periods before they undergo any collisions with the others. To ascertain that no collision occurred in between, we calculated the number of particles (N_p) in each of the considered clusters. The corresponding plots are shown in Fig. 6.3(b), from where it is evident that the particle number in each of the clusters is almost constant for the presented time range [only one sided fluctuation in the data sets is a low temperature feature – because of very low density of the vapor phase only the same set of particles get occasionally detached and attached to the parent droplet]. This also confirms that the contribution due to Lifshitz-slyozov particle diffusion mechanism is weak. The data in Fig. 6.3(a) are consistent with a power-law exponent 2, which points to the fact that the clusters undergo ballistic motion. This is in agreement with a study on 2D Lennard-Jones fluid at low temperature and low density where also the cluster motion was reported to be ballistic [22]. There the system was shown to coarsen via sticky collisions among the clusters, i.e., via the ballistic aggregation mechanism [31].

When a sticky collision occurs between two clusters, the newly formed structure minimizes the surface free energy by trying to attain a spherical shape. The time scale of this process competes with that of collisions via the ballistic motion of droplets. After

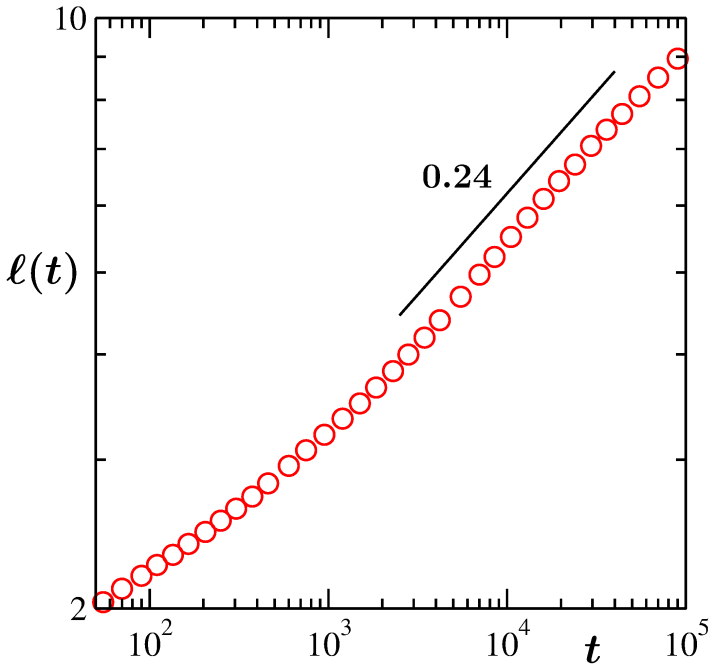

Figure 6.2: Log-log plot of the average domain size, $\ell(t)$, as a function of time, corresponding to the quench picture depicted in Fig. 6.1. The solid line denotes a power-law with the exponent mentioned next to it.

a collision, before the structure can attain a spherical shape, it is possible that the cluster encounter a new collision. This leads to the formation of fractal structures with branches. The corresponding dimensionality, d_f, of these structures can be quantified via Eq. (6.10). A plot of $M(t)$ versus R_g, in a log-log scale, is shown in Fig. 6.4 for a quench to $T_f = 0.2$. The power-law exponent for the late time data comes out to be $\simeq 2.75$ ($< d = 3$). This confirms the presence of fractal structure. Note that R_g was calculated as

$$R_g = \left[\frac{1}{N_p} \sum_{i=1}^{N_p} (\vec{r}_i - \vec{r}_{cm})^2 \right]^{1/2} , \tag{6.17}$$

where $\vec{r}_i$ is the position of the i^{th} particle, $\vec{r}_{cm}$ is the location of the centre of mass of the cluster, and N_p is the total number of particles inside the cluster.

The value of d_f, we observe, depends strongly on the quench temperature. In Fig. 6.5, we plot d_f as a function of quench temperature. From this plot, we see that d_f decreases with the increase in T_f. This is contrary to the natural expectation that d_f should increase with T_f. This expectation is because: as the temperature increases, the motion of particles inside each droplet increases that should help minimization of surface free energy faster. However, with the decrease in T_f, a newly formed droplet gets longer

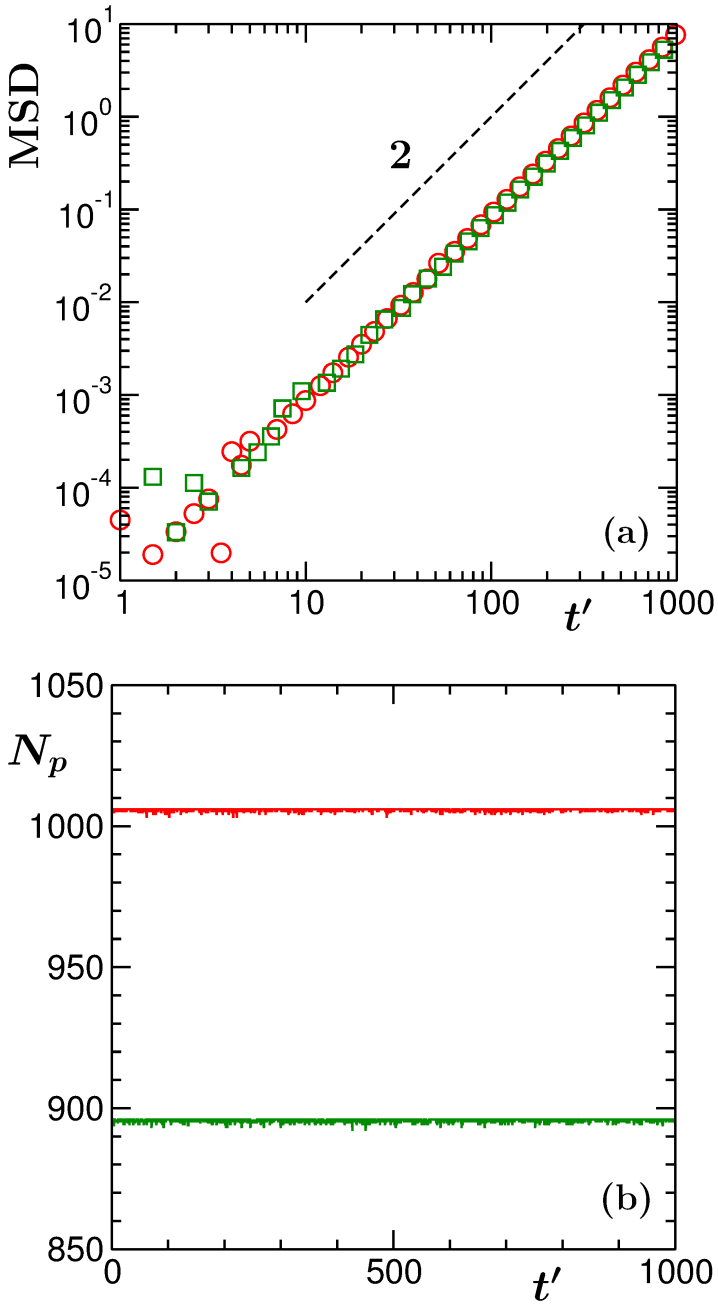

Figure 6.3: (a) Mean squared displacements (MSD) are plotted as a function of translated time t' for two different clusters. The dashed line represents a power-law with exponent 2, which signifies the ballistic motion of the clusters. (b) The number of particles in each of the clusters, N_p, for which the MSD are presented in part (a). All results are for quenches to $T_f = 0.2$.

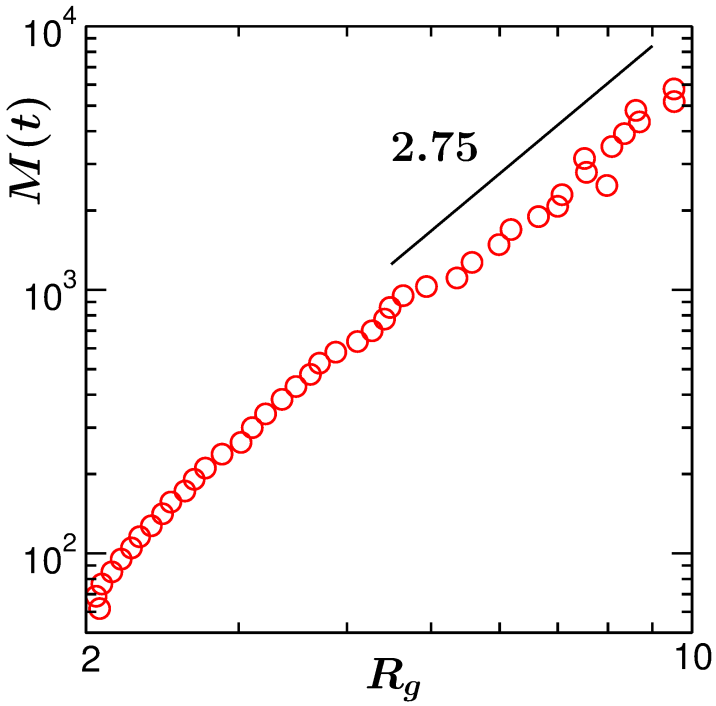

Figure 6.4: Plot of the average mass of the clusters, $M(t)$, as a function of R_g, for a quench to $T_f = 0.2$. The solid line denotes a power-law with an exponent $d_f \simeq 2.75$.

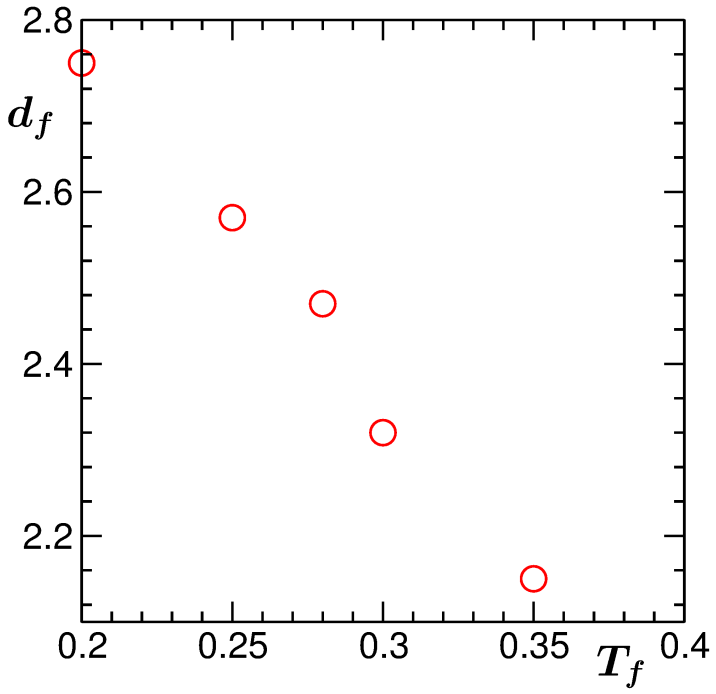

Figure 6.5: Plot of d_f as a function of quench temperature.

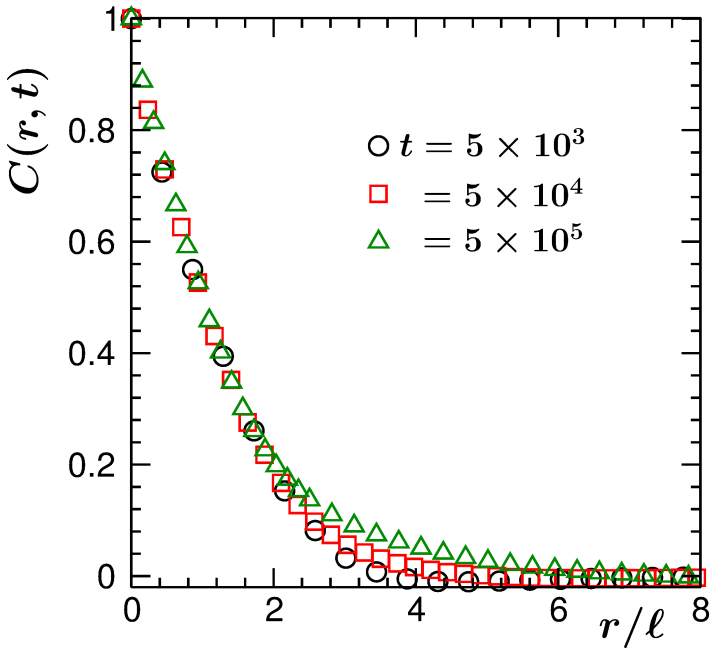

Figure 6.6: Plot of $C(r,t)$, versus r/ℓ, from different times, for $T_f = 0.2$. The non-scaling behavior implies that the structures at different times are not self-similar, in standard sense.

time for minimizing the surface free energy, because of the slower ballistic motion of the clusters, thereby, attaining a shape more close to a sphere. This, perhaps, leads to a higher value of d_f.

Evidently, the structures during this evolution will not be self-similar in nature, in standard sense, due to the presence of fractality. This fact can be captured via the usual scaling plots of the two-point equal-time correlation function, $C(r,t)$. Plot of $C(r,t)$, versus r/ℓ, from different times, following a quench to $T_f = 0.2$, are provided in Fig. 6.6. There is no collapse of data from different times which confirms the non-self-similarity of the structures at later times. To obtain data collapse in this case one needs to modify the scaling form by incorporating the difference $d - d_f$. However, in the present case, the value of d_f changes as the system evolves, for a significant period of time. If in the scaling exercise this fact is taken into account data collapse can be obtained. In systems for which d_f is time independent, the procedure is relatively trivial. Thus, for this problem this is a complex exercise which suggests that cluster mass, rather than the length, is a better quantity to probe.

Given that the motion of the clusters at late time is ballistic, cluster growth can be explained via the theory of ballistic aggregation. According to the theory, the average

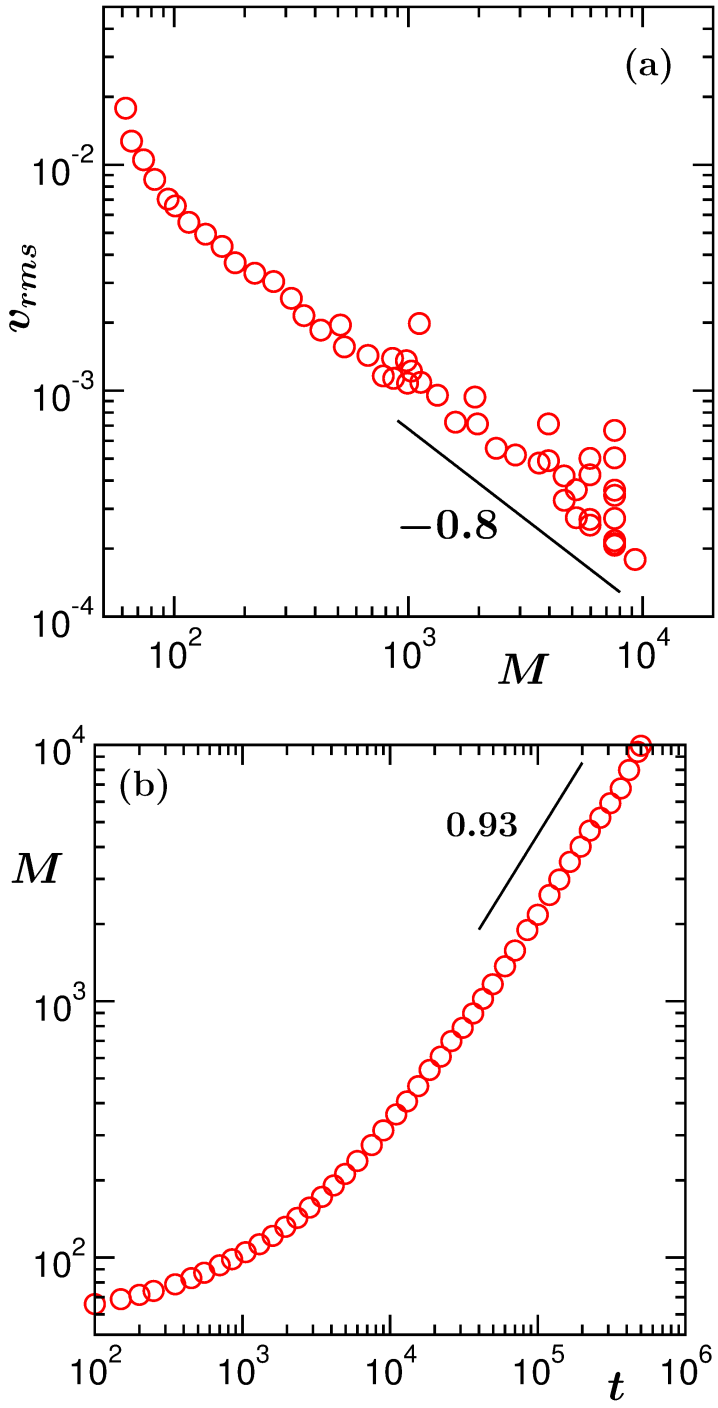

Figure 6.7: (a) Plot of v_{rms} versus $M(t)$ in a double-log scale. The solid line is a power-law, the exponent for which is mentioned in the figure. (b) Plot of $M(t)$ versus t in a double-log scale. The solid line is a power-law with an exponent that is obtained by using Eq. (6.13). All the results are for a quench to $T_f = 0.2$.

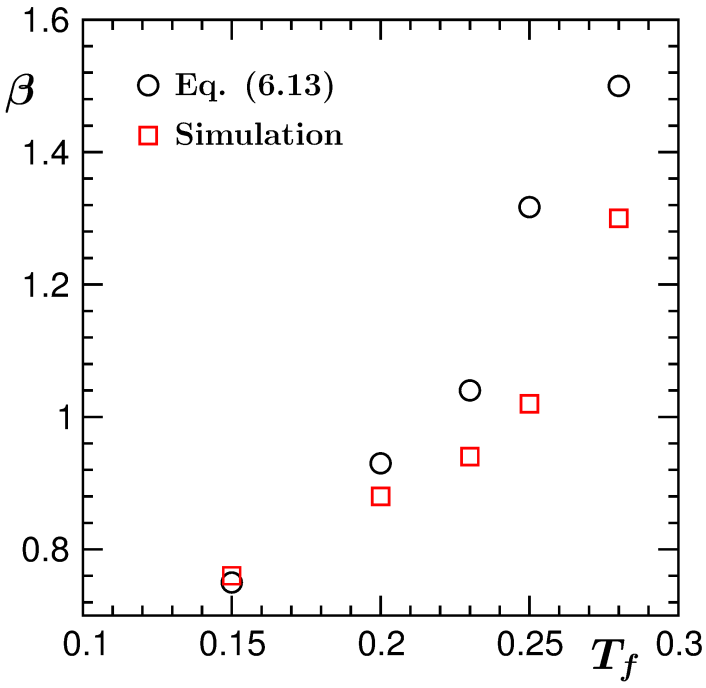

Figure 6.8: A comparative picture of the values of β obtained from Eq. (6.13) and from simulations.

mass of the clusters, $M(t)$, grows in a power-law fashion with an exponent β that is quoted in Eq. (6.13) in Sec. 6.1. The value of the exponent v_r can be quantified from the root-mean-squared velocity – see Eq. (6.11). A plot of v_{rms} as a function of $M(t)$ in a log-log scale is shown in Fig. 6.7(a) for quenches to $T_f = 0.2$. From this we quantify $v_r \simeq 0.8$. The deviation from the value 0.5 may imply correlation in cluster motions. By incorporating this value of v_r and d_f ($\simeq 2.75$) in Eq. (6.13), we obtain

$$\beta \simeq 0.93. \tag{6.18}$$

A plot of $M(t)$, as a function of t, in a log-log scale, is displayed in Fig. 6.7(b). A power-law with this value of β is also shown here. The simulation data are consistent with this.

We have calculated β for a wide range of temperature within which the ballistic aggregation picture applies. A comparison of the values of β obtained directly from the simulation data for growth and the ones that emerge from Eq. (6.13) is provided in Fig. 6.8. The agreement between the trends obtained from the theory and the simulation is satisfactory in this low temperature regime, the numbers being consistent with each

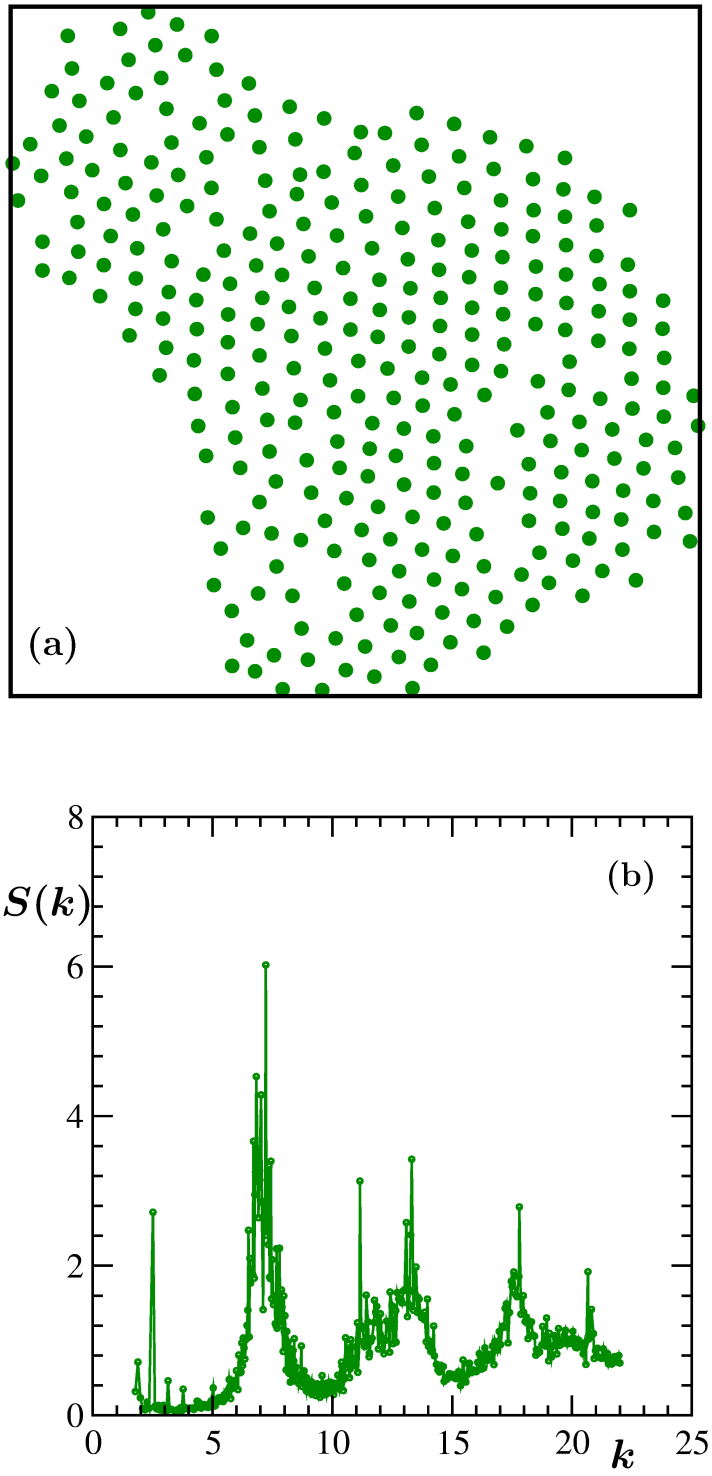

Figure 6.9: (a) A 2D slice of a cluster at $t = 4 \times 10^4$, for $T_f = 0.2$. (b) Plot of the structure factor, $S(k)$, as a function of k, for a cluster, for which the snapshot of a 2D slice is given in part (a).

other within about 10%. The discrepancy can be attributed to lack of statistics as well as the assumption that $v_{rms} \sim M^{-v_r}$ even when there exists correlation in cluster velocities.

In Fig. 6.9, we demonstrate structural aspects inside a typical cluster formed during evolution at $T_f = 0.2$. In part (a) of this figure we show a 2D slice (from $t = 4 \times 10^4$). Regular arrangement of atoms can be appreciated. We calculate the structure factor, $S(k)$, defined as [36]

$$S(k) = \frac{1}{N_p}\Big\langle \sum_{i=1}^{N_p} \exp(i\vec{k}.\vec{r})\Big\rangle, \tag{6.19}$$

where $\vec{r} = r_i - r_j$ and $\vec{k}$ is the wave vector. Fig. 6.9(b) shows the plot of $S(k)$ versus k, in which there are peaks confirming the presence of crystalline ordering. This ordering inside the cluster reduces the movement of the particles inside the cluster, and, in turn, leads to the formation of fractal clusters in the system. This exercise implies that a vapor-solid phase transition is occurring in the considered temperature-density regime.

6.4 Conclusion

We have studied the evolution of a single component system, with particles interacting via the Lennard-Jones potential, at low density and temperature regime inside the co-existence curve for vapor-solid phase transitions that the model exhibits. Because of low density the solid clusters are disconnected. These are fractal in nature. Here the growth dynamics is different from the usually expected BS mechanism. Rather than diffusive motions, the clusters undergo ballistic motion. The fractal dimension, d_f, of the clusters strongly depends on the final temperature. At very low temperature regime, d_f decreases with an increase in T_f. This is due to the interesting interplay between two time scales present in the system.

The average mass of clusters grow with time in a power-law fashion. The corresponding exponent, β, also appears to be temperature dependent. This we have tried to understand via a ballistic aggregation theory by incorporating the information on temperature dependent d_f. The theory produces correct trend and reasonable accuracy.

References

[1] A.J. Bray, Adv. Phys. **51**, 481 (2002).

[2] *Kinetics of Phase transition*, edited by S. Puri and V. Wadhawan (CRC Press, Boca Raton, 2009).

[3] R.A.L. Jones, *Soft Condensed Matter* (Oxford University Press, Oxford, 2008).

[4] K. Binder, in *Phase Transformation of Materials*, edited by R.W. Cahn, P. Haasen, and E.J. Kramer (VCH, Weiheim, 1991), Vol. 5, p. 405.

[5] A. Onuki, *Phase Transition Dynamics* (Cambridge University Press, Cambridge, 2002).

[6] K. Binder, Phys. Rev. B **15**, 4425 (1977).

[7] H. Tanaka, J. Chem. Phys. **103**, 2361 (1995).

[8] H. Tanaka, J. Chem. Phys. **105**, 10099 (1996).

[9] H. Tanaka, J. Chem. Phys. **107**, 3734 (1997).

[10] S. Majumder and S. K. Das, Europhys. Lett. **95**, 46002 (2011).

[11] E.D. Siggia, Phys. Rev. A **20**, 595 (1979).

[12] K. Binder and D. Stauffer, Phys. Rev. Lett. **33**, 1006 (1974).

[13] H. Furukawa, Phys. Rev. A **31**, 1103 (1985).

[14] J. Midya and S.K. Das, J. Chem. Phys. **146**, 024503 (2017).

[15] I.M. Lifshitz and V.V. Sloyozov, J. Phys. Chem. Solids **19**, 35 (1961).

[16] C. Wagner, Z. Elektrochem. **65**, 581 (1961).

[17] P.C. Hohenberg and B.I. Halperin, Rev. Mod. Phys. **49**, 435 (1977).

[18] S. Roy and S.K. Das, Phys. Rev. E **85**, 050602(R) (2012).

[19] S.K. Das, S. Roy, S. Majumder, and S. Ahmed, Europhys. Lett. **97**, 66006 (2012).

[20] S. Roy and S.K. Das, Soft Matter **9**, 4178 (2013).

[21] S. Roy and S.K. Das, J. Chem. Phys. **139**, 044911 (2013).

[22] J. Midya and S.K. Das, Phys. Rev. Lett. **118**, 165701 (2017).

[23] T. Lookman, Y. Wu, F.J. Alexander, and S. Chen, Phys. Rev. E **53**, 5513 (1996).

[24] C. Dutt, S.P. Tampi, and R. Govindarajan, Phys. Rev. E **91**, 010101(R) (2015).

[25] R. Shimizu and H. Tanaka, Nat. Commun. **6**, 7407 (2015).

[26] J. Midya and S.K. Das, J. Chem. Phys. **146**, 044503 (2017).

[27] S. Chakraborty and S.K. Das, J. Chem. Phys. **153**, 044905 (2020).

[28] S. Paul, A. Bera, and S.K. Das, Soft Matter **17**, 645 (2021).

[29] A. Bera, S. Sahoo, S. Thakur, and S.K. Das, arXiv:2012.15043.

[30] M.C. Marchetti, J.F. Joanny, S. Ramaswamy, T.B. Liverpool, J. Prost, M. Rao, and R.A. Simha, Rev. Mod. Phys. **85**, 1143 (2013).

[31] G.F. Carnevale, Y. Pomeau, and W.R. Young, Phys. Rev. Lett. **64**, 2913 (1990).

[32] M.P. Allen and D.J. Tildesley, *Computer Simulations of Liquids* (Clarendon, Oxford, 1987).

[33] D. Frenkel and B. Smit, *Understanding Molecular Simulations: From Algorithms to Applications* (Academic Press, San Diego, 2002).

[34] S. Nosé, J. Chem. Phys. **81**, 511 (1984).

[35] W.G. Hoover, Phys. Rev. A **31**, 1695 (1985).

[36] J.-P. Hansen and I.R. McDonald, *Theory of Simple Liquids* (Academic Press, London, 2008).

Chapter 7

Study of Disease Spread via a Scaling Approach

7.1 Introduction

The outbreak of COVID-19, a disease caused by a novel coronavirus, has led to renewed interest in the understanding of disease spread [1–9]. Efforts to recognize the patterns in disease spread have started long back [10–12]. In the literature of epidemiology, there are several mathematical models. The list includes SI (Susceptible-Infected) model, SIR (Susceptible-Infected-Recovered) model, etc. [11–16]. Modelling of disease spread using the concepts of percolation theory has also been of recent interest where the percolation probability is connected with the probability of infection through direct contact with an already infected individual [8, 17]. Outcomes of studies via these models suggest an exponential growth in the number of infections in the early days of the spread [14–16]. This can be understood by considering the fact that a single infected individual can infect another within certain period, and these two infected individuals can further infect two within the same interval, and so on. After this rapid initial spread, there occurs a crossover to a slower growth regime. The spread in this regime depends on various factors [1–8, 10–16]. Some of these are related to the efficiency of identification and isolation of the patients, recoveries and deaths of the infected individuals, the incubation period, the social restrictions imposed by the governments, etc. Thus, mathematical description of the *overall* spread of disease, and understanding of it, during an epidemic is a challenging task.

When an epidemic ends, the total number of infections can at the most equal the total population in the given geographical region, with the assumption that a person

cannot get infected multiple times [6]. Such finite-size effects [18–23] start much earlier than the saturation is reached. Even if there exists no preventive measures, recovery and death can lead to a deviation from the exponential behavior. This is analogous to the onset of finite-size effects in systems exhibiting phase transitions, though of different origin [18–23]. In reality, the saturation number is much less than the total population. This is, as mentioned above, due to early detections of the disease, preventive measures taken to reduce the spread, etc. These make the finite-size effects more severe, which, of course, is beneficial.

By considering the similarity of this problem with that of domain growth during "phase transitions" in condensed matter systems, having finite sizes, a finite-size scaling (FSS) [19] method was proposed recently [6], to understand the mathematical pattern in disease spread. The number of infected individuals at the end of an epidemic or of a wave within it, N_s, can be considered as the system size here. Application of the scaling method [6] provides information on universal as well as non-universal features of spreads in different geographical regions. Below we discuss the scaling picture. For the sake of convenience we first discuss the FSS picture in the phase transition context.

7.2 Scaling Technique

When a homogeneous system is quenched inside the miscibility gap, evolution towards the new equilibrium starts via the formation of particle rich and particle poor domains. The average size, ℓ, of these domains grows in a power-law fashion with time (t) as [24, 25]

$$\ell \sim t^{\alpha}, \tag{7.1}$$

where α is the growth exponent. Given that there may be an onset time (t_0) for a system to fall unstable to fluctuations, following the quench, or to reach the scaling regime of growth, a more general way of writing this is [21, 22, 26, 27]

$$(\ell - \ell_0) \sim (t - t_0)^{\alpha}, \tag{7.2}$$

where ℓ_0 is the domain length at time t_0. Note that ℓ_0 is like the background contribution in equilibrium critical phenomena [20]. Considering that there always exists inadequacy in system size in computer simulations, the growth will eventually encounter finite-size effects. I.e., at some point, depending upon the size of the system, there will be deviation from the behavior in Eq. (7.2). Let us consider the maximum domain length that can

be attained for a system of size L be ℓ_{max}. Using this fact and Eq. (7.2), one can write [21–23]

$$\ell - \ell_0 = Y(y)(\ell_{max} - \ell_0), \tag{7.3}$$

with $Y(y)$ being a finite-size scaling function and y a dimensionless scaling variable, defined as [21–23]

$$y = \frac{(\ell_{max} - \ell_0)^{\frac{1}{\alpha}}}{t - t_0}. \tag{7.4}$$

The construction of Eq. (7.3) is motivated by the following fact in equilibrium critical phenomena. A quantity X, having singularity [28–30]

$$X \sim \epsilon^{-x}, \tag{7.5}$$

ϵ being the deviation of a considered state point from the critical point, has a behavior [19]

$$X \sim L^{x/\nu}, \tag{7.6}$$

when measured at the "critical" points for systems of varying size L, ν being the critical exponent for the correlation length ξ. This finite-size behavior is bridged with the thermodynamic limit behavior via the introduction of a finite-size scaling function. Analogous to the fact that at the criticality $\xi = L$, in the considered nonequilibrium problem the finite-size limit is $\ell = \ell_{max}$. The difference of ℓ_{max} from actual system size L arises from the chosen method of measurement, composition or density in the coarsening system, etc.

When plotted versus y, data for Y from different system sizes will overlap on top of each other, for the correct choices of t_0 and α. Thus, Y is independent of system size, for a specific problem. This should not, however, be associated with universality. Universality in finite-size behavior will be established if the functional form for Y is unique irrespective of transitions or materials of different types [23, 31, 32]. In the case of disease spread the statement applies when the functional form is same for different geographical regions, i.e., if data from multiple countries overlap to provide a unique Y [6], despite the fact that there exist disparity in economy, population density, ethnicity, etc., among the considered group of countries.

In the limit $y \to 0$, i.e., $t \to \infty$, the scaling function $Y(y)$ will approach a constant value. When $y \to \infty$, $Y(y)$ should have a power-law behavior [23]

$$Y(y) \sim y^{-\alpha}. \tag{7.7}$$

Eq. (7.7) is compatible with the thermodynamic limit form, as quoted in Eq. (7.2), of domain growth.

Next we consider the case of an epidemic. Here, during early days of spread, the total number of infections at time t, $N(t)$, can be written as [6, 15]

$$N = N_0 \exp(mt), \tag{7.8}$$

with N_0 and m being positive constants. Let N_d be the population that gets infected at the time when the deviation from the exponential behavior occurs. This is the time when the finite-size effects start. Studies of phase transition suggests that this is proportional to the system size. I.e., in this case $N_d \propto N_s$. Given that for an ongoing wave of an epidemic N_s is not known, it is instructive to use N_d for the scaling analysis [6], if studies are designed with the objective to influence strategies to control the spread or to advice the governments on improvement of health infrastructures. In any case, a new wave may come even before an ongoing wave ends. That way it is difficult to have a good estimate of N_s.

A scaling ansatz in this case can be written as [6]

$$\ln n = Y(y) \ln n_d, \tag{7.9}$$

where

$$n = \frac{N}{N_0}, \tag{7.10}$$

$$n_d = \frac{N_d}{N_0}, \tag{7.11}$$

and

$$y = \frac{\ln n_d}{mt}. \tag{7.12}$$

Here $Y(y) \to$ constant as $y \to 0$, and as $y \to \infty$, $Y(y)$ should have the power-law behavior [6]

$$Y(y) \sim y^{-1}. \tag{7.13}$$

For the construction of a full analytical form for $Y(y)$, definition of an instantaneous exponent [6, 26],

$$\psi_i = \frac{d \ln Y}{d \ln y}, \tag{7.14}$$

can be useful. This will have a plateau at -1 for large y. By considering this as $-p$, rather than fixing the value at -1, a general form can be written as [6]

$$-\frac{1}{\psi_i} = \frac{1}{p} + by^{-\theta}. \tag{7.15}$$

Eq. (7.15) satisfies the empirical fact that in the $y \to 0$ limit Y approaches a constant, i.e., ψ_i is zero. Of course, the last term could have been of logarithmic or exponential character. The choice of a power-law form has practical reason [6]. By using Eqs. (7.14) and (7.15), one obtains [6]

$$Y(y) = Y_0 \left(b + \frac{y^\theta}{p}\right)^{-p/\theta}. \tag{7.16}$$

Here Y_0, b, and θ are positive constants. The same function may describe the finite-size scaling data for domain growth as well.

From Eq. (7.9), the total number of infections, $N(t)$, can be written as [6]

$$N(t) = N_0 \left(\frac{N_d}{N_0}\right)^Y. \tag{7.17}$$

This provides, by using Eqs. (7.16), (7.12), and (7.11),

$$N(t) = N_0 \exp\left[N_1 t^p (1 + N_2 t^\theta)^{-p/\theta}\right], \tag{7.18}$$

where

$$N_1 = Y_0 \ln n_d \frac{1}{p^{-p/\theta}} (m/\ln n_d)^p, \tag{7.19}$$

and

$$N_2 = bp(m/\ln n_d)^\theta \tag{7.20}$$

are constants.

The reason behind taking the finite-size scaling route to arrive at Eq. (7.18) is to exploit the similarity and familiarity with kinetics of phase transition. A broad objective is, of course, to establish universality in a larger nonequilibrium domain [6]. Now that we have Eq. (7.18), without taking the route of direct and formal FSS analysis the ground data can be fit to the latter equation, for different geographical regions. Assembling the country specific values of p and θ, thus obtained, conclusion on the existence or nonexistence of universality can be drawn, in an indirect way.

7.3 A Few Other Details

We have collected the COVID-19 data, that are made available online [33, 34], for different countries. Note here that we are not adopting any mathematical models such as SI or SIR. The study is performed by applying the method mentioned in the previous section to the collected data sets [6, 33, 34]. For comparing this finite-size scaling picture with that of growth in the phase transition dynamics, we present results for the kinetics in Ising model with conserved order-parameter (COP) dynamics [24, 25]. For the COP dynamics, the total value of the order parameter, i.e., sum of the spins over the whole system, does not change during a phase change [24, 25].

The Hamiltonian of the nearest-neighbor Ising model is written as [25, 35]

$$H = -J \sum_{\langle ij \rangle} S_i S_j;\ J > 0, \tag{7.21}$$

with $S_i = +1$ and -1 denoting two different kinds of particles, say, A and B, and J is the interaction strength. Here $\langle ij \rangle$ represents summation over nearest neighbors. We perform Monte Carlo [35] simulations of this binary mixture model using Kawasaki exchange dynamics [36]. Under this scheme the particles sitting on the randomly chosen neighboring sites exchange positions in accordance with the standard Metropolis criterion [35]. We performed the simulations on 2-dimensional square lattice. L is the linear dimension of square boxes that we have considered, in units of the lattice constant a. The time is measured in units of Monte Carlo steps (MCS) with one MCS consisting of L^2 trial moves. Note that for the disease dynamics the unit of time is a day. The quench temperature, T_f, is set at $0.5T_c$, T_c being the critical temperature, having a value [35] $2.269J/k_B$, where k_B is the Boltzmann constant. We fix the values of J, k_B, and a to unity, for the sake of convenience of presentation.

The average domain lengths are calculated from the domain-size distribution function, $P(\ell_d, t)$, as [21, 22]

$$\ell(t) = \int P(\ell_d, t) \ell_d d\ell_d. \tag{7.22}$$

Here ℓ_d is the distance between two successive interfaces in a specific direction. For each of the system sizes, the values of $\ell(t)$ have been obtained after averaging over simulation runs with 1000 independent initial configurations. For this purpose noise clusters in the system were appropriately removed via the application of a majority sum rule [21]. At early time noise is much less. This was appropriately taken care of.

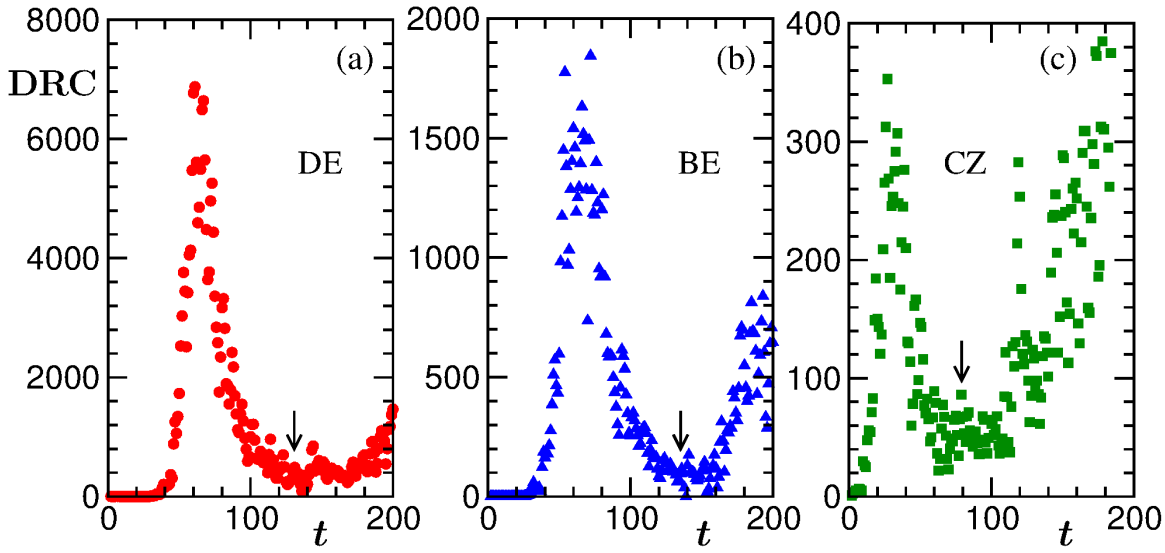

Figure 7.1: Plots of the daily reported cases (DRC) of COVID-19, for three different countries, viz., (a) Germany (DE), (b) Belgium (BE), and (c) Czech Republic (CZ). The arrows mark the (approximate) ends of the first waves of the disease spread in the respective countries.

7.4 Results

Table 7.1: List of values of t_0, N_0, and θ, along with the dates of detection of the first infections and the ends of the first waves, for a large set of countries.

Countries	Dates of detection of first infections	t_0	N_0	Dates of end of first waves	θ
Germany (DE)	27 January 2020	32	46	4 June 2020	3.31
Czech Republic (CZ)	1 March 2020	2	3	19 May 2020	2.92
Belgium (BE)	4 February 2020	32	109	17 June 2020	2.96
New Zealand (NZ)	28 February 2020	18	8	23 May 2020	3.51
Monaco (MC)	29 February 2020	12	1	28 April 2020	3.43
Luxembourg (LU)	29 February 2020	6	1	2 June 2020	3.06
Tunisia (TN)	4 March 2020	5	2	25 May 2020	3.04
Spain (ES)	1 February 2020	26	13	7 June 2020	3.53
United Kingdom (UK)	31 January 2020	26	34	4 July 2020	2.78
Switzerland (CH)	25 February 2020	3	8	6 June 2020	3.69
Italy (IT)	31 January 2020	24	155	27 June 2020	2.69
Finland (FI)	29 January 2020	31	2	12 July 2020	2.66
Norway (NO)	26 February 2020	4	15	4 June 2020	2.55
Papua New Guinea (PG)	20 March 2020	119	11	2 October 2020	3.4

In Fig. 7.1 we present the number of daily reported cases (DRC) of COVID-19 for three different example countries, viz., Germany (DE), Belgium (BE), and Czech Republic (CZ) [33]. The dates of detections of the first infections [33] are listed in Table 7.1, along with information on several other parameters. In addition to these three countries, information for many other countries are also included in this table. From Fig. 7.1, it is clear that each of the countries suffered from multiple waves of the spread. The downward arrows mark the positions of the ends of the first waves that we have roughly estimated, based purely on approximate visual judgement. From here onwards, we will focus on these first waves.

The total number of reported cases, i.e., $N(t)$, as a function of t, for the same three countries are presented in Fig. 7.2. Here we have presented data sets only up to the ends of the first waves. The same data sets in a semi-log scale are presented in Fig. 7.3(a). Given that the early time disease transmission is expected to be exponential in nature [6, 15], the data at the beginning should have a linear appearance in certain semi-log scale. This can be appreciated from this figure. The dashed lines represent the form $\exp(mt)$, the values of m being mentioned near the corresponding lines. The onset time of exponential behavior, denoted as t_0, is different for each of the countries [6]. We quantified these and subtracted from the data sets for further analysis. Data before this is usually less reliable. Also it is perhaps safe to say that the instability leading to the exponential growth did not appear till this time. N_0 is the total number of cases at t_0. The values of t_0 and N_0 are listed in Table 7.1. In Fig. 7.3(b), we have plotted $N(t)/N_0$, denoted by n, versus $m\tau$ ($\tau = t - t_0$), in a semi-log scale. Now the expected linear behavior can be seen from the beginning [6]. The dashed line here corresponds to the function $\exp(m\tau)$. As we have already mentioned, the deviation from the exponential behavior of the disease spread is connected to various factors, such as the detection and isolation of the infected individuals, recovery or death of the patients, the social restrictions imposed by the authorities, etc. These measures and values of m being different for each country, the deviation from the early exponential behavior and the saturation in the total number of cases (assuming that there exists a perfect end) are also different for different countries. This can be appreciated from Fig. 7.3.

This picture is very similar to the growth dynamics in the kinetics of phase transitions [6, 24, 25]. In the latter case, the average domain length, $\ell(t)$, of a system follows a power-law behavior with an exponent α [24, 25], as already mentioned. In Fig. 7.4 we present the results from the Ising model with the conserved order-parameter dynamics [21, 24, 25], for quench to $0.5T_c$, from random initial configurations. In Fig. 7.4(a), $\ell(t)$

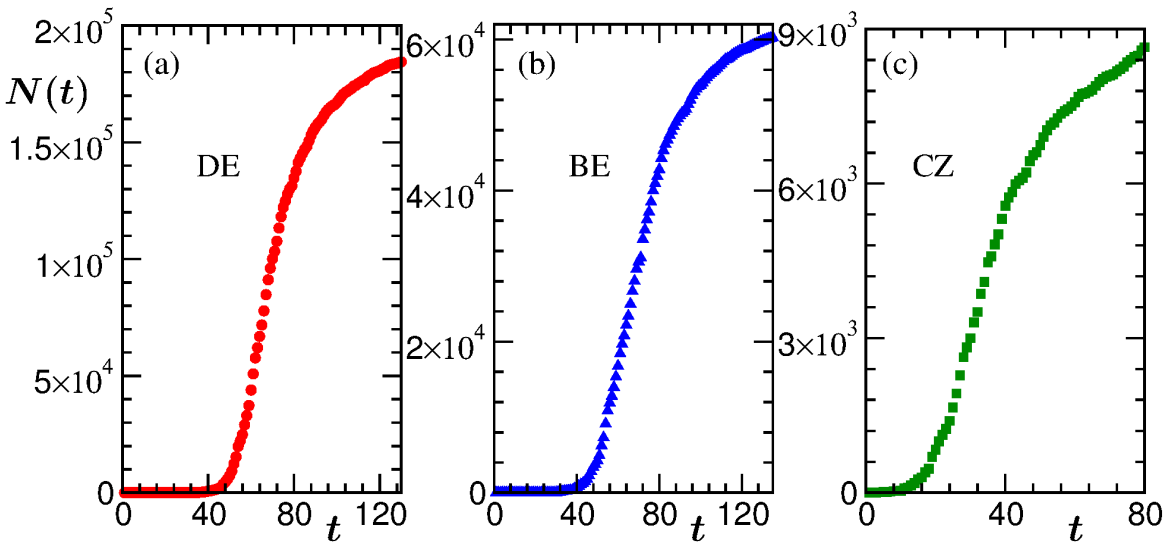

Figure 7.2: Plots of the total number of reported cases, $N(t)$, of COVID-19, till time t (in units of day) for the same three countries as in Fig. 7.1. Here the data are presented only up to the ends of the first waves.

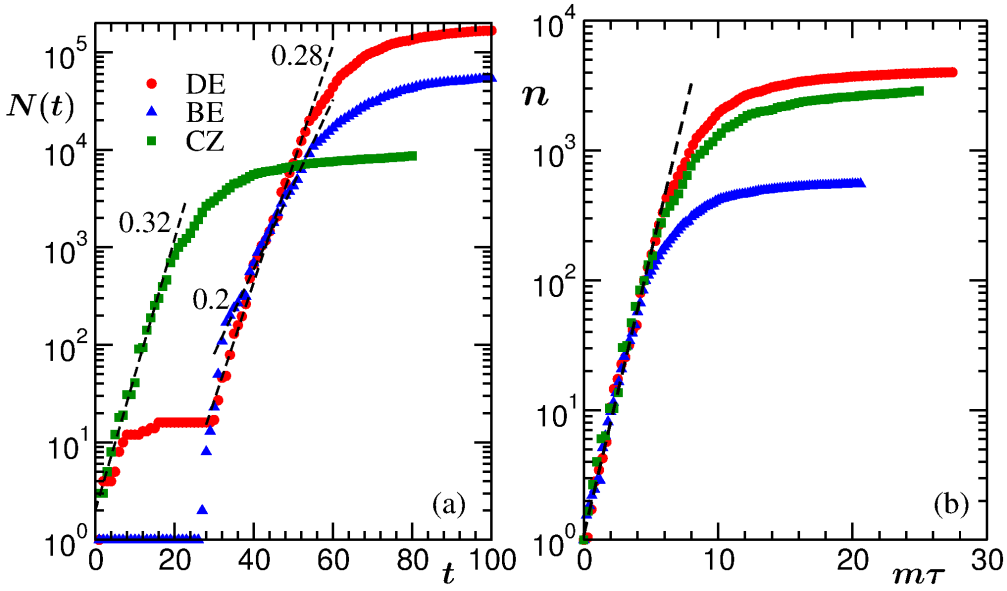

Figure 7.3: (a) Same as in Fig. 7.2, but here the data are presented on a semi-log scale such that the early exponential behavior is appreciated. The dashed lines correspond to $\exp(mt)$ with the values of m mentioned near the lines. (b) Plots of the "normalized" values of the total numbers of cases, n $(= N/N_0)$, versus $m\tau$, with $\tau = t - t_0$, for the same set of countries as in part (a). The dashed line corresponds to the exponential behavior.

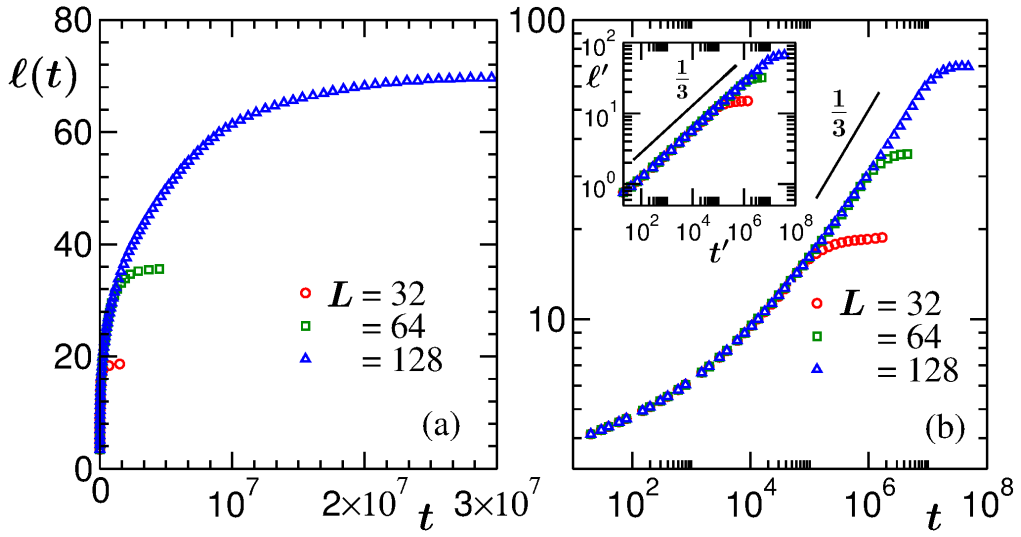

Figure 7.4: (a) The plots of domain length, $\ell(t)$, versus time, t, for different system sizes, for the Ising model with conserved order-parameter dynamics. (b) Same as (a) but here the data are presented on a log-log scale. The solid line represents a power-law with the mentioned value of the exponent. Inset: Plots of ℓ' $(= \ell(t) - \ell_0)$ versus t' $(= t - t_0)$ on a log-log scale. The power-law with an exponent 1/3 is shown here as well. The value of t_0 (and thus, ℓ_0) was obtained from finite-size scaling exercise.

are plotted versus t from different system sizes, in a linear scale. One can observe that the data from smaller system sizes saturates to a constant value faster than the larger ones [18–21]. This is related to the fact that the system with a smaller size equilibrates and, thus, encounters the finite-size effects earlier. Despite similarity there exists an important difference between the cases in Fig. 7.3(b) and Fig. 7.4(a). In the case of the latter, the system is same for all the values of L. For Fig. 7.3(b), the countries, i.e., the systems are different. Thus, if scaling collapses of data are observed, the corresponding Y will imply system-size independence in the Ising case, whereas for the COVID-19 case this will provide a sense of universality.

The same data of Fig. 7.4(a) are plotted on a log-log scale in Fig. 7.4(b). The solid-line here denotes a power-law with the exponent $\alpha = 1/3$, which is the growth exponent emerging from Lifshitz-Slyozov-Wagner theory [37, 38]. We can see that the finite-size unaffected late time data are consistent with this expected power-law behavior. At early time this is not obeyed because of the presence of an initial domain length, ℓ_0, in the system, at time t_0, when the system becomes unstable to the fluctuations [21, 22]. Thus, to obtain a more appropriate information, one should subtract this onset value from the whole data set. We present these results, after subtraction of the latter, in the

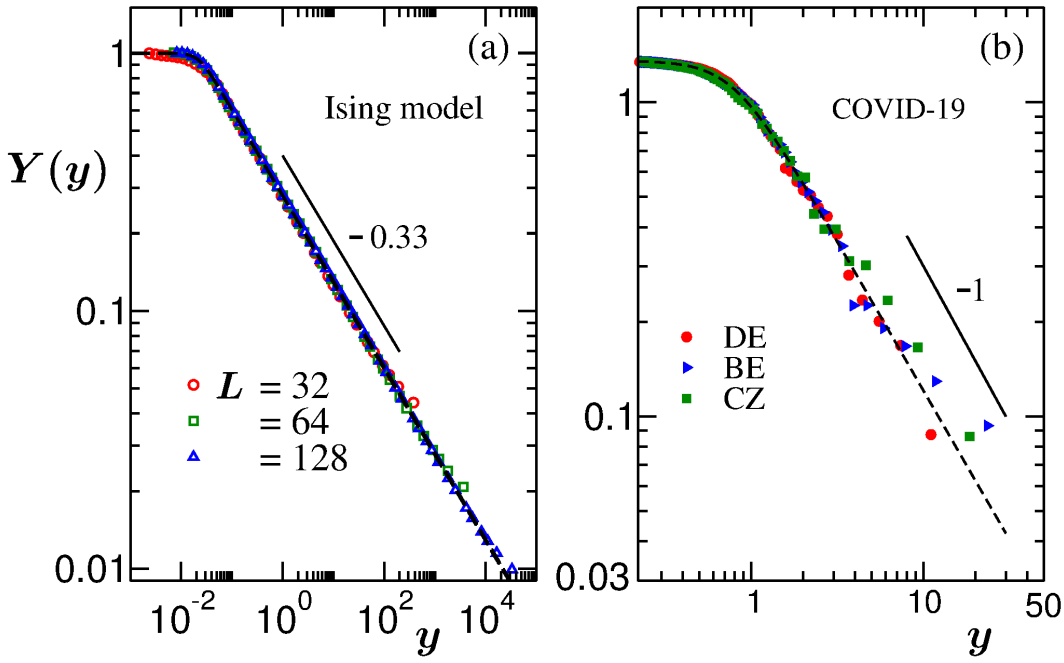

Figure 7.5: (a) The plot of $Y(y)$, versus y, on a log-log scale, obtained by using data from a few different system sizes for the Ising model. The dashed line represents the scaling function given in Eq. (7.16) and the solid line represents a power-law with an exponent -0.33. (b) The scaling plot for the disease case using data from different countries. The dashed line again represents Eq. (7.16). The solid line is a power-law with the value of exponent mentioned near it.

inset of Fig. 7.4(b), again on a log-log scale. The transformed data set is consistent with the same power-law from the beginning [21, 22]. This implies that there exists no strong curvature dependent correction to the growth law [21]. Note that $\ell' = \ell - \ell_0$ and $t' = t - t_0$. The values of ℓ_0 and t_0 are estimated from the best collapse criterion in the FSS analysis, results from which are presented in the following figure [21].

In Fig. 7.5 (a) we present results from the finite-size scaling analysis of the domain lengths for the Ising model [21, 22]. We show $Y(y)$ [cf. Eq. (7.3)] versus y plots, for different system sizes. The best collapse is obtained for the values [21, 22] $\alpha = 0.33$ and $t_0 = 20$ ($\ell_0 = 3.6$). In the large y limit, $Y(y)$ is consistent with a power-law behavior with the exponent $-1/3$, shown in the plot by a solid line. The deviation from this behavior in the data sets at the $y \to 0$ limit is due to the presence of finite-size effects. The dashed line is a fit to the data sets using the scaling function given in Eq. (7.16) by keeping Y_0, b, p, and θ as adjustable parameters. The value of p is 0.334, which is consistent with the power-law behavior of direct data with the exponent $\alpha = 1/3$. The value of θ emerged to be 3.74.

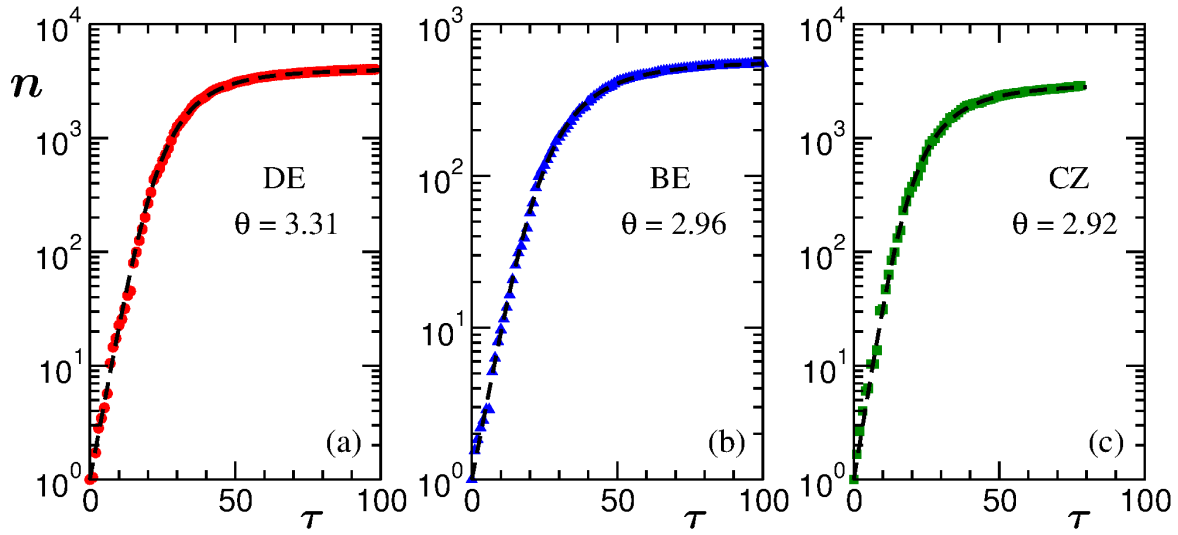

Figure 7.6: Plots of n versus τ, on a semi-log scale, for (a) DE (b) BE, and (c) CZ. We have included real data as well as Eq. (7.18), the latter being represented by dashed lines. The value of θ in each of the cases is mentioned inside the respective frame. The value of p is fixed to 1 in Eq. (7.18) for each of the fittings.

In Fig. 7.5 (b), results from the FSS analysis of the disease-spread data are shown. Here again we have considered the same three countries (DE, BE, and CZ) as in the previous plots. The collapse, concerning $Y(y)$, of the disease data from different countries can be appreciated. Note that these are not simulation data as averages over many independent initial runs. The solid line here denotes a power-law with the exponent -1, which describes the early exponential growth [6]. The dashed line is again a fit of the combined data sets to the same scaling function quoted in Eq. (7.16). Here the value of p appears to be $\simeq 0.95$ which is consistent with 1. The value of θ is 3.29. Surprisingly this value of θ differs from the case of the Ising model only by about 12%.

Furthermore, we used the functional form of $N(t)$, given in Eq. (7.18), to estimate the value of θ for different countries separately. The FSS value of p being only about 5% different from 1, we fix p to 1 for these fittings. In Fig. 7.6, we show n versus τ plots in semi-log scales for DE, BE, and CZ, along with the full analytical form, represented by the dashed lines. This functional form very nicely describes the disease data set in each of the cases. The obtained values of θ are mentioned in the respective frames. We have performed the analysis for many other countries that are mentioned in Table 7.1. The values of θ for each country can be seen in the latter table. Interestingly, these values are not very wide spread for this large set of countries. A better idea on this can be

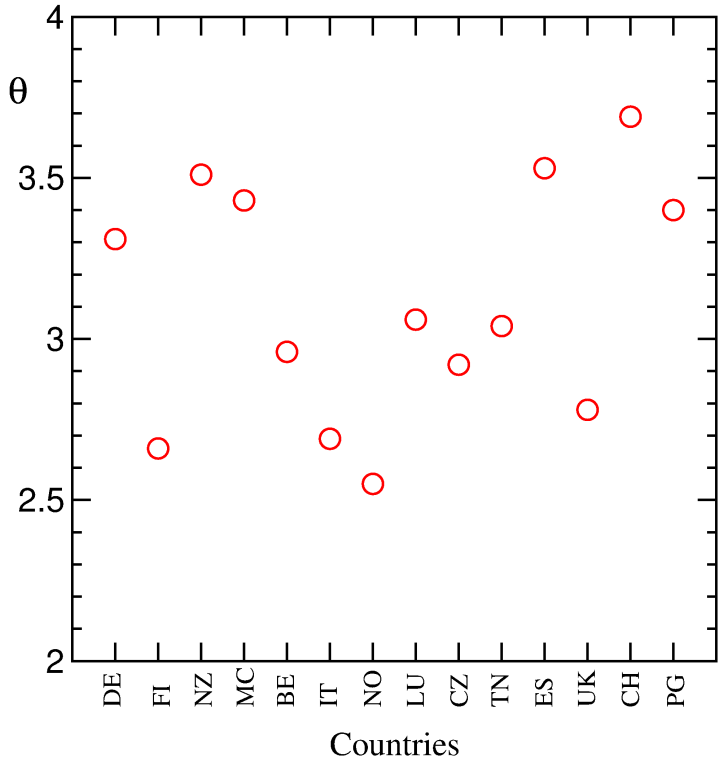

Figure 7.7: The values of θ for different countries. These values are obtained by using Eq. (7.18) after fixing p at 1 in the fitting exercise.

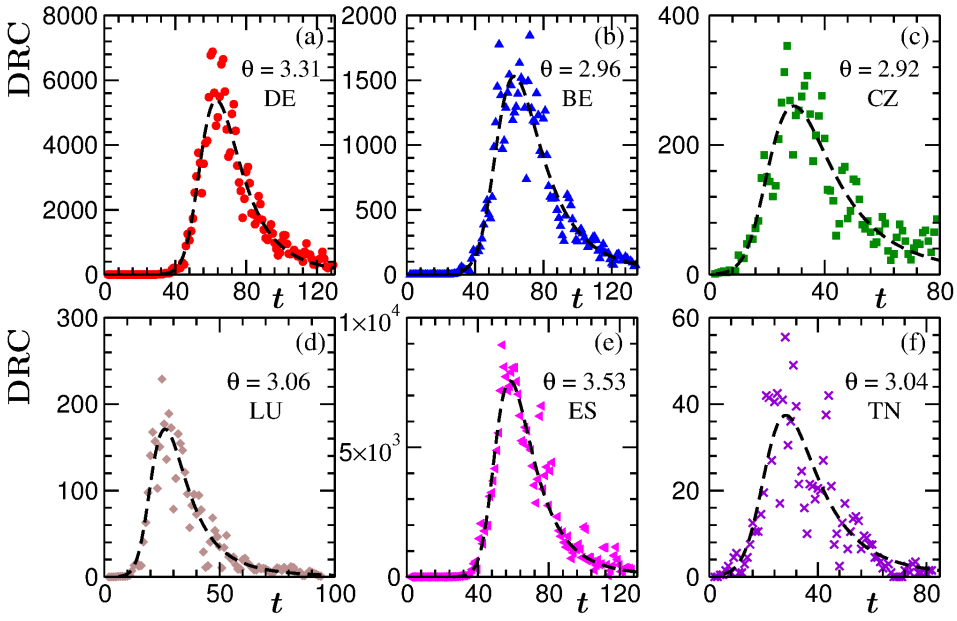

Figure 7.8: The number of daily cases (DRC), versus t, for different countries: (a) DE, (b) BE, (c) CZ, (d) LU, (e) ES, and (f) TN. The dashed lines represent time derivatives of Eq. (7.18). The value of θ is mentioned in each of the frames. The value of p is fixed to 1 for all the cases in the fitting exercise.

obtained from Fig. 7.7. This set of θ has a mean of 3.11 with a standard deviation of $\simeq 0.37$. Thus, there exists a picture of universality that deserves further attention [6].

In Fig. 7.8, we plot the daily cases, DRC, for six different countries. The dashed lines there represent $dN(t)/dt$, with $N(t)$ having the functional form given in Eq. (7.18). It can be seen that these lines nicely describe the DRC data for all the presented countries. A universal feature in the spreading pattern, as mentioned in Ref. [6], seem to be true for a large set of countries.

7.5 Conclusion

We have analysed the COVID-19 data from different countries that are available online [33, 34]. The spread of the disease initially follows an exponential behavior. Deviations from this early trend occur at different points for different countries. Nevertheless, a universal pattern exists in the spread [6]. To understand the picture, we used a recently proposed scaling method [6]. The outcome was compared with that of domain growth in the phase transition kinetics [6, 24, 25], for which the system integrated order parameter remains constant, in the Ising model framework [24, 25].

We have quantified the key parameters in the scaling function, viz., θ and p. The value of p obtained from the scaling analysis was $\simeq 0.95$, close to unity. This is because of the initial exponential growth in the spread. By fixing $p = 1$, we obtained the value of θ separately for a large set of countries, with the help of the analytical form obtained for the total number of cases, $N(t)$. For the presented countries, the mean value of θ came out to be 3.11 with a standard deviation $\simeq 0.37$. This indicates the presence of universal features in the spread.

The method can potentially be used for the purpose of prediction. For this one may obtain θ by fitting Eq. (7.18) to data till the current time for an ongoing wave. Once θ is extracted, predictions can be made with reasonable accuracy. Of course, the accuracy will improve as longer set of data become available. There, of course, exists other functional forms in the literature, to describe a full wave [3]. However, this approach is convenient and the mathematical form is reasonably simple. Even though there exists four parameters, some of these can be fixed via standard observation.

References

[1] H. Tian, Y. Liu, Y. Li, C. Wu, B. Chen, M.U.G. Kraemer, B. Li, J. Cai, B. Xu, Q. Yang, B. Wang, P. Yang, Y. Cui, Y. Song, P. Zheng, Q. Wang, O.N. Bjornstad, R. Yang, B.T. Grenfell, O.G. Pybus, and C. Dye, Science **368**, 638 (2020).

[2] M.U.G. Kraemer, C. Yang, B. Gutierrez, C. Wu, B. Klein, D.M Pigott, Open COVID-19 Data Working Group; L. du Plessis, N.R Faria, R. Li, W.P Hanage, J.S Brownstein, M. Layan, A. Vespignani, H. Tian, C. Dye, O.G Pybus, and S.V Scarpino, Science **368**, 493 (2020).

[3] J. Demongeot, Q. Griette, and P. Magal, R. Soc. Open. Sci. **7**, 201878 (2020).

[4] N. Wang, Y. Fu, H. Zhang, and H. Shi, Precision Clinical Medicine **3**, 85 (2020).

[5] A.L. Bertozzi, E. Franco, G. Mohler, M.B. Short, and D. Sledge, Proc. Natl. Acad. Sci. U.S.A. **117**, 16732 (2020).

[6] S.K. Das, Proc. R. Soc. A **477**, 20200689 (2021).

[7] X. Hou, S. Gao , Q. Li, Y. Kang, N. Chen, K. Chen, J. Rao, J.S. Ellenberg, and J.A. Patz, Proc. Natl. Acad. Sci. U.S.A. **118**, e2020524118 (2021).

[8] I.F. Mello, L. Squillante, G.O. Gomes, A.C. Seridonio, and M. de Souza, Physica A **573**, 125963 (2021).

[9] R.I Mukhamadiarov, S. Deng, S.R Serrao, Priyanka, R. Nandi, L.H. Yao, and U.C Täuber, Sci. Rep. **11**, 130 (2021).

[10] R. Ronald, Nature **87**, 466 (1911).

[11] R. Ronald, Proc. R. Soc. Lond. A **92**, 204 (1916).

[12] W.O. Kermack and A.G. McKendrick, Proc. R. Soc. Lond. A **115**, 700 (1927).

[13] R.M. Anderson and R.M. May, Science **215**, 1053 (1982).

[14] R.M. Anderson, in *Population Dynamics of Infectious Diseases: Theory and Applications*, edited by R.M. Anderson (Chapman and Hall, NewYork, 1982), pp. 1-37.

[15] H.W. Hethcote, SIAM Rev. **42**, 599 (2000).

[16] C. Castillo-Chavez, S. Blower, P. van den Driessche, D. Kirschner, and A. Yakubu (eds.), *Mathematical Approaches for Emerging and Reemerging Infectious Diseases: Models, Methods, and Theory* (Springer, 2002).

[17] F. Croccolo and E. Roman, Chaos, Solitons and Fractals **139**, 110077 (2020).

[18] M.E. Fisher, in *Critical Phenomena*, edited by M.S. Green (Academic, London, 1971) p. 1.

[19] M.E. Fisher and M.N. Barber, Phys. Rev. Lett. **28**, 1516 (1972).

[20] S.K. Das, M.E. Fisher, J.V. Sengers, J. Horbach, and K. Binder, Phys. Rev. Lett. **97**, 025702 (2006).

[21] S. Majumder and S.K. Das, Phys. Rev. E **84**, 021110 (2011).

[22] S. Majumder and S.K. Das, Phys. Chem. Chem. Phys. **15**, 13209 (2013).

[23] S.K. Das, S. Roy, S. Majumder, and S. Ahmad, Europhys. Lett. **97**, 66006 (2012).

[24] A.J. Bray, Adv. Phys. **51**, 481 (2002).

[25] S. Puri and V. Wadhawan (eds.), *Kinetics of Phase Transitions* (CRC Press, Boca Raton, 2009).

[26] D.A. Huse, Phys. Rev. B **34**, 7845 (1986).

[27] J.G. Amar, F.E. Sullivan, and R.D. Mountain, Phys. Rev. B **37**, 196 (1988).

[28] M.E. Fisher, Rep. Prog. Phys. **30**, 615 (1967).

[29] K.G. Wilson, Phys. Rev. B **4**, 3174 (1973).

[30] A. Onuki, *Phase Transition Dynamics* (Cambridge University Press, Cambridge, England, 2002).

[31] S. Majumder, S.K. Das, and W. Janke, Phys. Rev. E **98**, 042142 (2018).

[32] S. Majumder, J. Zierenberg, and W. Janke, Soft Matter **13**, 1276 (2017).

[33] https://github.com/owid/covid-19-data/blob/master/public/data.

[34] https://www.worldometers.info/coronavirus.

[35] D.P. Landau and K. Binder, *A Guide to Monte Carlo Simulations in Statistical Physics* (Cambridge University Press, Cambridge, 2009).

[36] K. Kawasaki, in *Phase Transition and Critical Phenomena*, edited by C. Domb and M.S. Green (Academic, New York, 1972), Vol. 2, p. 443.

[37] I.M. Lifshitz and V.V. Slyozov, J. Phys. Chem. Solids **19**, 35 (1961).

[38] C. Wagner, Z. Elektrochem. **65**, 581 (1961).

Chapter 8

Summary of the Thesis

In Chapter 2, we have studied structural, growth, and aging properties of the ferromagnetic (nonconserved) Ising model in space dimensions $d = 2$ and 3 via Monte Carlo simulations. We have quenched the systems from a starting temperature $T_s = \infty$, which corresponds to a disordered phase, to a final temperature $T_f = 0$. Domain growth and aging in the Ising model are well studied. Nevertheless, there are controversies in the case of the 3D Ising model for quenches to zero temperature. Some of the earlier studies of domain growth in the latter case reported a value of the growth exponent, α, that is much smaller than the theoretical prediction. We observe, however, that the value of α crosses over to the theoretical value, 1/2, in the asymptotic limit. In addition, we have identified anomaly in the aging dynamics, via the studies of the autocorrelation function, $C_{\rm ag}(t, t_w)$, where t and t_w are the observation and the waiting times, respectively. $C_{\rm ag}(t, t_w)$ decays in a power-law manner with an exponent λ, referred to as the aging exponent. We have quantified the value of λ via the finite-size scaling analysis of $C_{\rm ag}(t, t_w)$ [see Fig. 8.1(a)]. The obtained value is much smaller than the theoretical prediction, and it also violates a well-known lower bound. We justify the observation of this lower value by considering the structural features at this temperature [1].

We have extended the above study in Chapter 3 by considering a set of other low quench temperatures, to check whether the anomalies mentioned above are unique to zero temperature quench or not. We have quantified the aging exponent, λ, and showed that this has small values at other low temperatures as well, and it approaches the theoretical value, λ^3_{LM}, as $T_f \to T_R$, the roughening transition temperature. This is demonstrated in Fig. 8.1(b) where we have plotted $\Delta\lambda$, the difference between λ and λ^3_{LM}, as a function of $1/T_f$. The structural anomaly can be quantified by using the two-point equal-time correlation function, $C(r, t)$. In Fig. 8.1(b), we have also plotted

ΔI, the difference between $C(r,t)$ and the analytical form of it, referred to as the Ohta-Jasnow-Kawasaki function. We have shown that ΔI and $\Delta\lambda$ exhibit similar trend – both converge to zero for $T_f \to T_R$. This indicates a strong structure-dynamics connection in phase-ordering dynamics [2].

Next, in Chapter 4, we have investigated the dependence of the aging dynamics on initial correlations for transition to ferromagnetic state in $d = 2$ and 3. For this we have quenched the systems from the starting temperatures $T_s = T_c$, the critical temperatures, to the final temperatures $T_f = 0.6T_c$. Note that at T_c, the correlation length, ξ, diverges. We observe that the decay of $C_{\rm ag}(t, t_w)$ is rather slow, giving rise to a significantly smaller λ than that for the quenches from random initial configurations, i.e., $T_s = \infty$. This is depicted in Fig. 8.1(c) for both $d = 2$ (upper frame) and 3 (lower frame). Thus, in kinetics of phase transitions, universality can be divided into two classes, based on the presence or absence of spatial correlations in the system – one corresponding to $T_s = \infty$ ($\xi = 0$), and the other with $T_s = T_c$ ($\xi = \infty$) [3, 4].

The influence of initial correlations on the nonequilibrium dynamics also has connection with a counter-intuitive phenomenon known as the Mpemba effect (ME). According to the ME, a hotter body of water freezes faster than a colder one. In Chapter 5, we have investigated the presence of it in the 2D Ising ferromagnet. We have quenched the system to a fixed final temperature from different starting temperatures, T_s. We observe that the system with a higher T_s value approaches the new equilibrium faster than the ones with the smaller T_s values – a corresponding energy (E) plot is given in Fig. 8.1(d). This shows the presence of ME in our simple system of interest [5]. The observation is even more counter-intuitive because the model we considered does not have any in-built frustration-like features in the Hamiltonian, which is typically thought to provide this effect.

Till chapter 5, we have studied the evolutions in systems exhibiting nonconserved order-parameter dynamics. In chapter 6, we have considered a system with conserved order-parameter dynamics, where the total value of the order parameter remains the same during the phase transition. Here we have studied the kinetics of phase separation in a single component Lennard-Jones system, via molecular dynamics simulations, in space dimension $d = 3$ for low density and low temperatures. At very low temperatures, disconnected fractal clusters form at late times. We quantified the fractal dimensions of these late time structures and studied the dynamics of their growth by calculating the average cluster mass, $M(t)$ – a corresponding plot is given in Fig. 8.1(e). The exponent of the power-law growth of $M(t)$ depends strongly on temperature [see the

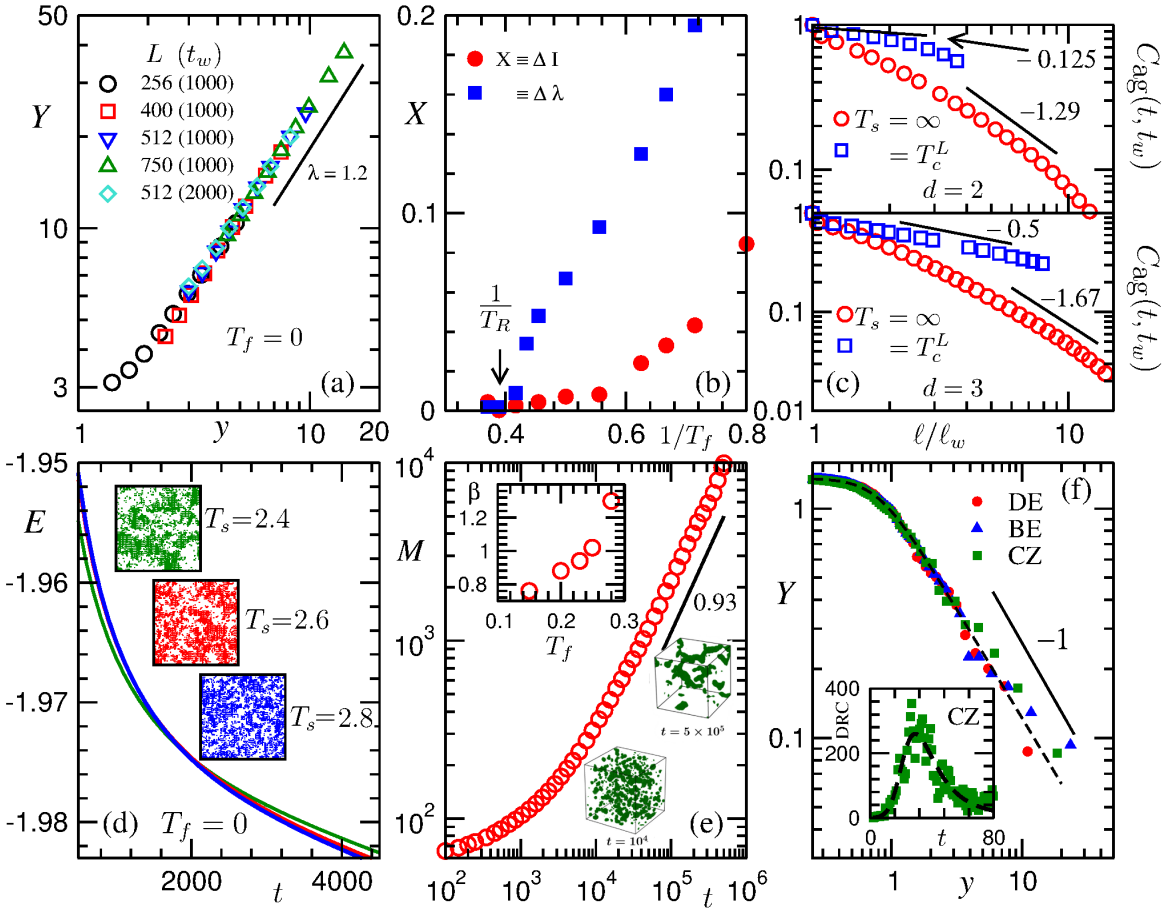

Figure 8.1: (a) Plot of finite-size scaling function, $Y(y)$, for the autocorrelation function $C_{\rm ag}(t, t_w)$, related to the aging phenomena, versus scaling variable, y, on a log-log scale, for zero temperature quench of 3D Ising ferromagnet. The solid line is a power-law with the exponent mentioned near it. The latter is the value of the aging exponent λ. (b) Plots of ΔI and $\Delta\lambda$, deviations of the structures and aging exponents from the theoretical expectations, versus $1/T_f$, for the 3D Ising model. The point corresponding to the roughening transition temperature, T_R, is marked with an arrow. (c) Plots of $C_{\rm ag}(t, t_w)$ versus ℓ/ℓ_w (ℓ and ℓ_w are the average domain lengths at t and t_w, the observation and waiting times, respectively) for Ising ferromagnets in $d = 2$ (in the upper frame) and 3 (in the lower frame) for quenches below the critical point from $T_s = \infty$ and T_c^L, the latter being the finite-size critical point. The solid lines are the power-laws with exponents mentioned near the lines. These exponents are the values of λ from certain theoretical calculations. (d) The plots of energy, E, versus time, t, for different starting temperatures T_s, in the case of 2D Ising ferromagnets for quenches to $T_f = 0$. Initial structures corresponding to all the T_s values are given in the boxes inside the main frame. (e) The plot of average mass, M, versus t, for a phase-separating single-component Lennard-Jones system. The evolution snapshots are given in smaller frames. Inset at the top contains a plot of the exponent, β, corresponding to the power-law growth of $M(t)$, versus quench temperature, T_f. (f) A scaling plot for COVID-19 data from different countries, viz., Germany (DE), Belgium (BE), and Czech Republic (CZ). The solid line corresponds to a power-law with exponent -1. The dashed line is the mathematical form of scaling function $Y(y)$ for the combined data set. Inset: The plot of the daily number of cases for CZ. The dashed line represents an analytical form.

inset of Fig. 8.1(e)]. In this regime of very low temperature and density, the clusters move ballistically. We aim to explain this via the ballistic theory of aggregation [6].

In chapter 7, we have studied the spread of COVID-19, with an objective of identifying the underlying pattern. We have analyzed the disease data from different countries using a recently formulated scaling method. From the analysis, we observe that the scaling functions corresponding to the disease data from a large set of countries overlap with each other. This indicates the presence of universal features in the spread [see the main frame of Fig. 8.1(f)]. The scaling function allows to obtain an analytical form for the total number of reported cases. By using this functional form, an entire wave of the disease can be described with reasonable accuracy [7]. One such representative plot is shown in the inset of Fig. 8.1(f).

References

[1] N. Vadakkayil, S. Chakraborty, and S.K. Das, J. Chem. Phys. **150**, 054702 (2019).

[2] N. Vadakkayil, S.K. Singha, and S.K. Das, arXiv: 2106.16232 (2021).

[3] S.K. Das, K. Das, N. Vadakkayil, S. Chakraborty, and S. Paul, J. Phys.: Condens. Matter **32**, 184005 (2020).

[4] K. Das, N. Vadakkayil, and S.K. Das, Phys. Rev. E **101**, 062112 (2020).

[5] N. Vadakkayil and S.K. Das, Phys. Chem. Chem. Phys. **23**, 11186 (2021).

[6] N. Vadakkayil, S. Roy, and S.K. Das, Manuscript under preparation.

[7] N. Vadakkayil and S.K. Das, Manuscript under preparation.

Zimbra **nalina@jncasr.ac.in**

Re: Seeking permission to reuse the text and figures of a paper

From : Permissions <permissions@ioppublishing.org> Wed, Sep 08, 2021 02:25 PM

Subject : Re: Seeking permission to reuse the text and figures of a paper

To : nalina@jncasr.ac.in

Cc : das <das@jncasr.ac.in>, koyeldas <koyeldas@jncasr.ac.in>, Saikat Chakraborty <chakrabortys@mpip-mainz.mpg.de>, paul <paul@itp.uni-leipzig.de>

Dear Nalina Vadakkayil,

Thank you for your email and for taking the time to seek this permission.

When you transferred the copyright in your article to IOP, we granted back to you certain rights, including the right to include all or part of the Final Published Version of the article within any thesis or dissertation. Please note you may need to obtain separate permission for any third party content you included within your article.

Please include citation details, "© IOP Publishing. Reproduced with permission. All rights reserved" and for online use, a link to the Version of Record.

The only restriction is that if, at a later date, you wanted your thesis/dissertation to be published commercially, further permission would be required.

I wish you the best of luck with the completion of your thesis/dissertation.

Kind regards,

Sophie

Copyright & Permissions Team
Sophie Brittain - Rights & Permissions Assistant
Cameron Wood - Legal & Rights Adviser

Contact Details
E-mail: permissions@ioppublishing.org

For further information about copyright and how to request permission:
https://publishingsupport.iopscience.iop.org/copyright-journals/
See also: https://publishingsupport.iopscience.iop.org/
Please see our Author Rights Policy https://publishingsupport.iopscience.iop.org/author-rights-policies/
Please note: We do not provide signed permission forms as a separate attachment. Please print this email and provide it to your publisher as proof of permission. **Please note**: Any statements made by IOP Publishing to the effect that authors do not need to get permission to use any content where IOP Publishing is not the publisher is not intended to constitute any sort of legal advice. Authors must make their own decisions as to the suitability of the content they are using and whether they require permission for it to be published within their article.

From: nalina@jncasr.ac.in <nalina@jncasr.ac.in>
Sent: 07 September 2021 08:11
To: Permissions <permissions@ioppublishing.org>
Cc: das <das@jncasr.ac.in>; koyeldas <koyeldas@jncasr.ac.in>; Saikat Chakraborty <chakrabortys@mpip-mainz.mpg.de>; paul <paul@itp.uni-leipzig.de>
Subject: Seeking permission to reuse the text and figures of a paper

Dear Sir/Madam,

I am Nalina Vadakkayil, a Ph. D. student working with Prof. Subir K. Das, from Theoretical Sciences Unit, Jawaharlal Nehru Centre for Advanced Scientific Research, Bangalore, India. I am writing this to seek permission to include parts of the text and figures of a paper that was published in Journal of Physics: Condensed Matter, that I co-authored, in my thesis (titled 'Structure and Dynamics Away from Equilibrium: Scaling results from a few condensed matter systems'). The details of the paper are given below:

"Initial correlation dependence of aging in phase separating solid binary mixtures and ordering ferromagnets", Subir K. Das, Koyel Das, Nalina Vadakkayil, Saikat Chakraborty, and Subhajit Paul, J. Phys.: Condens. Matter **32**, 184005 (2020).

This will be used only for academic purposes. So, I request you to kindly give me the permission to reuse the parts of text and figures.

Your sincerely,
Nalina Vadakkayil

IOP Publishing email addresses have changed from @iop.org to @ioppublishing.org, except those of our legal and finance teams, which have changed to @ioplegal.org and @iopfinance.org respectively.

This email (and attachments) are confidential and intended for the addressee(s) only. If you are not the intended recipient please immediately notify the sender, permanently and securely delete any copies and do not take action with it or in reliance on it. Any views expressed are the author's and do not represent those of IOPP, except where specifically stated. IOPP takes reasonable precautions to protect against viruses but accepts no responsibility for loss or damage arising from virus infection. For the protection of IOPP's systems and staff; emails are scanned automatically.

IOP Publishing Limited
Registered in England under Registration No 00467514.
Registered Office: Temple Circus, Bristol BS1 6HG England
Your privacy is important to us. For information about how IOPP uses your personal data, please see our Privacy Policy

---

Zimbra **nalina@jncasr.ac.in**

RE: Seeking permission to reuse the text and figures of a paper

From : AIPRights Permissions <Rights@aip.org> Fri, Sep 10, 2021 12:47 AM
Subject : RE: Seeking permission to reuse the text and figures of a paper
To : nalina@jncasr.ac.in
Cc : das <das@jncasr.ac.in>, Saikat Chakraborty <chakrabortys@mpip-mainz.mpg.de>

Dear Dr. Vadakkayil:

You are permitted to include material from your article in your thesis, including the full published version, provided you also include a credit line referencing the original publication.

Our preferred format is (please fill in the citation information):

“Reproduced from [FULL CITATION], with the permission of AIP Publishing.”

If the thesis will be available electronically, please include a link to the version of record on AIP Publishing’s site.

Please let us know if you have any questions.

Sincerely,

Susann LoFaso
Manager, Rights & Permissions

AIP Publishing
1305 Walt Whitman Road │ Suite 300 | Melville NY 11747-4300 │ USA
t +1.516.576.2268
rights@aip.org │ publishing.aip.org
Follow us: Facebook │ Twitter │ LinkedIn

From: nalina@jncasr.ac.in <nalina@jncasr.ac.in>
Sent: Tuesday, September 7, 2021 3:15 AM
To: AIPRights Permissions <Rights@aip.org>
Cc: das <das@jncasr.ac.in>; Saikat Chakraborty <chakrabortys@mpip-mainz.mpg.de>
Subject: Seeking permission to reuse the text and figures of a paper

Dear Sir/Madam,

I am Nalina Vadakkayil, a Ph. D. student working with Prof. Subir K. Das, from Theoretical Sciences Unit, Jawaharlal Nehru Centre for Advanced Scientific Research, Bangalore, India. I am writing this to seek permission to include the text and figures of a paper that was published in The Journal of Chemical Physics, that I co-authored, in my thesis (titled 'Structure and Dynamics Away from Equilibrium: Scaling results from a few condensed matter systems'). The details of the paper are given below:

"Finite-size scaling study of aging during coarsening in non-conserved Ising model: The case of zero temperature quench", Nalina Vadakkayil, Saikat Chakraborty, and Subir K. Das, J. Chem. Phys. **150**, 054702 (2019).

This will be used only for academic purposes. So, I request you to kindly give me the permission to reuse the text and figures.

Your sincerely,
Nalina Vadakkayil

(https://www.aps.org/)

Learn about our response to COVID-19 (https://journals.aps.org/covid19?utm_source=top_stripe&utm_medium=web&utm_campaign=covid19), including freely available research (https://journals.aps.org/collections/covid19?utm_source=top_stripe&utm_medium=web&utm_campaign=covid19) and expanded remote access support. (https://journals.aps.org/remote-access?utm_source=top_stripe&utm_medium=web&utm_campaign=covid19)

PHYSICAL REVIEW JOURNALS (/)
Published by the American Physical Society

Journals (/about) Authors (/authors) Referees (/referees) Collections (/collections)
Browse (/browse) Search (/search) Press (/press) (/feeds)

December 2017

APS Copyright Policies and Frequently Asked Questions

What is copyright? http://www.copyright.gov/ (http://www.copyright.gov/)

Copyright is a form of legal protection for original works of authorship. Copyright covers both published and unpublished works.

What does copyright protect?

Copyright, a form of intellectual property law, protects original works of authorship including literary, dramatic, musical, and artistic works, such as poetry, novels, movies, songs, computer software, and architecture. Copyright does not protect facts, ideas, systems, or methods of operation, although it may protect the way these things are expressed. See Circular 1, Copyright Basics, section "What Works Are Protected", see http://www.copyright.gov/circs/circ01.pdf (http://www.copyright.gov/circs/circ01.pdf)

How is a copyright different from a patent or a trademark?

Copyright protects original works of authorship, while a patent protects inventions or discoveries. Ideas and discoveries are not protected by the copyright law, although the way in which they are expressed may be. A trademark protects words, phrases, symbols, or designs identifying the source of the goods or services of one party and distinguishing them from those of others.

What is the difference between copyright infringement and plagiarism?

Copyright infringement occurs when an author's work is reused or republished without the permission of the copyright owner, whether or not author attribution accompanied the reuse.

Plagiarism occurs when an author's work has been reused or republished in such a manner as to make it appear as someone else's work, e.g., without quotation marks and citation of the original work.

Why should I transfer copyright to APS?

Like many other scientific publishers, the American Physical Society (APS) requires authors or their employers to provide transfer of copyright prior to publication. This permits APS to publish the article and to defend against improper use (or even theft) of the article. It also permits APS to publish the article online and to use the article in other forms or media, such as PROLA. By the APS transfer agreement, authors and their employers retain substantial rights in the work, as

specified in the agreement https://journals.aps.org/authors/transfer-of-copyright-agreement (https://journals.aps.org/authors/transfer-of-copyright-agreement) and discussed in your copyright permission letter.

Why should I transfer copyright to APS before the article is accepted for publication by an APS journal?

Transferring copyright early in the process avoids the possibility of delaying publication if the transfer has to be obtained later in the process. As stated in the terms of the copyright transfer agreement, transfer does not take effect until the paper is accepted by an APS journal. The author retains the copyright until acceptance, and has the full freedom, for example, to withdraw the paper from consideration by an APS journal and submit it elsewhere.

Does transferring copyright affect my patent rights?

No. Copyright is separate from any patent rights, and the APS transfer agreement specifically states that patent rights are not affected. However, you should be aware that submitting a manuscript to a journal without first taking steps to protect your patent rights (e.g., filing for a patent) could endanger those rights. Consult your patent attorney.

As the author of an APS-published article, may I post my article or a portion of my article on my own website?

Yes, the author or the author's employer may use all or part of the APS published article, including the APS-prepared version (e.g., the PDF from the online journal) without revision or modification, on the author's or employer's website as long as a fee is not charged. If a fee is charged, then APS permission must be sought. In all cases, the appropriate bibliographic citation and notice of the APS copyright must be included.

What happens if the author has posted an APS-published article on a free access e-print server or on the authors' or institutions' web page and subsequently a fee is imposed for access to those sites?

When a fee is imposed, the author must either obtain permission from APS or withdraw the article from the e-print server or Institutional Repository.

As the author of an APS-published article, may I post my article or a portion of my article on an e-print server?

The author has the right to post and update the article on a free-access e-print server using files prepared and formatted by the author. Any such posting made or updated after acceptance of the article for publication by APS should include a link to the online APS journal article abstract. In all cases, the appropriate bibliographic citation and notice of the APS copyright must be included.

As the author of an APS-published article, can I post my article or a portion of my article on a web resource like wikipedia or quantiki?

Sites like wikipedia and quantiki are strict about permissions and require that authors hold copyright to articles that they post there. In order to allow authors to comply with this requirement, APS permits authors to hold copyright to a “derived work” based on an article published in an APS journal as long as the work contains at least 10% new material not covered by APS's copyright and does not contain more than 50% of the text (including equations) of the original article. The APS will extend the author of a “derived work” the right to all papers published in APS journals.

As the author (or the author's employer) of an APS-published article, may I use copies of part or all of my article in the classroom?

Yes, the author or his/her employer may use all or part of the APS-prepared version for educational purposes without requesting permission from the APS as long as the appropriate bibliographic citation is included.

As the author of an APS-published article, may I use figures, tables, graphs, etc. in future publications?

Yes, as the author you have the right to use figures, tables, graphs, etc. in subsequent publications using files prepared and formatted by you or the APS-prepared versions. The appropriate bibliographic citation must be included.

As the author of an APS-published article, may I include my article or a portion of my article in my thesis or dissertation?

Yes, the author has the right to use the article or a portion of the article in a thesis or dissertation without requesting permission from APS, provided the bibliographic citation and the APS copyright credit line are given on the appropriate pages.

As the author of an APS-published article, may I give permission to a colleague or third party to republish all or part of the article in a print publication?

Yes, as the author you may grant permission to third parties to republish print versions of the article provided the APS-published version (e.g., the PDF from the online journal, or a copy of the article from the print journal) is not used for this purpose. The article may not be published in another journal, and the third party may not charge a fee. The appropriate bibliographic citation and notice of the APS copyright must be included.

As the author of an APS-published article, may I give permission to a colleague or third party to republish all or part of the APS-published version in an online journal, book, database compilation, etc.?

No, an author may not grant permission in this case. To request permission to republish APS-copyrighted material, please refer to the “Reuse & Permissions” link that can be found on each APS article page.

As the author of an APS-published article, may I provide a PDF of my paper to a colleague or third party?

The author is permitted to provide, for research purposes and as long as a fee is not charged, a PDF copy of his/her article using either the APS-prepared version or the author prepared version.

As a third party (not an author), may I republish an article or portion of an article published by APS?

Yes, APS will grant permission to republish articles or portions of articles (e.g., tables, graphs, excerpts) published by APS. Depending on the reuse and medium APS has the right to grant permission subject to APS terms and conditions and a fee may be assessed.

As a third party, may I use articles published by APS for lecture and classroom purposes?

Yes, you may use photocopied articles published by APS for lecture and classroom purposes without asking permission from APS as long as you remain an Authorized User of the APS online research per your institution's site license. Also, there is no limitation on the use of APS articles using links to the material accessible through institutional subscriptions.

How do I request permission to republish APS-copyrighted material?

APS uses Aptara's SciPris™ platform to manage rights and permission requests. APS will continue to support the STM guidelines for all copyright needs. To request permission to republish APS-copyrighted material, please refer to the "Reuse & Permissions" link that can be found on each APS article page.

Once directed to the SciPris™ platform, the following information is required:

1. The format in which the material will be republished, e.g., print, online, CD-ROM, and/or other format
2. How much of the article you want to republish, e.g., all or portion of article; if a portion describe the specific material, e.g., figure numbers, excerpt
3. How the material will be used, e.g., in a book, journal, proceeding, thesis, etc.
4. The title of the article/thesis/chapter etc., and the name of the publication in which your work will appear
5. The name of the publisher
6. Indicate whether or not a fee will be charged for the publication

Upon submission, a letter of permission will be generated, specifying all guidelines and regulations to follow.

Blanket permissions are not granted. Please note all requests are subject to APS terms and conditions (/info/terms.html) and a fee may be assessed.

If your questions have not been addressed and you need further assistance, please email customercare@aps.org (mailto:customercare@aps.org).

Further information

For further information about copyright in general, please refer to the Library of Congress FAQ at https://www.copyright.gov/help/faq/ (https://www.copyright.gov/help/faq/)

Journals published by the American Physical Society can be found at https://journals.aps.org/ (https://journals.aps.org/).

FAQ Version: December 12, 2017

Sign up to receive regular email alerts from *Physical Review Journals*

Enter your email

Sign Up

APS (https://www.aps.org/) | News & Announcements (/edannounce) | (https://twitter.com/APSphysics) (https://www.facebook.com/apsphysics)
Join APS (https://www.aps.org/membership/join.cfm)

AUTHORS

General Information (/authors)
Submit a Manuscript (https://authors.aps.org/Submissions/)
Publication Rights (/pub_rights.html)
Open Access (/open_access.html)
Tips for Authors (/authors/tips-authors-physical-review-physical-review-letters)
Professional Conduct (/authors/professional-conduct-ethics)

REFEREES

General Information (/referees)
Submit a Report (http://referees.aps.org/)
Update Your Information (http://referees.aps.org/)
Referee FAQ (/referees/faq.html)
Outstanding Referees (/OutstandingReferees)

LIBRARIANS

General Information (https://librarians.aps.org/)
Subscriptions (https://librarians.aps.org/subscriptions)
Online License Agreement (https://librarians.aps.org/sitelicense.pdf)
Usage Statistics (http://counter.aps.org/)
Your Account (https://librarians.aps.org/account)

STUDENTS

Physics (https://physics.aps.org)
PhysicsCentral (http://www.physicscentral.com/)
Student Membership (https://www.aps.org/membership/student.cfm)

APS MEMBERS

Subscriptions (https://www.aps.org/membership/aps-publications.cfm)
Article Packs (https://journals.aps.org/article-packs)
Membership (https://www.aps.org/membership/index.cfm)
FAQ (https://www.aps.org/membership/faq.cfm)
APS News (https://www.aps.org/publications/apsnews/index.cfm)
Meetings & Events (https://www.aps.org/meetings/index.cfm)

Privacy (https://www.aps.org/about/webpolicies.cfm#privacy) Policies (/policies) Contact Information (/contact.html)
Feedback (mailto:feedback@aps.org)

©2021 American Physical Society. (https://www.aps.org/) All rights reserved. *Physical Review™*, *Physical Review Letters™*, *Physical Review X™*, *Reviews of Modern Physics™*, *Physical Review A™*, *Physical Review B™*, *Physical Review C™*, *Physical Review D™*, *Physical Review E™*, *Physical Review Applied™*, *Physical Review Fluids™*, *Physical Review Accelerators and Beams™*, *Physical Review Physics Education Research™*, *APS Physics logo*, and *Physics logo* are trademarks of the American Physical Society. Information about registration may be found here (/legal). Use of the American Physical Society websites and journals implies that the

user has read and agrees to our Terms and Conditions (/info/terms.html) and any applicable Subscription Agreement (https://librarians.aps.org/sitelicense.pdf).

When you publish in a Royal Society of Chemistry journal, you keep the copyright of the manuscript. On this page you can learn more about our Licence to Publish and the rights you retain as an author. We also explain where you can deposit and share your article, and how to request permission to re-use other people's work.

The following details apply only to authors accepting the standard Licence to Publish. Authors who are interested in publishing open access should visit our open access pages for more information about our open access licences (/journals-books-databases/open-access/open-access-info/#choose) and deposition rights.

On this page

Share publicly via a scholarly communication network that has not signed up to STM sharing principles	×	×

*You may include your article in the electronic version of your thesis or dissertation as long as it is not made available as a separate document.

⧖ Accepted manuscripts may be distributed via repositories after an embargo period of 12 months

If you are a reader looking for the terms of use for information published by the Royal Society of Chemistry under our standard licence to publish please refer our terms of use (/journals-books-databases/librarians-information/products-prices/licensing-terms-and-conditions/#non-commercial-terms).

CHORUS

We are members of the CHORUS initiative, and therefore make the Accepted manuscript version of articles describing research funded by participating funders publicly available on our web site after an embargo period of 12 months. This is effective for research published from 1st March 2018 onwards. Unless otherwise noted on the article the Accepted manuscript is licensed under the terms of our standard license to publish and is subject to our standard reuse terms (/journals-books-databases/librarians-information/products-prices/licensing-terms-and-conditions/#non-commercial-terms).

Reusing Royal Society of Chemistry material

Reuse permissions requests

Material published by the Royal Society of Chemistry (RSC) and other publishers is subject to all applicable copyright, database protection and other rights. The graphic below outlines the steps to obtain permission to reuse RSC materials, where required:

I am the author of the RSC material I wish to reuse

I am NOT the author of the RSC material I wish to reuse

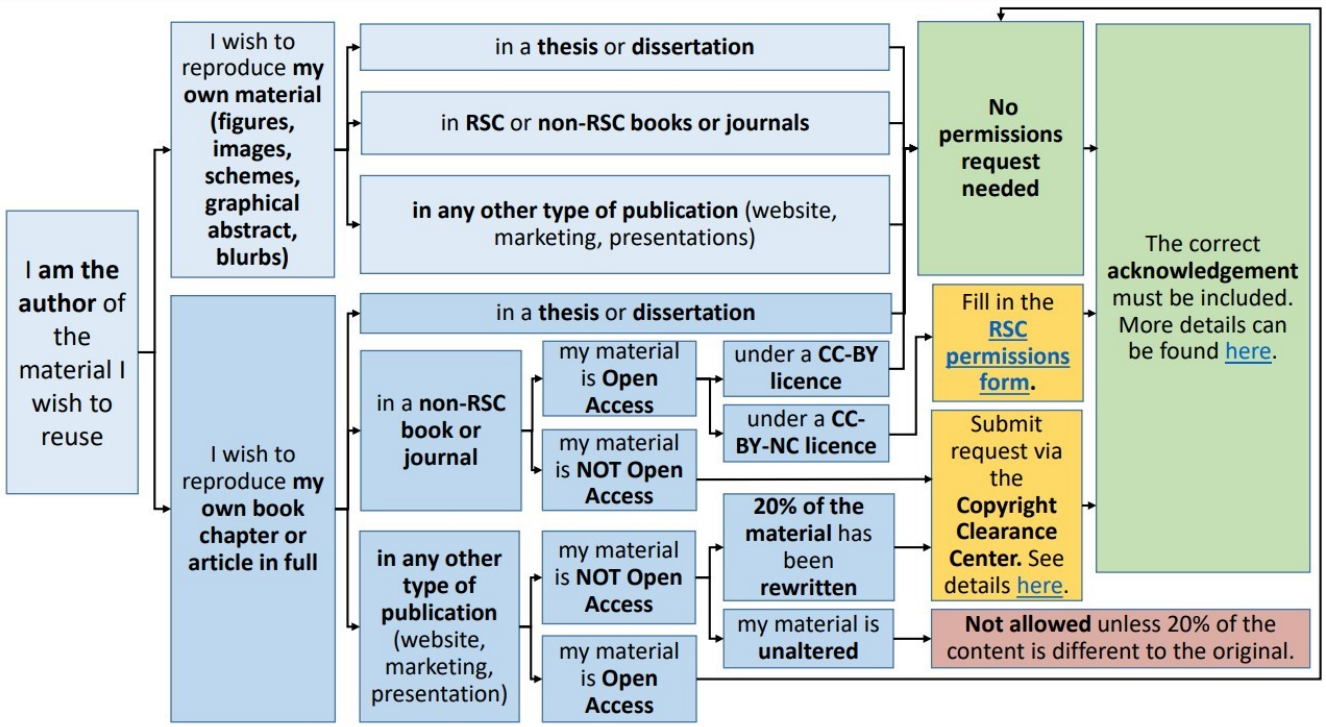

(/globalassets/05-journals-books-databases/journal-authors-reviewers/licenses-copyright-permissions/flowcharts-for-permissions---i-am-the-author.pdf)

Download full-sized flowchart (/globalassets/05-journals-books-databases/journal-authors-reviewers/licenses-copyright-permissions/flowcharts-for-permissions---i-am-the-author.pdf)

More details —

Author reusing their own work published by the RSC

You do not need to request permission to reuse your own figures, diagrams, tables, or images that were originally published in an RSC publication. However, permission should be requested for use of the whole article or chapter except if reusing it in a thesis. If you are including an article or book chapter published by the RSC in your thesis please ensure that your co-authors are aware of this.

Reuse of material that was published originally by the RSC must be accompanied by the appropriate acknowledgement of the publication. The form of the acknowledgement is dependent on the journal in which it was published originally, as detailed in the 'Acknowledgements' section (/journals-books-databases/author-and-reviewer-hub/authors-information/licences-copyright-permissions/#acknowledgements).

Authors reusing RSC material in another RSC publication

Authors contributing to RSC publications (journal articles, book or book chapters) do not need to formally request permission to reproduce material contained in another RSC publication. However, permission should be requested for use of a whole article or chapter. For all cases of reproduction the correct acknowledgement of the reproduced material should be given. The form of the acknowledgement is dependent on the journal in which it was published originally, as detailed in the 'Acknowledgements' section (/journals-books-databases/author-and-reviewer-hub/authors-information/licences-copyright-permissions/#acknowledgements).

Reusing RSC material in material for another publisher, including signatories to the STM Permissions Guidelines

Please submit a permissions request via the Copyright Clearance Center (/journals-books-databases/author-and-reviewer-hub/authors-information/licences-copyright-permissions/#copyrightclearancecenter) to reuse RSC material in material for another publisher. If you are an academic or you are reproducing Royal Society of Chemistry material in a publication to be published by an STM Publisher you will be granted the permission for free for up to three figures. The STM Publishers are those who have signed up to the STM Permissions Guidelines (https://www.stm-assoc.org/intellectual-property/permissions/permissions-guidelines/) and include publishers such as the American Chemical Society, Elsevier, Springer and Wiley. Please submit your request well ahead of publication of your material.

You should check that the material you wish to reproduce is not credited to a source other than the RSC before sending in any request. If the material is credited to another publisher, you are required to seek permission from them.

Reusing RSC material published under a CC-BY and CC-BY-NC licence

An Open Access article is one published under a CC-BY or a CC-BY-NC licence. To check if an article is Open Access, find the journal article from which you want to reproduce material on https://pubs.rsc.org/ (https://pubs.rsc.org/), go to the article landing page by clicking on the article's title, and check the ‘Article information’ on the right-hand side. An Open Access article would read ‘This is an Open Access article’.

If the material for which you are requesting reproduction rights has been published under a **CC-BY** licence, you may reproduce the material, even commercially, without requesting formal permission as long as the material is fully acknowledged and a link is included back to the article on our website.

If the material for which you are requesting reproduction rights has been published under a **CC-BY-NC** licence, you may reproduce the material in a non-commercial publication without requesting formal permission as long as the material is fully acknowledged and a link is included back to the article on our website. Permission must be requested using this RSC Permissions Request Form (/journals-books-databases/author-and-reviewer-hub/authors-information/licences-copyright-permissions/permissions-form/) for commercial reproduction.

Reusing material from other RSC publications

If you are reproducing material from an RSC website, education publication or science policy publication, please fill in the RSC Permissions Request Form (/journals-books-databases/author-and-reviewer-hub/authors-information/licences-copyright-permissions/permissions-form/).

Requests are usually for use of a figure or diagram, but they may also be for use of the entire article or chapter. Requests to use individual figures or diagrams are invariably granted. Permission for another publisher to print an entire RSC article or chapter may be granted in special circumstances.

The permission form should only be used to request permission to reproduce material from Chemistry World, Education in Chemistry, and other non-journal publications of the RSC. For these requests please complete and send the RSC Permissions Request Form (/journals-books-databases/author-and-reviewer-hub/authors-information/licences-copyright-permissions/permissions-form/) to our Contracts and Copyright team.

How to request permission from the RSC via the Copyright Clearance Center

Journals

Find the journal article from which you want to reproduce material and go to the article landing page by clicking on the article's title.

Click on 'Request permissions', which will open up a new window containing permissions information for the article. If required, click on 'Formally request permission' to go to the Copyright Clearance Center.